On the Evaporation of Sessile Droplets

J. M. Stauber
Department of Mathematics and Statistics
University of Strathclyde
Glasgow, UK
August 2015

This thesis is submitted to the University of Strathclyde for the degree of Doctor of Philosophy in the Faculty of Science.

This thesis is the result of the author's original research. It has been composed by the author and has not been previously submitted for examination which has led to the award of a degree.

Signed:

Date:

Acknowledgements

First and foremost, I would like thank my supervisors, Stephen K. Wilson and Brian R. Duffy, for your invaluable advice and support, for your guidance, and for your patience (particularly with all the "inexplicable" commas, that I used). Thank you for all the opportunities you provided me with to take part in conferences and to gain insights into the life of an academic, and, in general, thank you for all of your time and efforts.

I would also like to express my gratitude to Khellil Sefiane for keeping me focused on the "real" droplet world not just the maths behind it. Thank you for all your help.

Thank you very much also to Lindsey and Stephen for all the fun 9 o'clock tutorials, for your willingness to help, and for helping me with all my questions about COMSOL and Matlab. Thank you for cheering me up when I needed it.

My special thanks go to my family. Vielen, vielen Dank meinen Eltern Eva-Maria und Markus, meiner Schwester Rita und meinen Großeltern für die große Unterstützung, dass ihr mir immer mit Rat und Tat zur Seite gestanden seid und dass ihr immer für mich da wart, wenn ich euch gebraucht habe. Danke auch für all eure Ermutigungen, damit ich das Ziel nie aus den Augen verloren habe. Ein großes Dankeschön für das "feste Daumen Drücken" über die Jahre.

In particular, thank you, Ben, for all your help and support (especially for making sure I have been eating these last few months), for telling me to fight on and for all your love and your incredible patience. Thank you for always being there for me to share my joys and my struggles. Thank you for all your encouragement and for proof reading this thesis. I could not have done it without you! Grazzi hafna, qalbi.

A big thank you goes to the Kermode family and to all my friends for all your support over the years.

Finally, I want to thank the UK Engineering and Physical Sciences Research Council (EPSRC), the University of Strathclyde and the University of Edinburgh for funding my work.
S. D. G.

Jutta M. Stauber

Abstract

In this thesis the evolution of sessile droplets in different modes of evaporation and their lifetimes are investigated. The thesis focuses on situations in which the diffusion of vapour into the surrounding atmosphere is the rate-limiting mechanism of evaporation.

First, we describe the evolution of droplets evaporating in the two extreme modes, namely the constant contact radius mode, in which the contact line of the droplet is always pinned, and the constant contact angle mode, in which the contact line of the droplet is always de-pinned. In particular, we demonstrate how these two modes converge on strongly hydrophobic substrates.

Next we study the evolution of droplets evaporating in the stick-slide mode, in which the contact line is initially pinned and the contact angle decreases to the receding contact angle, but thereafter the contact line is de-pinned and the contact radius decreases to zero. The lifetimes of droplets evaporating in the stick-slide mode are investigated in two situations, namely when the initial and receding contact angles are independent and when there is a simple relationship between them based on the assumption of a constant maximum pinning force. In particular, it is shown that the lifetimes of droplets evaporating in this mode may be longer than those of initially identical droplets evaporating in the two extreme modes.

Finally, we develop a model for the evolution of droplets evaporating in a stick-jump mode, in which the contact line pins, de-pins and re-pins multiple times. It is shown that the lifetimes of droplets evaporating in this mode may be longer or shorter than those of initially identical droplets evaporating in the two extreme modes.

Good agreement is found between the predicted lifetimes of droplets in both the stick-slide and the stick-jump modes and the lifetimes of droplets determined from relevant experiments in the literature.

Contents

Chapter 1

Introduction

1.1 The Importance of Droplet Evaporation

This thesis concerns the evaporation of sessile fluid droplets. When a sessile fluid droplet (a droplet of fluid that is deposited onto a substrate) evaporates, fluid molecules escape from the free surface of the droplet, even though some may recondense on the surface, some will escape from the region of the droplet (see, for example, Deegan *et al.* [53]), so that the amount of fluid in the droplet decreases but the amount of vapour, *i.e.* the amount of the fluid molecules in the atmosphere, increases.

Studying the evaporation of sessile fluid droplets is important for several reasons, this introduction presents four. Firstly, the evaporation of sessile fluid droplets occurs in many everyday situations, such as rainfall onto windows, watering plants, applying hairspray, and droplets left on a plastic container in a dishwasher after a wash cycle. Examples of sessile water droplets are shown in figure 1.1. Secondly, and perhaps more significantly, the importance of this problem is due to the fact that it is crucial in a vast range of industrial applications, such

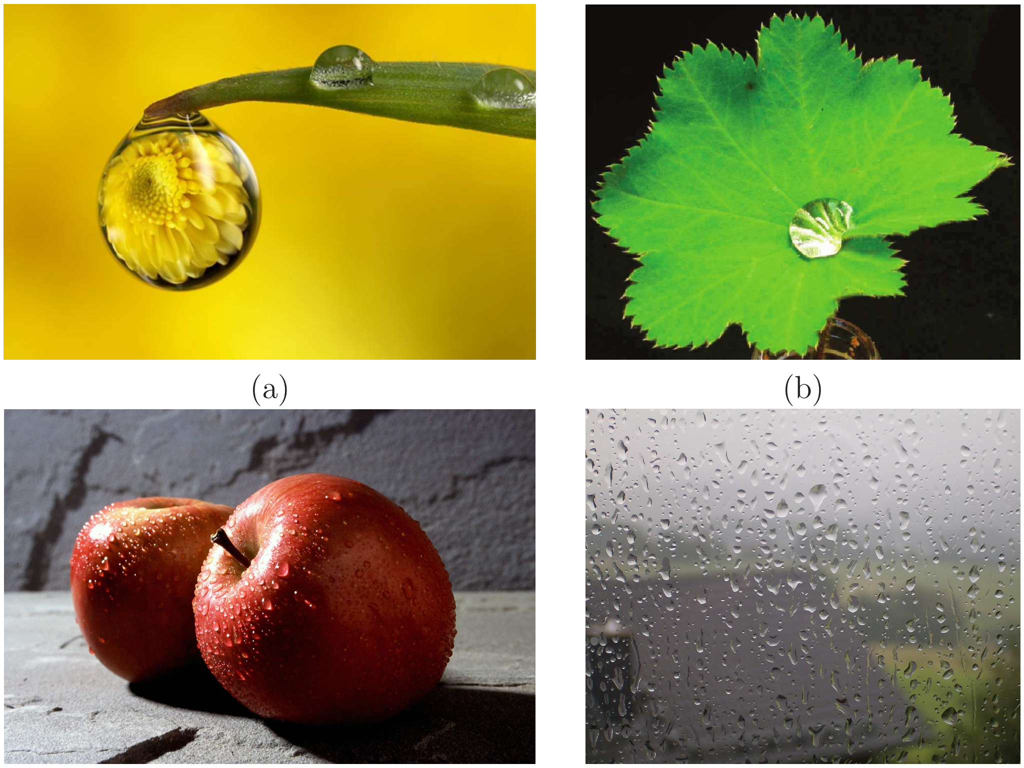

(a) (b)

(c) (d)

Figure 1.1: Examples of water sessile droplets: (a) Sessile droplets on a leaf with a chrysanthemum refracted through a pendent droplet. Reprinted with kind permission from Brian Valentine [236]. (b) Sessile droplet on a Lady's Mantle (Alchemilla). Reprinted with permission from Shirtcliffe *et al.* [209]. Copyright 2009 American Chemical Society. (c) Sessile droplets on Fuji apples [14]. (d) Droplets of rain on a window [238].

as ink-jet printing, spray cooling, production of fine powders and fuel, humidification and drying of air in air-conditioning systems, fire extinguishing, the efficient operation of heat exchangers, the production of thin film coatings, deposition of pesticides, deposition of DNA micro-arrays, and the construction of new optical and electronic materials (see Semenov *et al.* [191] and Erbil [71] and the references therein). Thirdly, studying the evaporation of sessile droplets opens up new possibilities for patterning a substrate. When a sessile droplet of a suspension, *i.e.* a fluid droplet which contains suspended particles, is left to evaporate, the complex interaction between the suspension and the substrate, and the flow of the suspension inside the droplet which occurs due to evaporation, lead to a large variety of deposition patterns. Examples of different deposition patterns such as single and multiple rings, fractal and branched deposit patterns, and three-dimensional structures such as columns, conical structures, spheres, annuli, domes, and disks are shown in figure 1.2 and listed in table 1.1. In particular, as described above, the evaporation of sessile droplets is the escape of fluid from the free surface of the droplet into the atmosphere. This results in a local evaporative flux, *i.e.* the mass of fluid escaping into the atmosphere per unit area per unit time and in a total evaporative flux, which is the surface integral of the local evaporative flux, *i.e.* the mass of fluid escaping into the atmosphere per unit time. In the case when the local evaporative flux is largest at a pinned contact line, *i.e.* the stationary three-phase line where the substrate, fluid, and atmosphere are all in contact, a radial flow towards the contact line leads to the deposition of particles at the contact line, so that after the fluid has completely evaporated from the droplets ring-like stain patterns are formed. These ring-like stain patterns will be discussed further in section 1.5.1, while the wide variety of deposition patterns in general will not be discussed further in this thesis. Fourthly, the evaporation of sessile droplets is of fundamental scientific interest as, for example, the recent review articles by Cazabat and Guéna [37], Erbil [71], Attinger *et al.* [9], Eral *et al.* [68], Bormashenko [23], Larson [118], Kovalchuk *et al.* [115], and Semenov *et al.* [195] demonstrate. Specifically, the study of the evaporation of free droplets, *i.e.* droplets that are suspended in the atmosphere, focuses on the interaction between the fluid and the surrounding atmosphere (see, for example, the review article by Cazabat and Guéna [37]). On the other hand, the study of the evaporation of sessile droplets has additional complications, as it has to take into account all of the interactions between the substrate, the fluid and the atmosphere.

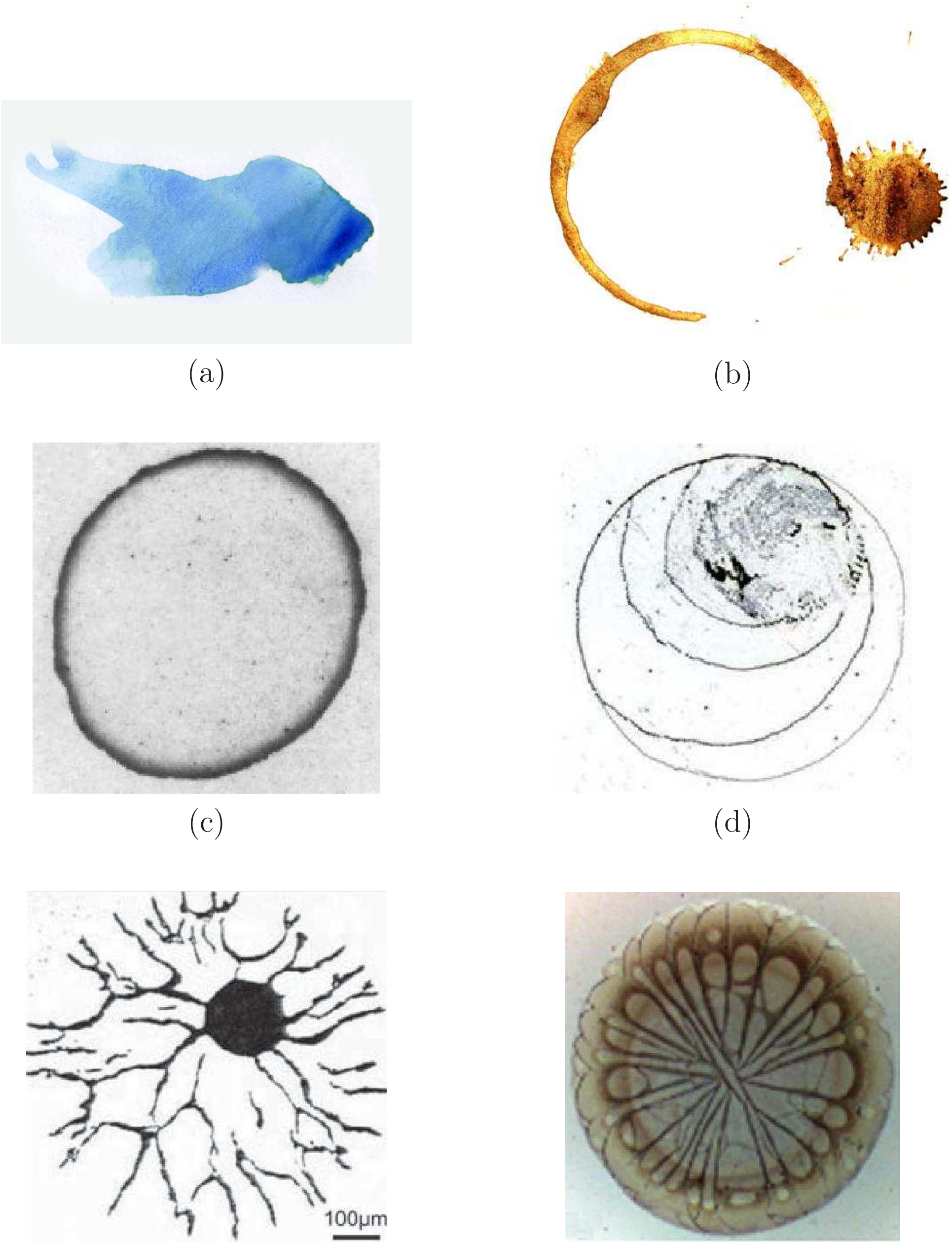

(a) (b)

(c) (d)

(e) (f)

Figure 1.2: Examples of different deposition patterns after complete evaporation of the fluid from droplets of various suspensions (a) A watercolour stain [35]. (b) A coffee stain [110]. (c) A ring stain, reprinted figure with permission from Deegan [52]. Copyright 2000 by the American Physical Society. (d) A stain with multiple rings, reproduced from Askounis *et al.* [5] with permission of The Royal Society of Chemistry. (e) A branched deposition pattern, reprinted with permission from Crivoi and Duan [44]. Copyright 2013 American Chemical Society. (f) A stain of dried blood serum, reprinted from Sefiane [188]. Copyright 2010, with permission from Elsevier.

Deposition pattern	Reference
Rings	Deegan *et al.* [51, 53]
	Deegan [52]
	Hu and Larson [99]
	Chon *et al.* [39]
	Li *et al.* [123, 124, 125]
	Maki and Kumar [133]
	Marín *et al.* [135]
	Baldwin *et al.* [11]
	Eral *et al.* [66, 67]
	Hampton *et al.* [92]
	Crivoi and Duan [45]
	Msambwa *et al.* [146]
	Nguyen *et al.* [151]
	Yunker *et al.* [251]
	Jung *et al.* [105]
	Shin *et al.* [207]
	Wray *et al.* [244]
	Yoo and Kim [247]
Multiple rings	Adachi *et al.* [1]
	Deegan [52]
	Shmuylovich *et al.* [210]
	Maheshwari *et al.* [132]
	Moffat *et al.* [144]
	Askounis *et al.* [5, 6, 7]
	Li *et al.* [127]
	Nguyen *et al.* [151]
Fractal/Branched patterns	Crivoi and Duan [44, 45, 46]
	Dutta *et al.* [64]
	Hadj-Achour and Brutin [90]
Columns	Baldwin *et al.* [10, 11]
Conical structures	Willmer *et al.* [243]
	Baldwin *et al.* [10]
Spheres	Marín *et al.* [136]
Annuli and Domes	Wang and Evans [240, 241]
	Zhang *et al.* [253]
Disks	Wang and Evans [240, 241]
	Yunker *et al.* [251]
Other deposit patterns	Ristenpart *et al.* [175]
	Sefiane [188]
	Brutin and Sobac [27]
	Bou Zeid and Brutin [24]
	Bou Zeid *et al.* [25]
	Brutin [28]
	Carle and Brutin [34]
	Choudhury *et al.* [40]
	Crivoi and Duan [45]
	Doganci *et al.* [58]
	Zhang and Evans [254]
	Baldwin and Fairhurst [12]
	Sobac and Brutin [217]
	Shin *et al.* [207]
	Yoo and Kim [247]

Table 1.1: Examples of deposition patterns observed after complete evaporation of the fluid from droplets of various suspensions

For these reasons evaporation has been the focus of extensive theoretical and experimental investigations by many research groups in many countries in recent years.

In this chapter we shall first describe experimental investigations of the evaporation of sessile fluid droplets in section 1.2. The effects of properties of the substrate on sessile fluid droplets, specifically on the contact angles of sessile fluid droplets, where the contact angle is the angle between the tangent to the solid substrate and the tangent to the free surface measured through the fluid at the contact line, are described in section 1.3. The effects of properties of the substrate on the evaporation of these droplets, resulting in various modes of evaporation, are described in section 1.4. The following sections will focus on modelling the evaporation of sessile fluid droplets in cases when the evaporation of droplets is controlled by the diffusion of vapour into the surrounding atmosphere. In particular, the local evaporative flux and the total evaporative flux will be modelled in subsection 1.5.1. The validity of this model and other effects that may influence the evaporation of a droplet are addressed in subsection 1.5.2. The time at which a droplet evaporates completely, *i.e.* the lifetime of the droplet when all the fluid has escaped from the droplet by converting into vapour, is discussed in section 1.6.

1.2 Experimental Investigations of the Evaporation of Sessile Droplets

Many authors have investigated the evaporation of sessile droplets experimentally. Sessile droplets are usually formed using a micro-syringe, whose needle is perpendicular to the substrate. Alternative ways of forming a sessile droplet include using a piezo-electric print head (see Lim *et al.* [128] and Talbot *et al.* [228]) or pumping

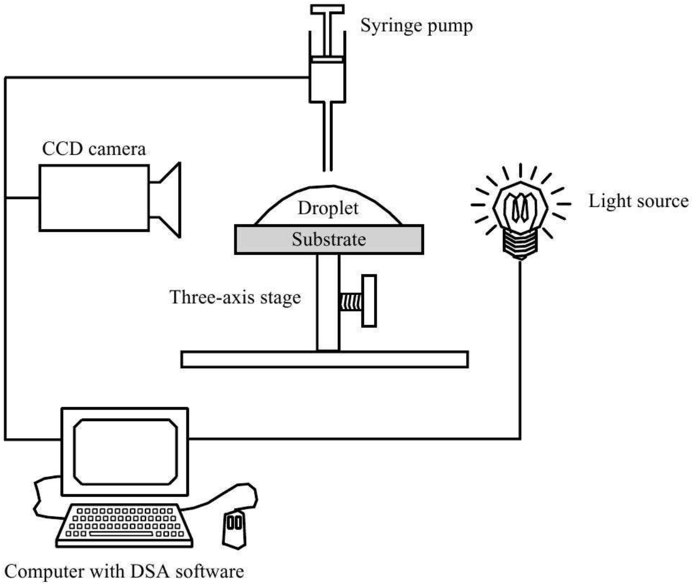

Figure 1.3: Schematic sketch of a typical experimental set-up, including the droplet that is deposited onto the substrate, the syringe, the video camera that is connected to a computer, by Dunn *et al.* [60]. Reproduced with permission from Dunn *et al.* [60]. Copyright 2009 by the Cambridge University Press.

fluid from a reservoir below the substrate through a micro-channel in the substrate (Gleason and Putnam [84]). Once the droplet is formed and left to evaporate a video camera with a suitable magnifying lens connected to a computer is typically used to acquire the evolution of the droplet profile. A schematic sketch of a typical experimental set-up is given by Dunn *et al.* [60] in figure 1.3. With the help of appropriate computer algorithms, which fit the contour of the droplet profile, the droplet profile is processed to determine the contact radius, *i.e.* the distance between the centre of the droplet on the substrate and the contact line, and contact angle [239, pp. 115–116]. Note, however, that because of the fitting and because sessile droplets are not necessarily axisymmetric, errors in the measurements for the contact angle and the contact radius inevitably occur. Furthermore, in extreme cases it is difficult to make exact measurements; in particular, when contact angles are larger than 175° they can scarcely be distinguished from 180°, and when they are smaller than 5°, they can scarcely be distinguished from 0° (see Wakeham *et al.* [239, p. 117]). Therefore, as the droplet evaporates and its volume decreases, it becomes increasingly difficult to make exact measurements of the droplet profile. It is, therefore, usually not possible to determine accurately the lifetime of a droplet in experiments. Even though errors in the measurements are inevitable, they are usually small, so that the above described method is the most commonly used method to investigate the evaporation of sessile droplets experimentally.

In experiments a wide range of fluids have been used, most often water and alcohol (both with and without suspended particles), but liquid crystals (see Poulard and Cazabat [169]), ceramic suspensions (see Zhang *et al.* [252]), binary fluids (see Sefiane *et al.* [180], Sefiane [182], Christy *et al.* [41]), and biological fluids (see Sobac and Brutin [217]) have also been used.

Besides using different fluids and suspensions, various experiments have been undertaken in which droplets were left to evaporate in different conditions, such as in a saturated atmosphere (see Shanahan [202]), in a reduced pressure atmosphere (see Sefiane [181] and Sefiane *et al.* [187]), when the droplet is confined by a sector-shaped boundary (see Popov and Witten [164, 165]), or between two sometimes parallel plates, (see Han and Lin [93]), and in an electric field (see Annapragada *et al.* [4], Orejon *et al.* [154], and Vancauwenberghe *et al.* [237]).

A considerable number of investigations have focused on various types of substrates onto which droplets are deposited and left to evaporate. Most commonly, droplets are left to evaporate on solid substrates, such as silicon, metals, and plastics, which may be coated, so that substrates are usually rigid, impermeable and insoluble. However, other types of substrates have been used. For example, the substrates can be soluble (see Dupas *et al.* [63]), soft but incompressible (see Limat *et al.* [129]), covered with a liquid layer (see Gelderblom *et al.* [80]), or made of gel (see Kajiya *et al.* [107, 108]). The effect of thermal conductivity of the substrate on the evaporation of sessile droplets has been studied by, for example, Dunn *et al.* [59, 60, 61, 62] and Semonov *et al.* [190].

Although droplets on un-heated substrates can evaporate (*i.e.* substrates that are at ambient temperature) the effect of heating the substrate on the evaporation of droplets has been studied both experimentally and theoretically by, for example, Burelbach *et al.* [30], Girard *et al.* [82, 83], Sefiane [184], Sefiane and Bennacer [186], Benselama *et al.* [15, 16], Brutin *et al.* [27], Karapetsas *et al.* [109], Putnam *et al.* [170], Sobac and Brutin [215, 216], Herbert *et al.* [95], Korenchenko and Beskachko [114], Dash and Garimella [50], Gleason and Putnam [84], and Parsa *et al.* [158].

The effects of properties of the substrate, such as the roughness and the chemical heterogeneity of the substrate, on the evaporation of a sessile fluid droplet will be discussed in the next section.

1.3 Determining the Contact Angle of a Sessile Droplet

When a fluid droplet is deposited onto a solid substrate the fluid may wet the substrate either completely or only partially (see de Gennes [81, pp. 16–17]).

If a fluid wets the substrate completely, the droplet forms a film of nanometre height and a zero contact angle. (For experimental examples of completely wetting fluids see, for example, Cachile *et al.* [31, 32], Poulard *et al.* [168], and Guéna *et al.* [88, 89], and for theoretical investigations of completely wetting fluids see Eggers and Pismen [65]). However, in this thesis only partially wetting fluids will be considered in cases in which surface-tension effects dominate gravitational and viscous effects.

We consider situations in which both the Bond number, $Bo = \rho G V_0^{2/3}/\gamma$, representing the ratio of gravitational and surface-tension effects, and the Capillary number, $Ca = \mu U/\gamma$, representing the ratio of viscous and surface-tension effects, are small; here ρ denotes the density of the fluid, G denotes the gravitational constant, V_0 is the initial volume of the droplet, γ is the interfacial tension of the fluid–atmosphere interface, μ denotes the viscosity of the fluid, and U denotes the typical flow velocity. For example, in experiments conducted by Hu and Larson [96] Bo is of the order 10^{-1} and Ca is of the order 10^{-8} for water droplets with a volume of approximately 1.45 μl.[1] In the limit of small Bond and Capillary numbers, *i.e.* for Bo, $Ca \to 0$, the equations for the shape of the free surface of the droplet and the flow inside the droplet decouple. Referred to a cylindrical polar coordinate (r, z) system with origin on the horizontal substrate at the centre of the axisymmetric droplet, the droplet always has the shape of a spherical cap (shown in figure 1.4) with radius $\mathcal{R} = \mathcal{R}(t)$ ($\mathcal{R} \geq R$), contact radius $R = R(t)$ ($R \geq 0$), and contact angle $\theta = \theta(t)$ ($0 \leq \theta \leq \pi$), and its free surface, denoted by $z = h(r, t)$, is given by

$$h = -\mathcal{R}\cos\theta \pm \sqrt{\mathcal{R}^2 - r^2}, \quad \text{where} \quad \mathcal{R} = \frac{R}{\sin\theta}, \tag{1.1}$$

where t denotes time. Note that the physically relevant (*i.e.* the non-negative) part of h given by (1.1) is a single-valued function of r for $0 \leq r \leq R$ when $0 \leq \theta \leq \pi/2$ and for $0 \leq r < R$ when $\pi/2 < \theta \leq \pi$ (in which case only the "+" sign is relevant), but a double-valued function of r for $R \leq r < \mathcal{R}$ when

---

[1] Note, Hu and Larson [96] actually report Bo to be of the order 10^{-2}. The difference in the values of Bo comes from the fact that Hu and Larson [96] use a slightly different definition of Bo, namely $Bo = \rho G R h_0/\gamma$, where R is the contact radius of the pinned droplet and h_0 is the initial height of the droplet measured at the centre of the droplet.

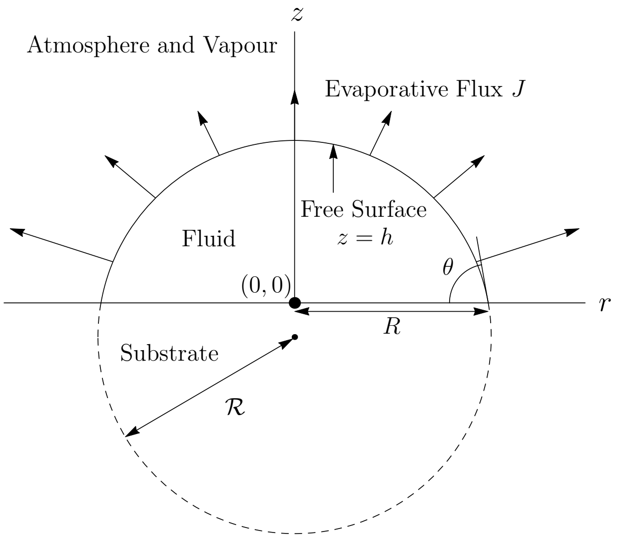

Figure 1.4: Geometry of the mathematical model. The free surface of the drop, $z = h$, is a spherical cap with radius $\mathcal{R}$, contact radius R, and contact angle θ (drawn for $\theta < \pi/2$). The arrows indicate the local evaporative flux, J, which will be modelled in subsection 1.5.1.

$\pi/2 < \theta \leq \pi$ (in which case the "+" and "−" signs correspond to the upper and lower hemispheres, respectively). The volume of the droplet, $V = V(t)$, is given by

$$V = 2\pi \int_0^R h\, r\, \mathrm{d}r = \frac{\pi R^3}{3} \frac{\sin\theta(2 + \cos\theta)}{(1 + \cos\theta)^2}, \tag{1.2}$$

and so, in particular, the initial volume, V_0, is given by

$$V_0 = \frac{\pi R_0^3}{3} \frac{\sin\theta_0(2 + \cos\theta_0)}{(1 + \cos\theta_0)^2}. \tag{1.3}$$

Using a horizontal force balance at the contact line, Young [248] showed that when a sessile fluid droplet is in equilibrium on an ideal substrate, *i.e.* a perfectly smooth, chemically homogeneous, rigid, impermeable, and insoluble substrate (see, for example, Wakeham *et al.* [239, pp. 106–118]), then the equilibrium contact

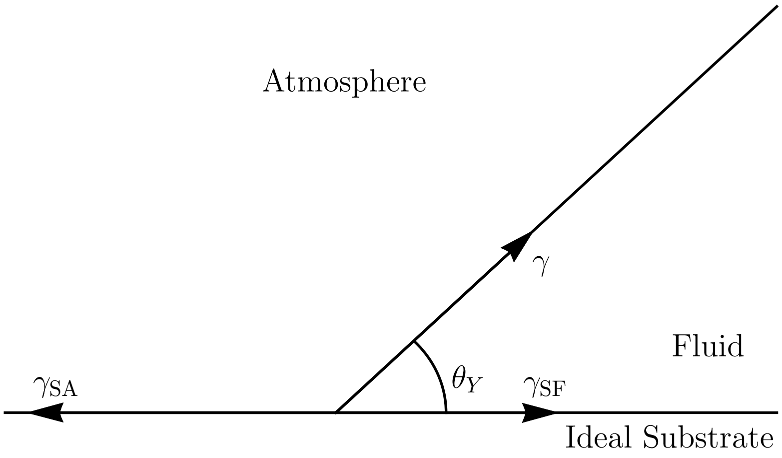

Figure 1.5: Sketch of the region near the contact line of a droplet deposited onto an ideal substrate whose equilibrium contact angle θ_Y can be determined by the classical Young–Laplace law (1.4).

angle of the droplet $\theta = \theta_Y$ can be determined by the classical Young–Laplace law

$$\gamma \cos\theta_Y = \gamma_{\mathrm{SA}} - \gamma_{\mathrm{SF}}, \tag{1.4}$$

where γ, γ_{SA} and γ_{SF} are the interfacial tensions of the fluid–atmosphere, substrate–atmosphere and substrate–fluid interfaces, respectively, as sketched in figure 1.5. In particular, equation (1.4) shows that for a droplet deposited onto an ideal substrate, the equilibrium contact angle θ_Y is unique.

However, in practice, substrates are not ideal, but are to some extent rough and/or chemically heterogeneous. Evaporation on such substrates has been studied both theoretically and experimentally by many authors, including Cazabat and Stuart [36], Shanahan [198, 199, 200], Wakeham *et al.* [239], Diehl [55], and Jansen *et al.* [101]. In particular, Wakeham *et al.* [239, pp. 106–118], for example, state that for a droplet deposited onto a rough substrate it is necessary to differentiate between the actual contact angle, which is the angle between the tangent to the free surface and the tangent to the actual/local substrate and which is the equilibrium

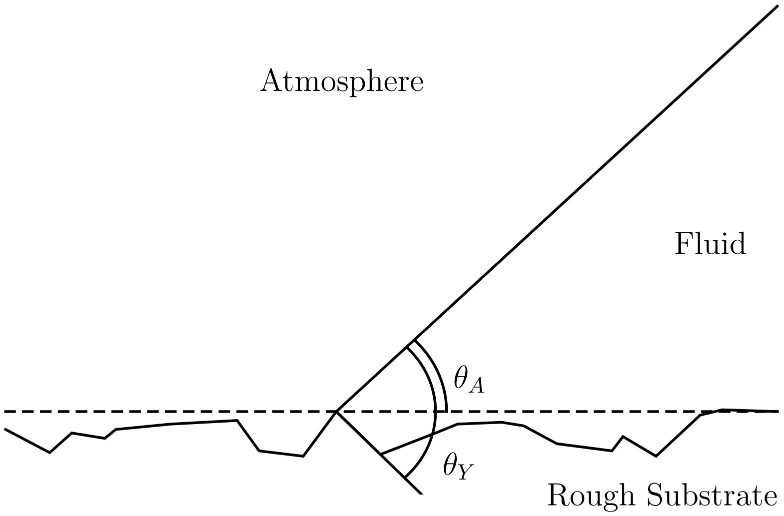

Figure 1.6: Sketch of the actual contact angle, θ_Y, and the apparent contact angle, θ_A, which is measured in experiments, for a droplet deposited onto a rough substrate.

contact angle, θ_Y, given by equation (1.4), and the apparent contact angle, θ_A, which is the angle between the tangent to the free surface and the tangent to the nominal substrate, measured macroscopically. In practice only the apparent contact angle, θ_A, is measured in experiments, and it can be very different from θ_Y (see figure 1.6). In the present work the contact angle always refers to the apparent contact angle, *i.e.* $\theta := \theta_A$, unless specified differently.

Furthermore, when a droplet is deposited onto a real substrate, the contact angle may not be unique, since θ_A can achieve a range of stable equilibrium values, because the contact line is pinned by surface roughness and/or chemical heterogeneities. The largest possible equilibrium contact angle is called the advancing contact angle, θ_{adv} (with $\theta_A \leq \theta_{\text{adv}}$), since for contact angles larger than this angle the contact line advances, and the smallest possible equilibrium contact angle, θ_{rec} (with $\theta_A \geq \theta_{\text{rec}}$), is called the receding contact angle, since for contact angles smaller than this angle the contact line recedes (see, for example, Wakeham *et al.* [239]). The difference between θ_{adv} and θ_{rec} is called contact angle hysteresis and has been studied by many authors such as Adam and Jessop [2], Good [85], Johnson and Dettre [103, 104], Joanny and de Gennes [102], Erbil *et al.* [69], de Gennes *et al.* [81], McHale *et al.* [141], Tadmor [227], Ramos and Tanguy [172], Wakeham *et al.* [239], Eral *et al.* [68], and Pittoni *et al.* [162].

When a droplet is deposited onto a real substrate and left to evaporate, it rapidly achieves a quasi-steady initial equilibrium shape with initial radius $\mathcal{R}_0$, initial contact angle θ_0, and initial contact radius R_0 after an unsteady adjustment phase. However, this adjustment phase is usually on a much shorter timescale than the timescale for the complete evaporation process, and therefore it will be neglected for the remainder of this thesis. Note that on a real substrate θ_0 is in the range $\theta_{\mathrm{rec}} \leq \theta_0 \leq \theta_{\mathrm{adv}}$, but is not necessarily equal to θ_Y. When the initial contact angle of a sessile droplet is smaller than 90° or larger than 90°, the substrate is hydrophilic or hydrophobic, respectively. In cases when the initial contact angle of a sessile droplet is larger than 150°, the substrate is superhydrophobic.

1.4 Modes of Evaporation

As we have seen in the previous section, the properties of the substrate can cause the droplet that is deposited onto it to achieve a range of stable equilibrium values of the contact angle θ due to the pinning or de-pinning of the contact line. This results in a variety of modes of evaporation, some of which will be described in this section.

1.4.1 Extreme Modes of Evaporation

Picknett and Bexon [160] identified two “extreme” modes of evaporation, namely the constant contact angle (CA) mode and the constant contact radius (CR) mode,

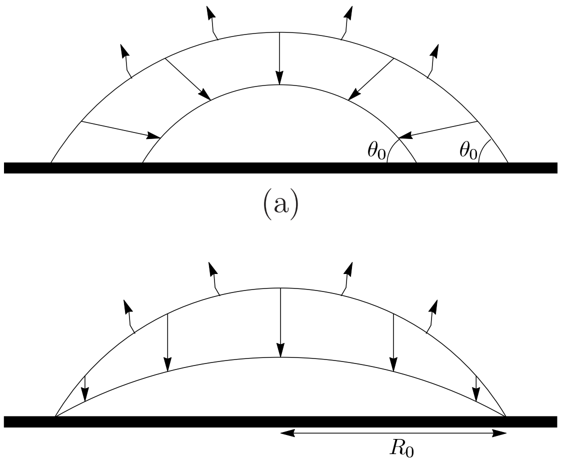

(a)

(b)

Figure 1.7: Sketches of sessile droplets evaporating (a) in the constant contact angle (CA) mode, with $R = R(t)$ decreasing from R_0 to zero and $\theta = \theta_0$ remaining constant, and (b) in the constant contact radius (CR) mode, with $R = R_0$ remaining constant and $\theta = \theta(t)$ decreasing from θ_0 to zero.

which are sketched in figure 1.7.

In particular, they concluded that on an ideal substrate with $\theta_{\rm rec} = \theta_0 = \theta_{\rm adv}$ a droplet evaporates in the CA mode, in which the contact line is always receding (*i.e.* the contact radius $R = R(t)$ decreases with time t from R_0 to zero, whence it has evaporated completely) and the contact angle $\theta = \theta_0$ remains constant. Note that, as shown in the previous section, for a droplet deposited onto an ideal substrate the equilibrium contact angle is unique and therefore $\theta_0 = \theta_Y$.

The other extreme mode of evaporation is the CR mode, in which the contact line is always pinned (*i.e.* the contact radius $R = R_0$ is constant) and the contact angle $\theta = \theta(t)$ decreases with time t from θ_0 to zero, whence it has evaporated completely. A droplet deposited onto a real substrate with $\theta_{\rm rec} = 0$ evaporates in a CR mode. As shown in the previous section, on a real substrate the contact angle θ can achieve a range of stable equilibrium values given by $\theta_{\rm rec} \leq \theta \leq \theta_{\rm adv}$ (and hence $\theta_{\rm rec} \leq \theta \leq \theta_0$), because the contact line is pinned by surface roughness and/or chemical heterogeneities; therefore, for a droplet deposited onto a real substrate with $\theta_{\mathrm{rec}} = 0$ the contact line is always pinned, so that the droplet evaporates in the CR mode.

Picknett and Bexon [160] and many subsequent authors (for example, Coutant and Penski [42], Birdi *et al.* [20], Birdi and Vu [21], Parisse and Allain [157], Erbil *et al.* [70], Poulard *et al.* [167], Bhardwaj *et al.* [19], Kulinich and Farzaneh [116], Shin *et al.* [205, 206], Sobac and Brutin [214, 215, 216], Song *et al.* [218], Weon *et al.* [242], Gelderblom *et al.* [78], Shanahan *et al.* [204], Lim *et al.* [128], Talbot *et al.* [228], Bou Zeid and Brutin [24], Pittoni *et al.* [161, 162], Dash and Garimella [50], and Gatapova *et al.* [77]) have shown that in experiments droplets often evaporate with a constant contact radius or a constant contact angle for most or all of their lifetimes.

In Chapter 2 we will discuss the evolution of droplets in the extreme modes in greater detail.

1.4.2 Stick-Slide Mode of Evaporation

While the extreme modes can be observed, Picknett and Bexon [160] also showed that in practice a sessile droplet may not necessarily evaporate in one of the two extreme modes, but it can evaporate in a variety of modes. Perhaps the most commonly reported mode of evaporation is a stick-slide (SS) mode, which comprises one or more "stick" phases, in which the contact line is pinned, and one or more "slide" phases, in which the contact line is receding.

Various types of SS modes have been observed experimentally. For example, SS modes consisting of a first stick phase, during which the contact radius R is constant, followed by a slide phase, during which the contact angle θ is constant, followed by a second stick phase, and which might be followed by another slide phase during which both R and θ decrease, have been observed experimentally by, for example, Grandas *et al.* [86] and Nguyen *et al.* [151].

A different type of SS mode was observed by Bourgès-Monnier and Shanahan [26] in the case of water droplets evaporating on a polished epoxy substrate; their results are reproduced in figure 1.8, where in stage I the air is saturated and so negligible evaporation occurs, in stage II the droplet evaporates in a stick phase, in which the contact line is pinned, in stage III the droplet evaporates in a first slide phase, in which the contact line is receding and θ is constant, and in stage IV the droplet evaporates in a second slide phase, in which the contact line is receding and θ decreases. In other words this SS mode consists of a single stick phase (corresponding to stage II) (rather than the two stick phases observed by Grandas *et al.* [86] and Nguyen *et al.* [151]), which is followed by a first slide phase in which R is decreasing but θ is constant (corresponding to stage III), which in turn is followed by a second slide phase in which both R and θ are decreasing (corresponding to stage IV). This SS mode has subsequently been reported by a large number of authors (for example, McHale *et al.* [140], Uno *et al.* [235], Erbil *et al.* [69], Mollaret *et al.* [145], Fang *et al.* [73], Soolaman and Yu [219], Fukai *et al.* [76], Anantharaju *et al.* [3], Bhardwaj *et al.* [19], Kajiya *et al.* [106], Li *et al.* [126], Shin *et al.* [205, 206], Dhavaleswarapu *et al.* [54], Dash *et al.* [48], Doganci *et al.* [57], Semenov *et al.* [191, 192, 194], Song *et al.* [218], Lee *et al.* [122], Lim *et al.* [128], Nguyen *et al.* [147], Nguyen and Nguyen [149], Yu *et al.* [249, 250], Dash and Garimella [49], Pittoni *et al.* [161, 162], and Trybala *et al.* [233]).

As this SS mode (which consists of a single stick phase and two slide phases) is perhaps the most commonly reported SS mode, Nguyen and Nguyen [150, 149] and Dash and Garimella [49] constructed a simple yet effective model for this mode of evaporation. In this model the second slide phase is neglected as it is often of relatively short duration compared with the stick and the first slide phases.

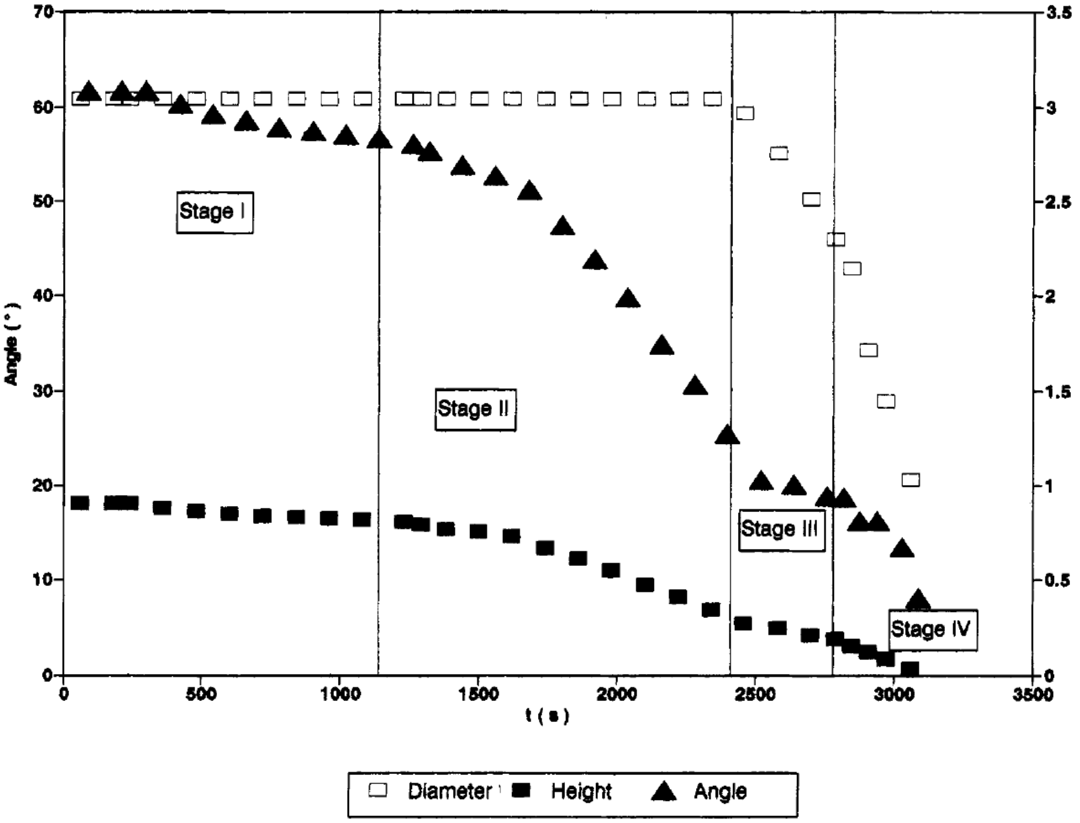

Figure 1.8: Evolutions of the contact diameter ($2R$), height and contact angle θ of an evaporating 4μl sessile water droplet on a polished epoxy substrate taken from Bourgès-Monnier and Shanahan [26]. In stage I the air is saturated and so negligible evaporation occurs, in stage II the droplet evaporates in a stick phase, in which the contact radius is pinned, in stage III the droplet evaporates in a first slide phase, in which the contact line is receding and θ is constant, and in stage IV the droplet evaporates in a second slide phase, in which the contact line is receding and θ decreases. Reprinted with permission from Bourgès-Monnier and Shanahan [26]. Copyright 1995 American Chemical Society.

Therefore, the droplet initially evaporates in a CR phase with $R = R_0$ and with $\theta = \theta(t)$ decreasing from $\theta = \theta_0$ to the receding contact angle $\theta = \theta_{\mathrm{rec}} := \theta^*$, after which the droplet evaporates in a CA phase with $\theta = \theta_{\mathrm{rec}} := \theta^*$ and with $R = R(t)$ decreasing from R_0 to zero. This model will be used in Chapters 3 and 4 to give a complete description of the lifetimes of droplets evaporating in this SS mode.

While many situations are well described by the SS mode, there are other situations in which the receding of the contact line is not continuous as observed in the SS mode. One of these is the stick-jump mode (SJ) mode described in the next subsection.

1.4.3 Stick-Jump Mode of Evaporation

Table 1.2 lists examples of previously reported situations, such as droplets with suspended particles (including nanoparticles, *i.e.* particles with a diameter between 1–100 nm [29], and DNA) on solid substrates, or pure droplets on pillared substrates (*i.e.* substrates that are patterned with a grid of pillars), chemically patterned substrates (*i.e.* substrates that are patterned to have a varying chemical heterogeneity), heated substrates, or polymer substrates, in which droplets evaporate in what we term a stick-jump (SJ) mode. The SJ mode comprises a number of stick phases, in which the contact line is pinned, and a number of rapid "jump" phases, in which the contact line recedes and the contact angle increases. We introduce the term "stick-jump" mode (also adopted by Dietrich *et al.* [56]) rather than "stick-slip" mode introduced by Shanahan [201] to emphasise that the time in which the contact line recedes is very short compared to the time in which the contact line is pinned. The SJ mode is different from the SS mode in two respects. Firstly, a slide phase in the SS mode may be of a comparable duration to a stick phase, while a jump phase in the SJ mode is of a very short

Occurrence of SJ mode	Reference
Droplets with suspended particles	Adachi *et al.* [1] Shmuylovich *et al.* [210]
Droplets with suspended nanoparticles	Deegan *et al.* [52] Moffat *et al.* [144] Askounis *et al.* [5, 6, 7] Li *et al.* [127] Orejon *et al.* [153]
Droplets with suspended nanoparticles on heated substrates	Parsa *et al.* [158]
Droplets with suspended DNA	Maheshwari *et al.* [132]
Droplets on pillared substrates	McHale *et al.* [142] Kusumaatmaja and Yeomans [117] Xu *et al.* [245]
Droplets on chemically patterned substrates	Kusumaatmaja and Yeomans [117]
Droplets on heated substrates	Shanahan and Sefiane [203] Putnam *et al.* [170]
Droplets on polymer substrates	Bormashenko *et al.* [22]

Table 1.2: References reporting the occurrence of the stick-jump (SJ) mode

duration compared to the stick phases. Secondly, and more importantly, during a slide phase in the SS mode the R and θ remain constant or decrease, while during the rapid jump phase in the SJ mode θ jumps to a higher value and R jumps to a lower value. Figure 1.9 shows examples of droplets evaporating in a SJ mode in the experiments by Orejon *et al.* [153], in which water droplets with various concentrations of TiO_2 nanoparticles (namely, 0.1%, 0.05%, 0.025% and 0.01%) were left to evaporates on CYTOP under ambient conditions. In particular, figure 1.9 shows that the higher the concentration of TiO_2 nanoparticles, the more pronounced is the SJ mode, *i.e.* during a stick phase R has a smaller drift and the jumps in the values for θ during the jump phases are more significant. It also shows that for a higher concentration of TiO_2 nanoparticles, there are fewer jump phases. Thus, the presence of nanoparticles significantly influences the pinning, de-pinning and re-pinning of the contact line.

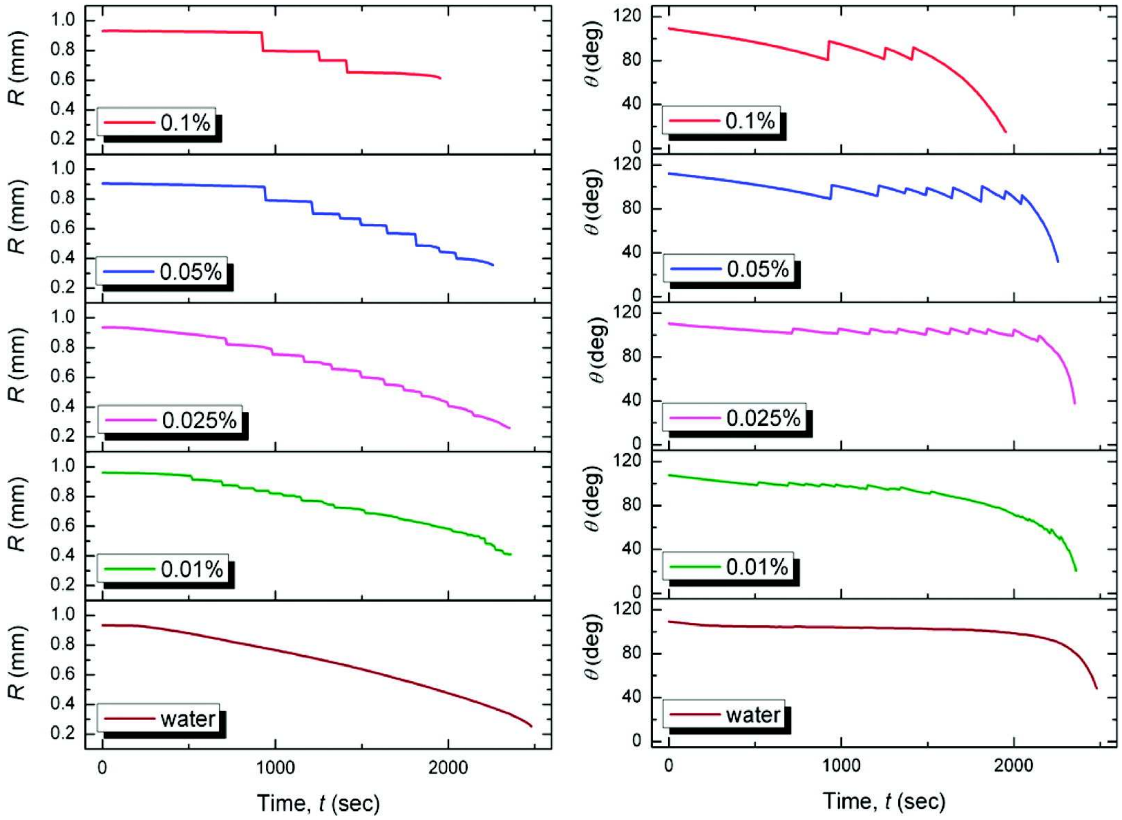

Figure 1.9: Evolutions of the contact radius, R, and contact angle, θ, of $3\,\mu$l sessile water droplets with various concentrations of TiO_2 nanoparticles (namely, 0.1%, 0.05%, 0.025% and 0.01%) on CYTOP evaporate in a SJ mode with different numbers of stick and jump phases measured by Orejon *et al.* [153]. Reprinted with permission from Orejon *et al.* [153]. Copyright 2011 American Chemical Society.

Various authors have investigated both theoretically and experimentally the pinning, de-pinning, and re-pinning of the contact line of a droplet. Adachi *et al.* [1] developed a model for de-pinning and re-pinning of the contact line of a water droplet with suspended particles and concluded that the SJ mode results from a competition between the surface tensions and the friction force at the contact line. Sefiane and Tadrist [183] investigated experimentally the de-pinning of the contact line of a volatile droplet on a rough substrate by considering the influence of a reduced atmospheric pressure, various substrate temperatures, and the presence of surfactants. Rio *et al.* [174] and Berteloot *et al.* [18] observed de-pinning and re-pinning of the contact line of droplets with suspended nanoparticles when the droplets are deposited onto a moving substrate and pushed against a fixed wall; by considering the trajectories of the suspended particles near the contact line they modelled the size of the region of deposition of particles. Frastia *et al.* [75] modelled the de-pinning and re-pinning of a contact line through the dependence of the viscosity of the fluid on the particle concentration, and determined how the deposition patterns depend on the evaporation rate and the particle concentration. Recently, Tsoumpas *et al.* [234] considered theoretically and experimentally the pinning and de-pinning of the contact line of a completely wetting fluid droplet at a sharp edge.

While the models described above focus on the behaviour near the contact line, other models consider the droplet as a whole during the pinning, de-pinning, and re-pinning of the contact line. By comparing the droplet before a jump phase and after a jump phase Shanahan [201] developed a simple model for the pinning and de-pinning of the contact line using a Gibbs free energy argument. In particular, he described the change in R during a jump phase and obtained a criterion that determines when the contact line de-pins. Bhardwaj *et al.* [19] proposed criteria for the de-pinning of the contact line of a droplet with suspended particles and numerically solved the Navier-Stokes equation inside the droplet, and heat and mass transport equations for the fluid flow, the local evaporative flux, and the transport of particles. Matar *et al.* [139] and Craster *et al.* [43] developed a model for thin droplets with suspended particles using lubrication theory and numerically computed the particle concentration and the droplet thickness as functions of time. Recently, Dietrich *et al.* [56] modelled the dissolution of sessile alcohol droplets in water by considering the mathematically equivalent problem of an evaporating sessile droplet. In particular, they developed a model for a droplet evaporating in the SJ mode, in which the contact line de-pins once a certain contact angle is achieved and instantaneously jumps and re-pins with a larger contact angle. These models can often be very complex, such that they can be solved only numerically, and/or are valid only in particular circumstances, such as for thin droplets. Therefore, a simple model for the SJ mode, which is very similar to but more general than the model recently derived by Dietrich *et al.* [56], will be derived in Chapter 5 of this thesis, which is used in Chapter 6 to describe the lifetime of a droplet evaporating in the SJ mode.

In the next section we shall describe the mathematical model for the local evaporative flux and the total evaporative flux in cases when the evaporation is controlled by the diffusion of vapour into the surrounding atmosphere, which will be used in the following chapters to describe the evolution of droplets in the extreme modes, the SS mode, and the SJ mode.

1.5 The Diffusion-Limited Model

1.5.1 Modelling the Evaporative Flux

Picknett and Bexon [160] not only contributed substantially to the understanding of various modes of evaporation, but also pioneered the modelling of the evaporation of sessile droplets in a still atmosphere, where the diffusion of vapour is the rate-limiting mechanism. In general, the evaporative flux depends on both the transfer rate of the liquid across the free surface of the droplet and the diffusion of the vapour away from the free surface into the surrounding atmosphere. However, it can be shown that when a droplet evaporates in a still atmosphere the transfer rate across the free surface is typically much faster than the diffusion of vapour into the surrounding atmosphere. For example, the timescale for the transfer across the free surface is usually of the order $10^{-10}\,\mathrm{s}$ (see, for example, Popov [166]), whereas the timescale for the diffusion of vapour is of the order R^2/D, where D is the diffusion coefficient of vapour in the atmosphere, which, for example, for the vapour of evaporating sessile water droplets is usually of the order of seconds (see, for example, [51, 53, 96, 166]). Thus, in these situations the diffusion of the vapour into the surrounding atmosphere is the rate-limiting mechanism. Note that the opposite extreme case, in which the transfer rate of the liquid across the free surface of the droplet is the rate-limiting mechanism, is described by the so-called "one-sided" model (see, for example, Burelbach *et al.* [30] and Espin and Kumar [72]), which only accounts for the liquid in the droplet, but not for the vapour in the atmosphere.

Moreover, for sessile droplets evaporating in a still atmosphere, the diffusion of the vapour into the surrounding atmosphere is typically on a much shorter timescale than the adjustment of the shape of the droplet due to evaporation, so that the evaporation process may be considered to be quasi-steady. For example, the non-dimensional ratio of the timescale for the diffusion of vapour (R^2/D) to timescale for the lifetime of a droplet, is of the order $(c_{\mathrm{sat}} - c_\infty)/\rho$, c_{sat} is the saturation vapour concentration, and c_∞ (with $0 \leq c_\infty \leq c_{\mathrm{sat}}$) is the vapour concentration far away from the interface, which is of the order of 10^{-5} for a sessile water droplet (see, for example, [51, 53, 96, 166]).

Picknett and Bexon [160], and many subsequent authors including Deegan *et al.* [51, 53], Hu and Larson [96], and Popov [166] showed that when the diffusion of vapour is the rate-limiting mechanism and the evaporation process may be considered to be quasi-steady, the vapour concentration in the atmosphere, $c = c(r, z, t)$, satisfies Laplace's equation

$$\nabla^2 c = 0, \tag{1.5}$$

subject to the boundary conditions that at the free surface of the droplet the atmosphere is saturated with vapour and so c takes its saturation value, c_{sat}, that far away from the droplet c takes its constant ambient value, c_∞, and that the vapour cannot penetrate the substrate (i.e. $\partial c/\partial z = 0$ on $z = 0$ for $r > R$). In the simplest and most widely-used version of the model, c_{sat}, c_∞, D, and ρ are all constant, which, as will be shown in section 1.5.2, describes many physical situations very well, but may need to be extended in some situations to account for the temperature dependence of c_{sat}.

Deegan *et al.* [51, 53] first reported that the solution for c when c_{sat} is constant was obtained by Lebedev [119], who solved the mathematically equivalent electrostatics problem to (1.5), which they used to elucidate the occurrence of ring-like stains after the evaporation of droplets containing suspended particles, so-called "coffee-ring stains". In particular, the local evaporative flux from the free surface of the droplet, $J = J(r,t)$, defined by $J = -D\mathbf{n}\cdot\nabla c$, where $\mathbf{n}$ is the unit outward normal to the free surface, is given by

$$J = \frac{D(c_{\mathrm{sat}} - c_{\infty})}{R}\left[\frac{1}{2}\sin\theta + \sqrt{2}(\cosh\alpha + \cos\theta)^{3/2} \right.$$
$$\left. \times \int_0^{\infty} \frac{\tau\cosh\theta\tau}{\cosh\pi\tau}\tanh\left[\tau(\pi-\theta)\right] P_{-1/2+i\tau}(\cosh\alpha)\,\mathrm{d}\tau\right], \tag{1.6}$$

where $P_{-1/2+i\tau}(\cosh\alpha)$ denotes the Legendre function of the first kind of degree $-1/2 + i\tau$ and argument

$$\cosh\alpha = \frac{r^2\cos\theta \pm R\sqrt{R^2 - r^2\sin^2\theta}}{R^2 - r^2}, \tag{1.7}$$

where again the "+" and "−" signs correspond to the upper and lower hemispheres, respectively, when $\pi/2 < \theta \leq \pi$. Note, Deegan *et al.* [53] also developed an approximation for the local evaporative flux given in equation (1.6), namely

$$J(r,t) \approx \bar{J}(R,\theta)\left(1 - \frac{r^2}{R^2}\right)^{B_{\mathrm{D}}(\theta)}, \tag{1.8}$$

where $\bar{J}(R,\theta)$ is determined in principle from equation (1.6) and the function $B_{\mathrm{D}} = B_{\mathrm{D}}(\theta)$ is given by

$$B_{\mathrm{D}}(\theta) = \frac{2\theta - \pi}{2\pi - 2\theta}. \tag{1.9}$$

In order to describe the occurrence of ring-like stains Deegan *et al.* [51, 53] considered the contact line $r = R$ and $z = 0$ to be pinned for the complete lifetime of the droplet and focussed on the local evaporative flux near the contact line, namely

$$J \propto (R - r)^{B_{\mathrm{D}}(\theta)}, \tag{1.10}$$

which they derived from (1.8). Equation (1.10) shows that the behaviour of the flux near the contact line depends quantitatively (rather than just qualitatively) on the value of the contact angle. Specifically, when $0 \leq \theta < \pi/2$ then $-1/2 \leq B_{\mathrm{D}}(\theta) < 0$ and so the flux is (integrably) singular at the contact line, when $\theta = \pi/2$ then $B_{\mathrm{D}}(\theta) = 0$ and so the flux is finite at the contact line, and when $\pi/2 < \theta \leq \pi$ then $B_{\mathrm{D}}(\theta) > 0$ and so the flux is zero at the contact line. Deegan *et al.* [51, 53] concluded that for a droplet with contact angle θ in the interval $0 \leq \theta < \pi/2$ a radial flow from the centre of the droplet towards the contact line is necessary to compensate for the theoretically singular (in practice, very large) local evaporative flux in order for the contact line to remain pinned. Suspended particles are carried with this radial flow towards the contact line, leaving a ring-like stain after the droplet has completely evaporated. Since the work of Deegan *et al.* [51] (which has over 2100 citations on the Web of Science on 7th April 2015) many authors have observed these ring-like stains (see table 1.1) and modelled them mathematically, including Popov [166], Lebedev-Stephanov and Vlasov [120], Tarasevich *et al.* [231], Espin and Kumar [72], and Crivoi and Duan [47]. The work of Deegan *et al.* [51, 53] also lead to further investigations into the suppression of ring-like stains by, for example, Eral *et al.* [66, 67], Sempels *et al.* [196], Talbot *et al.* [229], and Wray *et al.* [244], and into the flow inside an evaporating droplet by, for example, Deegan [52], Fischer [74], Ruiz and Black [176], Hu and Larson [97, 98], Tarasevich [230], Sefiane and Cameron [185], Ristenpart *et al.* [175], Berteloot *et al.* [17], Petsi and Burganos [159], Bhardwaj *et al.* [19], Masoud and Felske [137, 138], Hamamoto *et al.* [91], Li *et al.* [127], Marín *et al.* [135], Gelderblom *et al.* [79], He and Duan [94], Manukyan *et al.* [134], Talbot *et al.* [229], Thokchom *et al.* [232], Zhang *et al.* [255], Barash [13], and Huang *et al.* [100]. As we have shown in section 1.3 for droplets for which surface-tension effects dominate gravitational and viscous effects, the equations for the shape of the free surface of the droplet and the flow inside the droplet decouple, and the droplet always has the shape of a spherical cap independent of the flow inside the droplet, which will not be discussed further in this thesis.

Hu and Larson [96] developed another approximation for the local evaporative flux that is similar to the approximate expression (1.8) given by Deegan *et al.* [53], namely

$$J(r,t) \approx \bar{J}(R,\theta)\left(1-\frac{r^2}{R^2}\right)^{B_{\mathrm{HL}}(\theta)}, \tag{1.11}$$

where $\bar{J}(R,\theta)$ is determined from equation (1.6) and the function $B_{\mathrm{HL}} = B_{\mathrm{HL}}(\theta)$ is given by

$$B_{\mathrm{HL}}(\theta) = \frac{\theta}{\pi} - \frac{1}{2}. \tag{1.12}$$

Note that the small angle expansion of $B_{\mathrm{HL}}(\theta)$ is at leading order, but not at first order, the same as the small angle expansion of B_{D}, namely $B_{\mathrm{D}} = -1/2 + \theta/2\pi + O(\theta^2)$ as $\theta \to 0^+$. Hu and Larson [96] compared their approximation for the local evaporative flux (1.11) with the exact solution (1.6) and found good agreement between them. (Note that their actual equation for the exact solution has a typographical error as it is missing a factor of $\sqrt{2}$; see Nguyen and Nguyen [148].) Hu and Larson [96] considered the local evaporative flux J as given by equation (1.6) in the special cases when the contact angle approaches zero or is equal to $\pi/2$ (*i.e.* $\theta \to 0^+$ and $\theta = \pi/2$). At leading order in the limit of small contact angle, $\theta \to 0^+$, the free surface of the droplet is a parabola, namely $h = \theta(R^2 - r^2)/(2R)$, and the local evaporative flux is given by

$$J = \frac{2}{\pi}\frac{D(c_{\mathrm{sat}} - c_{\infty})}{\sqrt{R^2 - r^2}}, \tag{1.13}$$

so that $\bar{J}$ in equation (1.8) is given by $\bar{J} \to 2D(c_{\mathrm{sat}} - c_{\infty})/\pi R$. In the special case $\theta = \pi/2$ the free surface of the droplet is a hemisphere with radius $\mathcal{R} = R$, namely

$h = \sqrt{R^2 - r^2}$, and the local evaporative flux is uniform and given by

$$J = \frac{D(c_{\rm sat} - c_\infty)}{R}, \tag{1.14}$$

so that $\bar{J}$ in equation (1.8) is given by $\bar{J} = D(c_{\rm sat} - c_\infty)/R$.

In the special case $\theta = \pi$ the free surface of the droplet is a complete sphere of radius $\mathcal{R}$ ($\mathcal{R} \geq 0$) with zero contact radius, $R = 0$, namely $h = \mathcal{R} \pm \sqrt{\mathcal{R}^2 - r^2}$, and the expression for the flux (1.6) requires careful interpretation. It is, therefore, more convenient to use Smith and Barakat's [212] solution for the mathematically equivalent electrostatics problem to obtain (after some simplification)

$$J = \frac{D(c_{\rm sat} - c_\infty)}{2\mathcal{R}} \left[1 + \left(\frac{2\mathcal{R}}{h} \right)^{3/2} \int_0^\infty q \tanh q \, J_0 \left(\frac{rq}{h} \right) \exp(-q) \, \mathrm{d}q \right], \tag{1.15}$$

where $J_0(\cdot)$ denotes the Bessel function of the first kind of order zero. In particular, the flux at the apex of the droplet, $r = 0$, is given by

$$J = \frac{D(c_{\rm sat} - c_\infty)}{\mathcal{R}} \mathrm{Catalan}, \tag{1.16}$$

where Catalan $\simeq 0.9160$ is Catalan's constant.

Figure 1.10 shows scaled plots of four droplets given by (1.1) each with the same volume V but different contact angles, namely $\theta = \pi/18 = 10^\circ$ (typical of $0 \leq \theta < \pi/2$), $\theta = \pi/2 = 90^\circ$, $\theta = 17\pi/18 = 170^\circ$ (typical of $\pi/2 < \theta < \pi$), and $\theta = \pi = 180^\circ$, and different scaled contact radii, $R/V^{1/3}$, together with the corresponding scaled local evaporative flux at the free surface, $JV^{1/3}/(D(c_{\rm sat} - c_\infty))$, given by (1.6) or, in the special case $\theta = \pi$, by (1.15), shown by the arrows. In particular, figure 1.10 clearly illustrates the qualitatively different behaviour of the flux near the contact line (observed by Deegan *et al.* [51, 53]) in the cases

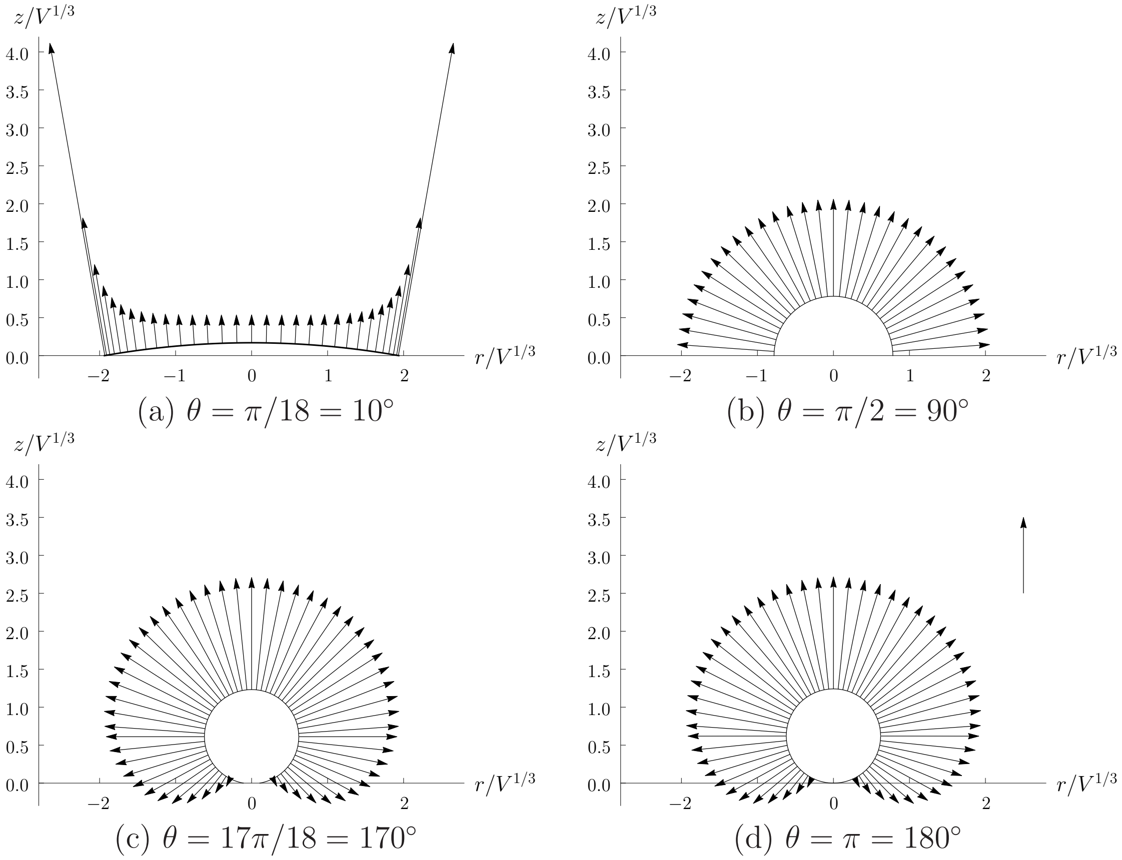

(a) $\theta = \pi/18 = 10^\circ$

(b) $\theta = \pi/2 = 90^\circ$

(c) $\theta = 17\pi/18 = 170^\circ$

(d) $\theta = \pi = 180^\circ$

Figure 1.10: Scaled plots of four droplets given by (1.1) each with the same volume V but different contact angles, namely (a) $\theta = \pi/18 = 10^\circ$, (b) $\theta = \pi/2 = 90^\circ$, (c) $\theta = 17\pi/18 = 170^\circ$, and (d) $\theta = \pi = 180^\circ$, and different scaled contact radii, $R/V^{1/3}$, together with the corresponding scaled local evaporative flux at the free surface, $JV^{1/3}/(D(c_{\mathrm{sat}} - c_\infty))$, given by (1.6) or, in the special case $\theta = \pi$, by (1.15), shown by the arrows. Note that the length of the arrows is proportional to the magnitude of $JV^{1/3}/(D(c_{\mathrm{sat}} - c_\infty))$, with the length of the reference arrow in part (d) corresponding to $JV^{1/3}/(D(c_{\mathrm{sat}} - c_\infty)) = 1$.

$0 \leq \theta < \pi/2$, $\theta = \pi/2$ and $\pi/2 < \theta \leq \pi$ described above. Specifically, figure 1.10 shows that the diffusion-limited model predicts that when $0 \leq \theta < \pi/2$ the flux is largest (theoretically infinite) at the contact line and smallest at the apex of the droplet (*i.e.* at $r = 0$), when $\theta = \pi/2$ the flux is uniform and given by (1.14), and when $\pi/2 < \theta \leq \pi$ the flux is largest at the apex of the droplet and smallest (theoretically zero) at the contact line.

Snow [213], who considered the mathematically equivalent electrostatics problem, first gave a series solution for the total evaporative flux from the droplet at any instant. Over fifty years later, Popov [166] integrated the flux J given by (1.6) over the free surface of the droplet, and was able to give an exact expression (not involving any series) for the total evaporative flux from the droplet at any instant, from which the rate of change of the volume of the droplet $\mathrm{d}V/\mathrm{d}t$ is derived, namely

$$\frac{\mathrm{d}V}{\mathrm{d}t} = \frac{1}{\rho}\int_A J\mathrm{d}A = -\frac{\pi R D(c_{\mathrm{sat}} - c_\infty)}{\rho}\frac{g(\theta)}{(1+\cos\theta)^2}, \tag{1.17}$$

where A is the surface of the droplet, V is given in terms of R and θ by (1.2), and the function $g = g(\theta)$ is defined by

$$g(\theta) = (1+\cos\theta)^2\left\{\tan\frac{\theta}{2} + 8\int_0^\infty \frac{\cosh^2\theta\tau}{\sinh 2\pi\tau}\tanh\left[\tau(\pi-\theta)\right]\,\mathrm{d}\tau\right\}, \tag{1.18}$$

and is plotted in figure 1.11. In particular, the function g satisfies $g(0) = 16/\pi$, $g(\pi/2) = 2$, and $g \sim (\pi-\theta)^3\log 2 \to 0^+$ as $\theta \to \pi^-$. Moreover, Popov [166] confirmed the asymptotic results for the local evaporative flux (1.13) and (1.14) given by Hu and Larson [96]. He then used these expressions to predict the height and width of the ring-like stain of the deposited particles.

There are several approximations for rate of change of the volume of the droplet,

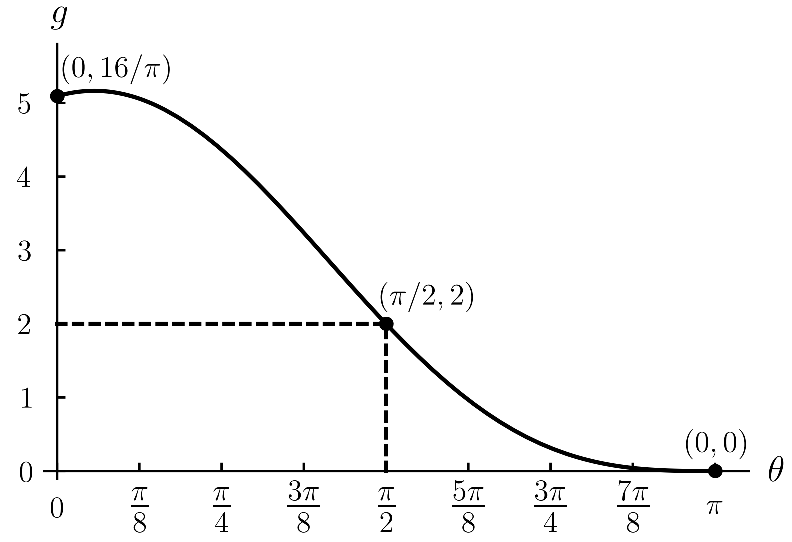

Figure 1.11: The function $g = g(\theta)$ as a function of the contact angle θ, as given by equation (1.18).

$\mathrm{d}V/\mathrm{d}t$. In this thesis we shall describe two of them in more detail, namely the ones by Picknett and Bexon [160] and by Hu and Larson [96]. Picknett and Bexon [160] fitted Snow's series solution [213] for $\mathrm{d}V/\mathrm{d}t$ to develop an approximation for $\mathrm{d}V/\mathrm{d}t$, namely

$$\frac{\mathrm{d}V}{\mathrm{d}t} = -\frac{2\pi D(c_{\mathrm{sat}} - c_{\infty})\mathcal{R}}{\rho} f(\theta), \tag{1.19}$$

where the function $f = f(\theta)$ is given by

$$f(\theta) = \begin{cases} 0.6366\theta + 0.09591\theta^2 - 0.06144\theta^3 & \text{for } 0 \leq \theta < 0.175, \\ 8.957 \times 10^{-5} + 0.6333\theta + 0.1160\theta^2 & \\ -0.08878\theta^3 + 0.01033\theta^4 & \text{for } 0.175 \leq \theta \leq \pi. \end{cases}$$

They then used this approximation to predict the evolution of the contact angle θ in the CR mode as well as the loss of mass of the droplet over time, and the lifetimes and half-lives (that is, the time taken for a droplet to evaporate to half of its initial volume) as functions of the initial contact angle θ_0 in the two extreme modes, as shown in figure 1.12. Furthermore, they compared the predicted scaled half-lives

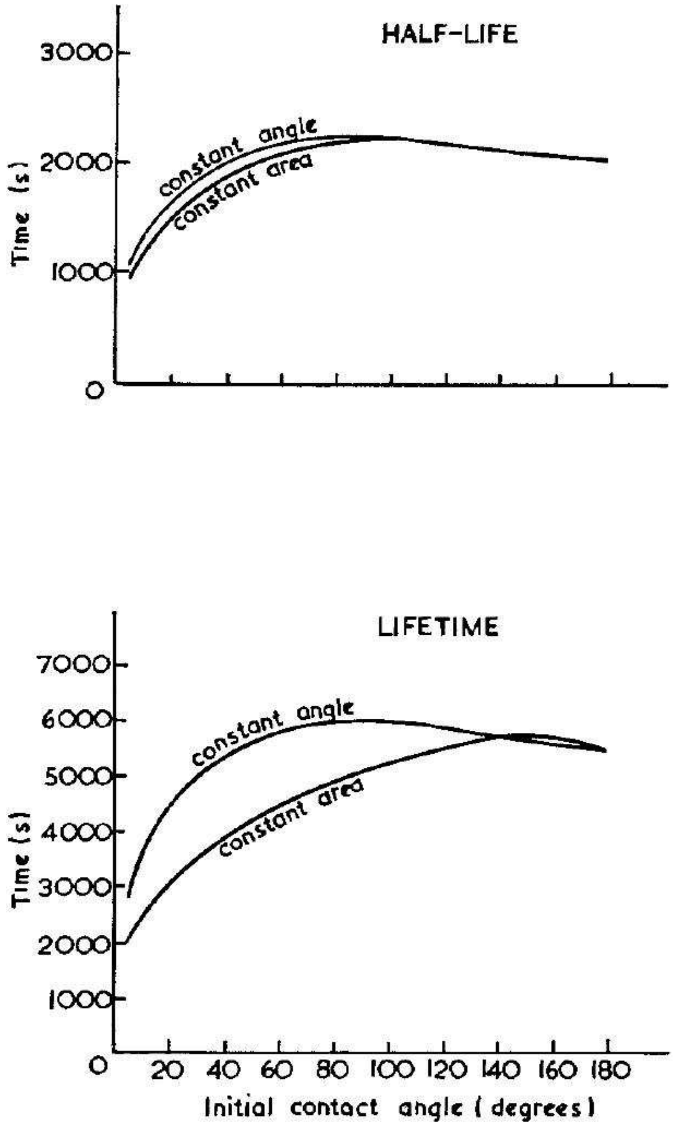

Figure 1.12: Theoretically predicted lifetimes and half-lives of 1 mg methylacetate droplets evaporating in the CR mode (denoted by "constant area" mode) and in the CA mode (denoted by "constant angle" mode) as functions of the initial contact angle calculated by Picknett and Bexon [160]. Note, the curves representing the lifetimes of droplets evaporating in the extreme modes are not drawn for small contact angles. Reprinted from Picknett and Bexon [160]. Copyright 1977, with permission from Elsevier.

with their experimental data for droplets with initial contact angles in the range 30°–70° evaporating in the two extreme modes and found good agreement between them (with percentage errors between the model predictions and the experimental results smaller than 18%).

On the other hand Hu and Larson [96] used their approximation for the local evaporative flux (1.11) to obtain an approximation for $\mathrm{d}V/\mathrm{d}t$, namely

$$\frac{\mathrm{d}V}{\mathrm{d}t} = -\frac{\pi D(c_{\mathrm{sat}} - c_{\infty})R}{\rho}(0.27\theta^2 + 1.30). \tag{1.20}$$

Note that this approximation is valid only for $0 \leq \theta \leq \pi/2$ (see [96, 148, 228]). Hu and Larson [96] compared their approximation for $\mathrm{d}V/\mathrm{d}t$ with the approximation (1.19) given by Picknett and Bexon [160] and with experimental data for a water droplet evaporating on a glass substrate with $\theta_0 \approx 0.73 \simeq 41.8°$, and found good agreement between them all.

Figure 1.13 gives the error (in %) between the approximations for $\mathrm{d}V/\mathrm{d}t$ as functions of the contact angle θ given by Picknett and Bexon [160], namely equation (1.19), and Hu and Larson [96], namely equation (1.20), and the exact solution for $\mathrm{d}V/\mathrm{d}t$ as given by Popov [166], namely equation (1.17). In particular, it shows that the approximation by Hu and Larson [96], given by equation (1.20), is indeed a good approximation for contact angles in the range $0 \leq \theta \leq \pi/2$, with absolute percentage errors smaller than 2.4%; however, for contact angles $2.29 \simeq 131.3° \lesssim \theta \leq \pi$ the percentage error between the approximation and the exact solution is larger than 20%. Figure 1.13 also shows that the approximation by Picknett and Bexon [160], given by equation (1.19), is an excellent approximation for all contact angles, *i.e.* $0 \leq \theta \leq \pi$, with absolute percentage errors smaller than 0.15%. However, the approximation by Picknett and Bexon [160] has the slight disadvantage that it is piecewise defined, which makes computations more

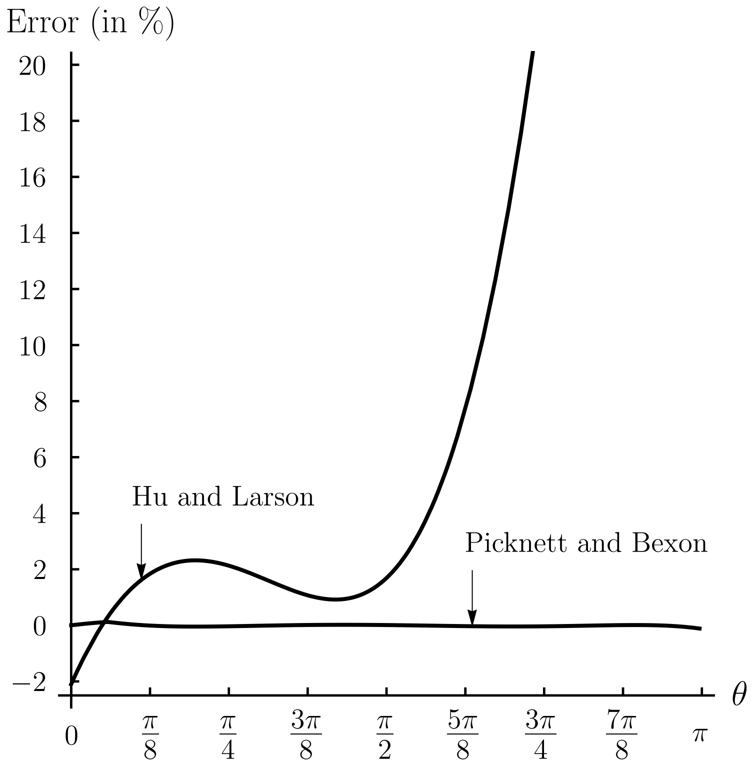

Figure 1.13: The error (in %) between the approximations for $\mathrm{d}V/\mathrm{d}t$ as functions of the contact angle θ, given by Picknett and Bexon [160], namely equation (1.19), and Hu and Larson [96], namely equation (1.20), and the exact solution for $\mathrm{d}V/\mathrm{d}t$ as given by Popov [166], namely equation (1.17).

inconvenient. Therefore henceforth only the exact solution for the rate of change of the volume of the droplet, $\mathrm{d}V/\mathrm{d}t$, derived by Popov [166] and given by equation (1.17) will be used.

1.5.2 Validation and Extensions of the Diffusion-Limited Model

Since Picknett and Bexon [160] first described the diffusion-limited model for evaporating droplets in a still atmosphere, many authors have shown that many situations are well described by this model, but also that sometimes it needs to be modified and extended in order to include other physical effects, such as evaporative cooling that occurs because latent heat (the energy required for the phase change of fluid into vapour) is obtained from the thermal energy of the droplet, substrate, and the atmosphere and/or the convection of vapour in the atmosphere.

Table 1.3 gives a list of authors who compared experimental results with the prediction of the simplest version of the diffusion-limited model, in which c_{sat} (as well as c_∞, D, ρ) is assumed to be constant, for droplets in the CA, CR, and SS modes with contact angles ranging from approximately zero to approximately 150° and concluded that there is good agreement between them. This good agreement between experimental results and the model predictions has led to wide usage of the simplest version of the diffusion-limited model.

Table 1.3 also shows that Gelderblom *et al.* [78] and Talbot *et al.* [228], who reported the evaporation of water droplets on carbon nanofibre on silicon substrates and on silicon substrates, respectively, with initial contact angles of up to $\theta_0 \simeq 150^\circ$, found good agreement between the predictions of the simplest version of the model and their experiments and concluded that the effect of evaporative cooling is negligible in these experiments. On the other hand, Dash and Garimella

Reference	Mode of Evaporation	Range of Contact Angle θ
Coutant and Penski [42]	CA mode	40°–100°
Erbil *et al.* [70]	CA mode	35°–45°
Bhardwaj *et al.* [19]	CR mode	0°–20°
	SS mode	15°–30°
Shin *et al.* [205]	CR mode	0°–60°
Doganci *et al.* [57]	SS mode	30°–100°
Gelderblom *et al.* [78]	CR mode	10°–150°
Semenov *et al.* [191]	SS mode	20°–90°
Sobac and Brutin [214]	CR mode	20°–135°
Song *et al.* [218]	CR mode	15°–60°
	SS mode	25°–100°
Lim *et al.* [128]	CR mode	5°–50°
	SS mode	35°–65°
Nguyen *et al.* [147]	SS mode	25°–110°
Sobac and Brutin [216]	CR mode	5°–70°
Semenov *et al.* [193]	SS mode	20°–85°
Talbot *et al.* [228]	CA mode	10°–100°
	CR mode	20°–150°
Bou Zeid and Brutin [24]	CR mode	5°–15°
Dash and Garimella [49]	SS mode	40°–120°
Semenov *et al.* [194]	SS mode	20°–85°
Singh *et al.* [211]	CR mode	10°–45°
Trybala *et al.* [233]	CR mode	15°–115°
	SS mode	80°–115°
Dash and Garimella [50]	CA mode	30°–120°

Table 1.3: Details of experimental results that are well predicted by the simplest version of the diffusion-limited model, in which c_{sat} is assumed to be constant. In particular, the mode in which the droplets evaporated as well as the range of contact angles that are reported during the evaporation process are listed.

[49, 50] investigated experimentally the evaporation of water droplets with different volumes on (sometimes heated) hydrophobic and (sometimes heated) superhydrophobic substrates. In particular, they observed that water droplets on the superhydrophobic substrate with $\theta_0 \approx 160^\circ$ evaporate always in the CA mode (irrespective of the temperature of the substrate). They found poor agreement between the theoretical predictions of the simplest version of the model and experimental results. They attributed this poor agreement to the fact that the simplest version of the model does not account for the significant evaporative cooling, which they computed for droplets with $\theta_0 \approx 160^\circ$. This discrepancy in the literature suggests that further experiments are necessary to determine if and under what conditions the simplest version of the model is valid for droplets evaporating on superhydrophobic substrates.

In order to account for this significant effect of evaporative cooling Dash and Garimella [49] proposed an ad hoc modification of the simplest version of the model (namely reducing the theoretical prediction of the total evaporative flux by an empirically determined factor of 20%). Following, for example, Dunn *et al.* [59, 60, 61, 62], and Sefiane *et al.* [187] who first incorporated the temperature dependence of c_{sat}, *i.e.* $c_{\mathrm{sat}} = c_{\mathrm{sat}}(T)$, where T is the temperature of the fluid, in the simplest version of the model to account for the effect of evaporative cooling of droplets evaporating on substrates of low conductivity and in a reduced pressure atmosphere, Dash and Garimella [50] and Pan *et al.* [155, 156] incorporated $c_{\mathrm{sat}} = c_{\mathrm{sat}}(T)$ in subsequent publications to account for the observed significant effect of evaporative cooling of droplets on superhydrophobic substrates. In particular, Pan *et al.* [155] compared the predictions of the diffusion-limited model taking $c_{\mathrm{sat}} = c_{\mathrm{sat}}(T)$ into account and those of the simplest version of the model with the experimental data of Dash and Garimella [49]. They found good agreement with experimental data for the predictions of the diffusion-limited model taking $c_{\text{sat}} = c_{\text{sat}}(T)$ into account but not for the simplest version of the model. Since Dunn *et al.* [59, 60, 61, 62], and Sefiane *et al.* [187] the diffusion-limited model taking $c_{\text{sat}} = c_{\text{sat}}(T)$ into account was also used by, for example, Sefiane and Bennacer [189], Lopes *et al.* [131], Saada *et al.* [178], and Gatapova *et al.* [77] to account for the effect of evaporative cooling of droplets evaporating on substrates of low conductivity, on thick substrates, or on heated substrates, respectively, and by Sefiane and Bennacer [189], to account for the effect of evaporative cooling of droplets evaporating in a reduced pressure atmosphere or of evaporating droplets with a high thermal resistance. Recently Gleason and Putnam [84] proposed a different ad hoc modification of the simplest version of the model to account for the evaporative cooling of a droplet on a heated substrate, namely incorporating a prescribed temperature distribution of the free surface of the droplet.

Guéna *et al.* [87], Shahidzadeh-Bonn *et al.* [197], Dunn *et al.* [60], Weon *et al.* [242], Sobac *et al.* [216], and Kelly-Zion *et al.* [113], highlighted the possible importance of incorporating the convection of vapour in the atmosphere into the diffusion-limited model for heptane droplets towards the end of their lifetime, for water droplets, nanosized droplets, droplets on heated substrates, and hexane droplets, respectively. This has lead to the development of extensions of the simplest version of the model, which incorporate the convection of vapour by, for example, Dunn *et al.* [60], Saada *et al.* [177], Kelly-Zion *et al.* [111, 112], and Carle *et al.* [33] have proposed and analysed extensions of the diffusion-limited model which also includes the effects of the convection of the vapour. In particular, they found that the simplest version of the model underestimates the evaporation rate compared to their extensions of the model. Kelly-Zion *et al.* [111, 112], who considered four droplets of hydrocarbons (namely, 3-methylpentane, hexane, cyclohexane, heptane) and eight droplets of hydrocarbons (namely, acetone, 3-methylpentane, hexane, methanol, cyclohexane, isooctane, heptane, and octane), respectively, evaporating on aluminium, and Carle *et al.* [33], who considered ethanol droplets evaporating on heated aluminium, found good agreement between the predictions of the extensions of the diffusion-limited model and experimental results.

Another extension of the simplest version of the model was studied by Lopes *et al.* [131], who assumed that evaporation is not quasi-steady.

Since the simplest version of the model is applicable in many situations (see table 1.3) and it does not require numerical computations to determine the evaporative flux, as most of the previously mentioned extensions (with the exception of that by Dash and Garimella [49]), it is used in this thesis. In particular, the simplest version of the model is used to determine the evolution of an evaporating droplet, and therefore, the lifetime of a droplet.

1.6 Lifetimes of Droplets

In many practical situations being able to predict and influence the lifetime of an evaporating droplet could lead to considerable economic efficiencies. For example, minimising the lifetime of droplets in cooling applications (for example, the cooling of electronics) could lead to a faster cooling process, leading to a reduction in production and energy costs; as another example optimising the lifetimes of droplets containing pesticides could lead to an optimised usage of pesticides with economic as well as environmental benefits. Similarly, optimising the lifetimes of droplets in ink-jet printing applications could lead to faster printing speeds which could increase production speed and hence profits.

As we have already mentioned, Picknett and Bexon [160] were the first to consider the lifetimes (and half-lives) of sessile droplets in the extreme modes of evaporation using an approximate solution for the rate of change of the volume (1.19). In particular, they obtained theoretically predicted lifetimes of 1 mg methylacetate droplets as a function of the initial contact angle, shown in figure 1.12. Picknett and Bexon [160] did not compute the curves representing the lifetimes of droplets evaporating in the extreme modes for small contact angles in figure 1.12, but they showed that for initial contact angles θ_0 satisfying $0 \lesssim \theta_0 \lesssim 140^\circ$, the lifetime of a droplet evaporating in the CR mode is significantly shorter than the lifetime of an initially identical droplet evaporating in the CA mode. They also showed that this is no longer true for initial contact angles θ_0 satisfying $140^\circ \lesssim \theta_0 \leq 180^\circ$, when the lifetime of a droplet in the CR mode is slightly longer than the lifetime of a droplet in the CA mode.

Thirty years after the pioneering work of Picknett and Bexon [160], Schönfeld *et al.* [179] used an approximation to Picknett and Bexon's [160] approximate solution for the the rate of change of the volume of the droplet (1.19) that is valid for $0 \leq \theta_0 \leq \pi/2$ to determine the lifetime of a droplet evaporating in the CR mode. In particular, they found that just as in the CA mode the lifetime of a droplet evaporating in the CR mode is proportional to the initial volume $V_0^{2/3}$ given in equation (1.3).

As mentioned in section 1.4.3, Bhardwaj *et al.* [19] solved numerically the Navier-Stokes equation inside the droplet, and heat and mass transport equations for the local evaporative flux and the evolution of the droplet, from which they predicted lifetime of a droplet in the CR and the SS mode, which they compared to their experimentally determined lifetimes and found good agreement between them.

A different approximation from that of Schönfeld *et al.* [179] was derived by Shanahan *et al.* [204] who investigated experimentally and theoretically the lifetimes of droplets with small initial contact angles ($0 \leq \theta_0 \lesssim 65^\circ$) evaporating in the two extreme modes. However, rather than using the asymptotic result for the local evaporative flux in the limit of small contact angle given by equation (1.13), they used Hu and Larson's [96] approximate solution for the local evaporative flux (1.11) with the additional assumption that $\bar{J}$ is constant in both the CR and the CA mode. Furthermore, they determined the lifetimes of droplets that evaporate in either the CR or the CA mode for most of their lifetime from their experiments [204], or the lifetime of droplets that evaporate in the SJ mode for most of their lifetime, from the experiments by Moffat *et al.* [144] by extrapolating V linearly in t to $V = 0$ (see Nguyen and Nguyen [148]). The comparison between their approximate solutions for the lifetimes of droplets evaporating in the two extreme modes as functions of the initial contact angle and their experimentally determined lifetimes is shown in figure 1.14. In particular, they claimed that the curve representing the approximate lifetime of a droplet evaporating in the CR mode is applicable for initial contact angles in the range $0 \leq \theta_0 \lesssim 20^\circ$, while the curve representing the approximate lifetime of a droplet evaporating in the CA mode is applicable for initial contact angles in the range $45^\circ \lesssim \theta_0 \lesssim 65^\circ$. Furthermore they hypothesised the existence of a sigmoidal transition curve connecting these two curves, representing the lifetimes of droplets evaporating in the SS mode, in which the droplet first evaporates with a pinned contact line but later with a de-pinned contact line.

In contrast to the approximations derived by Shanahan *et al.* [204], Nguyen and Nguyen [148] developed theoretical predictions for the lifetimes of droplets evaporating in the extreme modes that are based on the exact solution of the

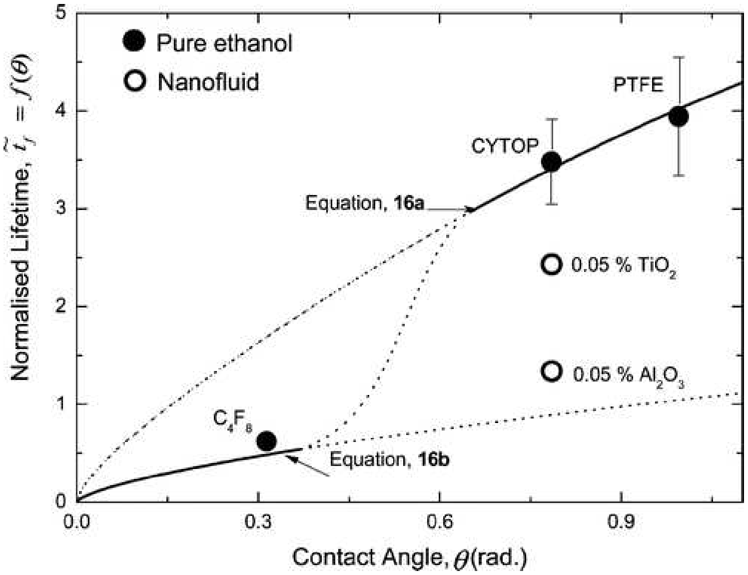

Figure 1.14: Approximate lifetimes of droplets in the extreme modes of evaporation as a function of the initial contact angle (where the solid lines denote the range of validity of the approximations) together with a hypothesised sigmoidal transition curve between them and experimentally determined lifetimes obtained by Shanahan *et al.* [204] and Moffat *et al.* [144]. Reprinted with permission from Shanahan *et al.* [204]. Copyright 2011 American Chemical Society.

diffusion-limited model (see subsection 1.5.1). Their predictions [148, Figure 5] are qualitatively similar to the approximate results reported by Picknett and Bexon [160], which are shown in figure 1.12, but also show that the curves representing the lifetimes of droplets evaporating in the CR and the CA mode coincide at the origin for $\theta_0 = 0$. In order to determine the lifetimes of droplets investigated in experiments by Erbil *et al.* [70], Kulinich and Farzaneh [116], Shin *et al.* [205], and Shanahan *et al.* [204], Nguyen and Nguyen [148] extrapolated $V^{2/3}$ linearly in t to $V = 0$ (as they had proposed in a previous publication [147]). They compared these experimentally determined droplet lifetimes with the predicted lifetimes based on the diffusion-limited model and with the predicted lifetimes based on the approximations derived by Shanahan *et al.* [204]. This comparison shows that the extrapolated droplet lifetimes are predicted well by the diffusion-limited model, but not by the approximations derived by Shanahan *et al.* [204].

Just like Nguyen and Nguyen [148], Talbot *et al.* [228] used the diffusion-limited model described in section 1.5.1 to predict the lifetimes of droplets in the extreme modes. Their experimental data concern picolitre droplets with a large range of initial contact angles, $10° \lesssim \theta_0 \lesssim 150°$, evaporating in both the CA and the CR mode. They did not specify how the experimentally determined lifetimes were calculated, but concluded that for picolitre droplets the diffusion-limited model predicts the experimentally determined lifetimes very well.

In a second publication Nguyen and Nguyen [149] focused on the hypothesised sigmoidal transition curve between the curves representing the lifetimes of droplets in the extreme modes proposed by Shanahan [204]. To this end they developed the simple model for a droplet evaporating in the SS mode described in section 1.4.2, which they used to determine the lifetime of a droplet in this mode. Nguyen and Nguyen [149] state that "[t]he lifetime of the combined mode of evaporation [the SS mode] is constrained by those of the two single modes of evaporation [the extreme modes]," and write (expressed in their notation in their equation (5)) that the lifetime of a droplet evaporating in the CA mode is always longer than or equal to that of a droplet with the same initial shape and volume evaporating in the SS mode, which is itself always longer than that of a droplet with the same initial shape and volume evaporating in the CR mode. Evidently this cannot be true for all values of θ_0, since, as we have already seen, Picknett and Bexon [160] showed that the lifetime of a droplet in the CR mode is slightly longer than the lifetime of a droplet in the CA mode for $140° \lesssim \theta_0 < 180°$. Notwithstanding this, Nguyen and Nguyen [149] used a rational approximation to the function $g(\theta)$, given in (1.18), to compute the lifetimes of droplets in the CR mode and the CA mode as functions of the initial contact angle θ_0 together with lifetimes of droplets in

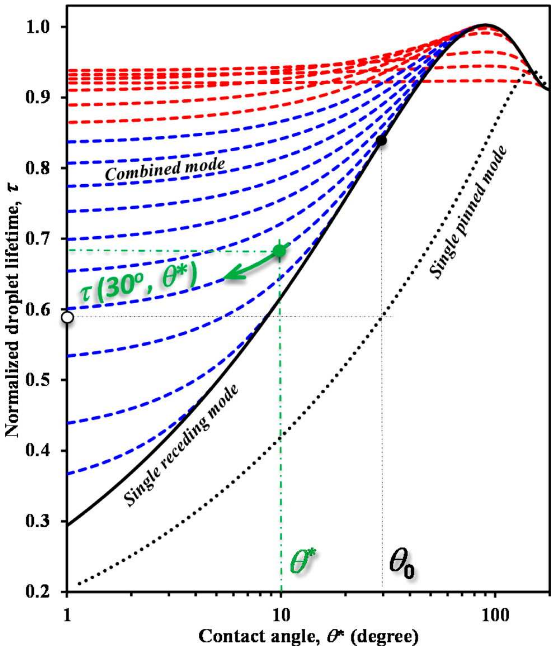

Figure 1.15: Lifetimes of droplets in the CR mode (denoted by "single pinned mode") and the CA mode (denoted by "single receding mode") as functions of the initial contact angle θ_0 together with lifetimes of droplets in the SS mode (denoted by "combined mode") as a function of the receding contact angle, θ^*, where the blue and red dashed lines represent the lifetime of droplets in the SS mode with initial angles $\theta_0 < 90°$ and $\theta_0 > 90°$, respectively, obtained by Nguyen and Nguyen [149]. Reprinted with permission from Nguyen and Nguyen [149]. Copyright 2012 American Chemical Society.

the SS mode as a function of the receding contact angle, θ^*, which are shown in figure 1.15. They observed that figure 1.15 shows that "the lifetime of the combined pinned-receding mode [SS mode] is located outside the confined area between the two limit lines [corresponding to the lifetimes of droplets in the CR mode and the CA mode]" and that their results "do not support the controversial hypothesis in the literature [due to Shanahan *et al.* [204]] that there would be a "sigmoidal" transition line for the droplet lifetime of the combined pinned-receding mode [SS mode] and that the sigmoidal transition line linking the two modes [*i.e.* the CR and CA modes] would be located within the confined area between the limit lines", both of which statements appear to contradict their earlier statement

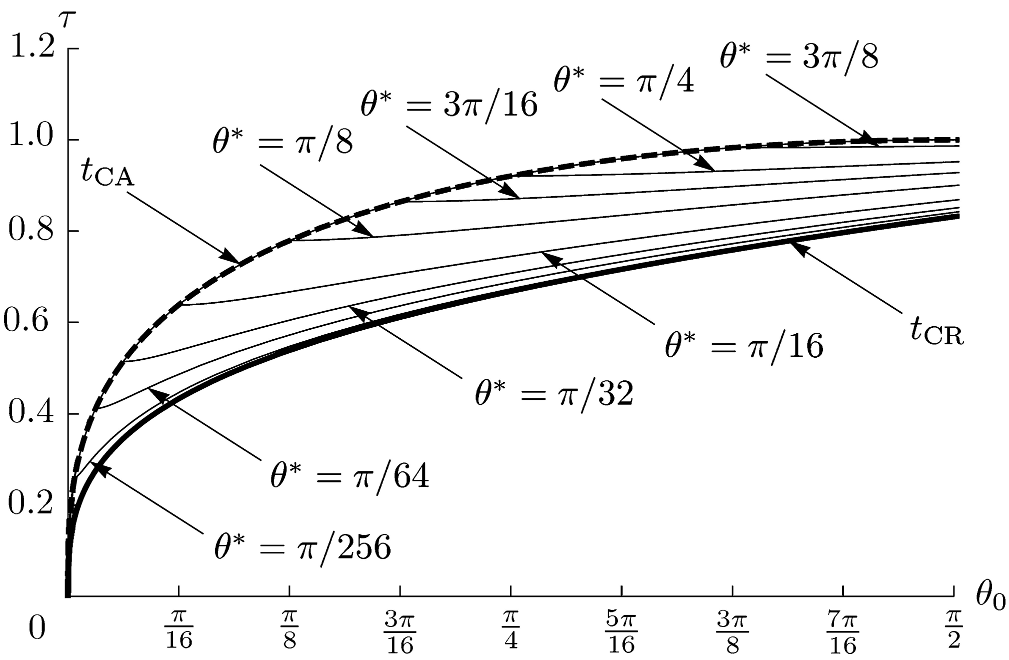

Figure 1.16: Lifetimes of droplets in the CR mode (denoted by t_{CR}) and the CA mode (denoted by t_{CA}) together with lifetimes of droplets in the SS mode for various values of $0 < \theta^* < \pi/2$ as functions of the initial contact angle θ_0 obtained by Stauber *et al.* [220]. Reprinted with permission from Stauber *et al.* [220]. Copyright 2013 American Chemical Society.

that the lifetime of a droplet evaporating in the CA mode is always longer than or equal to that of a droplet evaporating in the SS mode, which is itself always longer than that of a droplet evaporating in the CR mode.

We have shown in our recent comment on their work (Stauber *et al.* [220]) that the apparent contradiction between their statements arises because in figure 1.15, Nguyen and Nguyen [149] plotted the lifetimes of droplets evaporating in the extreme modes as functions of the initial contact angle θ_0 but plotted the lifetime of droplets evaporating in the SS mode as a function of the receding contact angle θ^* for several values of θ_0. To this end we gave in figure 1.16, the lifetimes of droplets evaporating in the CR, CA, and SS mode are *all* plotted as functions of the initial contact angle θ_0 for $0 \leq \theta_0 \leq \pi/2$, the latter for several values of the receding contact angle θ^*. In particular, figure 1.16 shows that for every value of

θ^* in the range $0 \leq \theta^* \leq \pi/2$, the lifetime of a droplet in the SS mode is equal to the lifetime of a droplet in the CA mode for $0 \leq \theta_0 \leq \theta^*$ and the lifetime of a droplet in the CR mode is shorter than the lifetime of a droplet in the SS mode, which is shorter than the lifetime of a droplet in the CA mode. In other words, at least for $0 \leq \theta_0 \leq \pi/2$, the curve corresponding to the lifetime of a droplet in the SS mode always lies *inside* the "limit lines" corresponding to lifetime of a droplet in the extreme modes (and not "outside the confined area between the two limit lines" as Nguyen and Nguyen [149] stated), and so the curve representing the lifetime of a droplet in the SS mode always lies *above* the curve representing the lifetime of a droplet in the CR mode and *below* the curve representing the lifetime of a droplet in the CA mode (and not "above the lifetime line of the single receding mode" as Nguyen and Nguyen [149] stated). However, it is important to note that figure 1.16 confirms the key conclusions of Nguyen and Nguyen [149] that "there are many "transition" lines for the combined mode" and that they have a qualitatively different shape from that tentatively suggested by Shanahan *et al.* [204].

In subsequent publications (Stauber *et al.* [223], Stauber *et al.* [225]) we gave a complete description of the lifetime of a droplet evaporating in the SS mode, and this work will be described in detail in Chapters 3 and 4.

Dash and Garimella [49, 50] investigated experimentally and theoretically the lifetimes of droplets evaporating on a (sometimes heated) hydrophobic and a (sometimes heated) superhydrophobic substrates. As mentioned previously, they found good agreement between the experimentally determined lifetimes of droplets evaporating on the hydrophobic substrate and the predicted lifetimes of droplets in the CA mode (see table 1.3), they found poor agreement between the experimentally determined lifetimes of droplets evaporating on the superhydrophobic substrate and the predicted lifetimes of droplets in the CA mode irrespective of the substrate temperature and proposed the extension for the simple version of the diffusion-limited model previously discussed in section 1.5.2. Note, however, that Dash and Garimella [49, 50] did not specify how the lifetimes were obtained in their experiments.

1.7 Overview of the Thesis

The main focus of this thesis is to investigate the evolution of sessile droplets in different modes of evaporation and, in particular, their lifetimes.

Before considering the SS and SJ modes, Chapter 2 briefly addresses the evaporation of droplets in the extreme modes. In particular, Chapter 2 describes the manner in which the extreme modes of evaporation become indistinguishable on strongly hydrophobic substrates. Simple asymptotic expressions are obtained which provide good approximations to the evolutions of the contact radius, the contact angle, and the volume of droplets evaporating in the extreme modes for a wide range of hydrophobic substrates.

Chapter 3 focuses on the lifetime of a droplet in the SS mode, and the unexpectedly subtle relationship between the lifetime of such a droplet and those of initially identical droplets evaporating in the extreme modes is described. In particular, it is shown that the lifetime of a droplet in the SS mode is not, in general, constrained by the lifetimes of a droplet in the extreme modes. Furthermore, good agreement is found between the predicted lifetimes and lifetimes determined from experiments reported in the literature.

In Chapter 4 we propose a simple relationship between the initial and receding contact angles based on the assumption of a constant maximum pinning force.

This relationship is then used to give a complete description of the lifetime of a droplet in the SS mode. In particular, it is shown that the dependence of the lifetime on the initial contact angle is qualitatively different from that in the case when the initial and receding angles are independent parameters, as studied in Chapter 3. Furthermore, both the proposed relationship and the theoretically predicted lifetimes calculated using it are found to agree surprisingly well with experimental results obtained by previous authors.

Chapters 5 and 6 focus on droplets evaporating in the SJ mode of evaporation. In particular, in Chapter 5 a simple model for the SJ mode is developed, and it is shown that in appropriate special cases the model for the SJ mode reduces to models for the CR, CA, and SS modes. Additionally, it is shown that the model for the SJ mode quantitatively predicts the experimental results obtained by previous authors.

In Chapter 6 the lifetime of a droplet in the SJ mode is considered. It is shown that the model derived in Chapter 5 predicts the experimentally determined lifetimes of droplets in the SJ mode obtained by previous authors surprisingly well, despite the fact that it predicts an infinite number of stick and jump phases. The rather complicated behaviour of the lifetime of a droplet in the SJ mode is analysed and it is demonstrated that under special conditions the lifetime of a droplet in the SJ mode can be approximated by the lifetime of a droplet in the CA mode.

In Chapter 7 some conclusions are drawn, and open questions and possible directions for further developments are discussed.

1.8 Publications and Presentations

Some aspects of the work in Chapter 1 have been published in Langmuir (Stauber *et al.* [220, 224]) and in the Proceedings of the 13th UK National Heat Transfer Conference, 2nd–3rd September 2013, London (Stauber *et al.* [221]).

The work in Chapter 2 has recently been published in Langmuir (Stauber *et al.* [224]).

The work in Chapter 3 has been published in the Journal of Fluid Mechanics (Stauber *et al.* [223]) and (as of 1st April 2015) has already been cited 14 times by other researchers [38, 72, 84, 121, 152, 156, 101, 130, 143, 208, 226, 247, 246, 256] . Furthermore, aspects of the work in Chapter 3 were also published as an extended abstract in the Proceedings of the 10th European Coating Symposium (ECS 13), 11th–13th September 2013, Mons, Belgium (Stauber *et al.* [222]). Various aspects of this work have been presented by me at the 55th British Applied Mathematics Colloquium at the University of Leeds in April 2013, the 26th Scottish Fluid Mechanics Meeting at the University of Aberdeen in May 2013, the 10th European Coating Symposium in Mons, Belgium in September 2013, a Continuum Mechanics and Industrial Mathematics Research Group Seminar within the Department of Mathematics and Statistics at the University of Strathclyde in December 2013, and the British Society of Rheology Midwinter Meeting at the University of Cambridge in December 2013.

The work in Chapter 4 has recently been submitted for publication (Stauber *et al.* [225]), and various aspects of this work have been presented by me at the 56th British Applied Mathematics Colloquium at Cardiff University in April 2014, the 27th Scottish Fluid Mechanics Meeting at the University of St. Andrews in May 2014, and the Institute of Physics (IoP) Science of Inkjet and Printed Drops Meeting in London in November 2014.

Furthermore, aspects of the work in Chapters 3 and 4 have been presented by my primary supervisor Prof. Stephen K. Wilson at the workshop on Drying Droplets at Durham University in March 2013, the 13th UK Heat Transfer Conference in London in September 2013, the IoP Science of Inkjet and Printed Drops Meeting in London in November 2013, the 66th APS Division of Fluid Dynamics Annual Meeting in Pittsburgh, USA in November 2013, the 1st International Conference on Micro and Nanofluidics in Twente, The Netherlands in May 2014, the 67th APS Division of Fluid Dynamics Annual Meeting in San Francisco, USA in November 2014, and the British Society of Rheology Midwinter Meeting at Durham University in December 2014. In addition, our collaborator Prof. Khellil Sefiane recently presented aspects of the work in Chapter 3 as part of an invited talk at the Smart and Green Interfaces Conference in Belgrade, Serbia in March 2015.

Aspects of the work in Chapters 5 and 6 are currently in preparation for publication, and will be presented by Prof. Stephen K. Wilson as part of an invited talk at Droplets 2015 to be held in Twente, The Netherlands in October 2015.

Chapter 2

Droplets in the Extreme Modes

As understanding the extreme modes of evaporation remains a key part of understanding the evaporation of droplets we shall first briefly consider the evaporation of droplets in the extreme modes before investigating the evaporation of droplets in the SS and SJ modes. In particular, the diffusion-limited model described in section 1.5.1 is used to discuss the evolution of droplets in the extreme modes in section 2.1 and to show how the extreme modes converge as the value of the initial contact angle θ_0 increases towards π, and so, in particular, to describe the manner in which they become indistinguishable on strongly hydrophobic substrates in section 2.2.

2.1 Evaporation of Droplets in the Extreme Modes

The evolution of the volume of the droplet V, the contact radius R and the contact angle θ as the droplet evaporates and hence, in particular, the lifetime of the droplet (*i.e.* the time it takes for R and/or θ and hence for V to reach zero), are determined by the rate of change of the volume of the droplet, $\mathrm{d}V/\mathrm{d}t$, given by equation (1.17).

As several previous authors have described, for a droplet evaporating in the CR mode, $R = R_0$ is constant, and so (1.17) becomes an equation for $\theta = \theta(t)$, namely

$$\frac{\mathrm{d}\theta}{\mathrm{d}t} = -\frac{D(c_{\mathrm{sat}} - c_\infty)}{\rho R_0^2} g(\theta) \tag{2.1}$$

which has the implicit solution

$$t = \frac{\rho R_0^2}{D(c_{\mathrm{sat}} - c_\infty)} \int_\theta^{\theta_0} \frac{\mathrm{d}\theta}{g(\theta)}, \tag{2.2}$$

while for a droplet evaporating in the CA mode, $\theta = \theta_0$ is constant, and so (1.17) becomes an equation for $R = R(t)$, namely

$$\frac{\mathrm{d}R}{\mathrm{d}t} = -\frac{D(c_{\mathrm{sat}} - c_\infty)}{\rho R} \frac{g(\theta_0)}{\sin\theta_0(2 + \cos\theta_0)} \tag{2.3}$$

which has the exact solution

$$R^2 = R_0^2 - \frac{2D(c_{\mathrm{sat}} - c_\infty)}{\rho} \frac{g(\theta_0)}{\sin\theta_0(2 + \cos\theta_0)} t \tag{2.4}$$

and hence

$$V = \frac{\pi}{3} \frac{\sin\theta_0(2 + \cos\theta_0)}{(1 + \cos\theta_0)^2} \left[R_0^2 - \frac{2D(c_{\mathrm{sat}} - c_\infty)}{\rho} \frac{g(\theta_0)}{\sin\theta_0(2 + \cos\theta_0)} t \right]^{3/2}. \tag{2.5}$$

A key observation is that in the special case $\theta_0 = \pi$ (*i.e.* for a perfectly hydrophobic substrate) *the CR and CA modes coincide at all times* t. In this case the free surface of the droplet is a complete sphere of radius $\mathcal{R} = \mathcal{R}(t)$ ($\mathcal{R} \geq 0$) touching the substrate at the single point $r = 0$ with constant contact radius $R \equiv R_0 = 0$ *and* constant contact angle $\theta \equiv \theta_0 = \pi$ *throughout its entire lifetime*, *i.e.* in this case (and only in this case) *the CR and CA modes are identical* *throughout their entire lifetimes.* For clarity it might be better to refer to them as a constant contact radius and constant contact angle mode in this special limit. Integrating the expression for the flux J in this special case given by (1.15) over the free surface of the droplet yields an equation for $\mathcal{R} = \mathcal{R}(t)$, namely

$$\frac{\mathrm{d}\mathcal{R}}{\mathrm{d}t} = -\log 2 \frac{D(c_{\mathrm{sat}} - c_\infty)}{\rho \mathcal{R}} \tag{2.6}$$

which has the exact solution

$$\mathcal{R}^2 = \mathcal{R}_0^2 - \log 2 \frac{2D(c_{\mathrm{sat}} - c_\infty)}{\rho} t, \tag{2.7}$$

where $\mathcal{R}_0 = \mathcal{R}(0)$ is the initial radius of the sphere, and hence

$$V = \frac{4\pi \mathcal{R}^3}{3} = \frac{4\pi}{3} \left[\mathcal{R}_0^2 - \log 2 \frac{2D(c_{\mathrm{sat}} - c_\infty)}{\rho} t \right]^{3/2}. \tag{2.8}$$

To simplify the subsequent presentation in this chapter it is convenient to scale time t with the maximum lifetime of a droplet evaporating in the CA mode (which occurs for $\theta_0 = \pi/2$), namely

$$\mathcal{T} = \frac{\rho}{2D(c_{\mathrm{sat}} - c_\infty)} \left(\frac{3V_0}{2\pi} \right)^{2/3} = \frac{\rho R_0^2}{2D(c_{\mathrm{sat}} - c_\infty)} \left(\frac{\sin\theta_0 (2 + \cos\theta_0)}{2(1 + \cos\theta_0)^2} \right)^{2/3}. \tag{2.9}$$

Setting $\theta = 0$ in (2.2) yields an expression for the scaled lifetime of a droplet evaporating in the CR mode, denoted by $t_{\mathrm{CR}} = t_{\mathrm{CR}}(\theta_0)$, namely

$$t_{\mathrm{CR}} = \left(\frac{2(1 + \cos\theta_0)^2}{\sin\theta_0 (2 + \cos\theta_0)} \right)^{2/3} \int_0^{\theta_0} \frac{2\,\mathrm{d}\theta}{g(\theta)}, \tag{2.10}$$

and setting $R = 0$ in (2.4) or $V = 0$ in (2.5) yields an expression for the scaled lifetime of a droplet evaporating in the CA mode, denoted by $t_{\mathrm{CA}} = t_{\mathrm{CA}}(\theta_0)$, namely

$$t_{\mathrm{CA}} = \left(\frac{2(1+\cos\theta_0)^2}{\sin\theta_0(2+\cos\theta_0)} \right)^{2/3} \frac{\sin\theta_0(2+\cos\theta_0)}{g(\theta_0)}. \tag{2.11}$$

Setting $\mathcal{R} = 0$ in (2.7) or $V = 0$ in (2.8) (or, equivalently, taking the limit $\theta_0 \to \pi^-$ in (2.10) or (2.11)) yields an expression for the scaled lifetime of both modes when $\theta_0 = \pi$, namely $t_{\mathrm{CA}} = t_{\mathrm{CR}} = t_\pi$, where

$$t_\pi = \frac{1}{4^{1/3}\log 2} \simeq 0.9088. \tag{2.12}$$

Figure 2.1 shows the evolutions of θ, $R/V_0^{1/3}$, and V/V_0 plotted as functions of $t/\mathcal{T}$ for droplets with different initial contact angles, namely $\theta_0 = \pi/18 = 10^\circ$, $\theta_0 = \pi/2 = 90^\circ$, $\theta_0 = \theta_{\mathrm{crit}} \simeq 2.5830 \simeq 148^\circ$, and $\theta_0 = 17\pi/18 = 170^\circ$, evaporating in the CR and CA modes. In particular, figure 2.1 shows that in the special case $\theta_0 = \theta_{\mathrm{crit}}$ (first identified approximately by Picknett and Bexon [160] to be approximately 140°, see section 1.6), the values of t_{CR} and t_{CA} coincide (specifically, $t_{\mathrm{CR}} = t_{\mathrm{CA}} = t_{\mathrm{crit}} \simeq 0.9354$), but the evolutions of R, θ and V for the two modes are very different. Note that this behaviour is qualitatively different from that when $\theta_0 = \pi$ described previously for which the two modes are identical for their entire lifetimes.

Figure 2.2(a) shows the scaled lifetimes of droplets evaporating in the CR mode, t_{CR}, given by (2.10), and in the CA mode, t_{CA}, given by (2.11), plotted as functions of the initial contact angle θ_0. In particular, figure 2.2(a) is qualitatively similar to figure 1.12 obtained by Picknett and Bexon [160] and Nguyen and Nguyen [148, Figure 5]. Just like figure 1.12 and figure 5 by Nguyen and Nguyen [148] it illustrates the sometimes overlooked fact that the lifetime of the CR mode is (slightly) longer than that of the CA mode when $\theta_{\mathrm{crit}} < \theta_0 < \pi$, and shows that both t_{CR} and t_{CA} approach t_π from above as $\theta_0 \to \pi^-$. Note, however, like figure 5

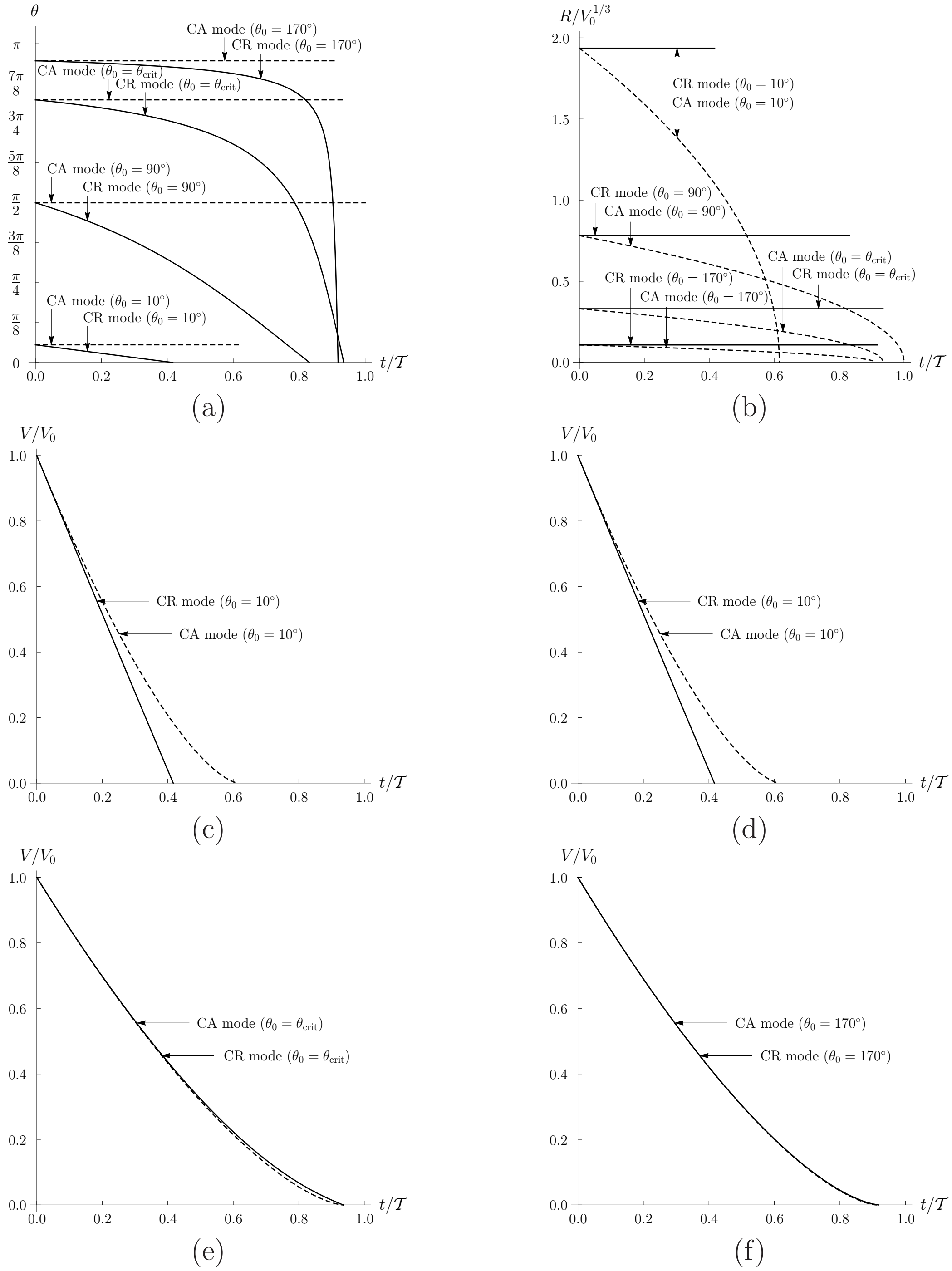

Figure 2.1: Evolutions of (a) the contact angle θ, (b) the scaled contact radius $R/V_0^{1/3}$, and (c)–(f) the scaled volume V/V_0, plotted as functions of scaled time $t/\mathcal{T}$ for droplets with different initial contact angles, namely $\theta_0 = \pi/18 = 10°$, $\theta_0 = \pi/2 = 90°$, $\theta_0 = \theta_{\text{crit}} \simeq 2.5830 \simeq 148°$, and $\theta_0 = 17\pi/18 = 170°$, evaporating in the CR and CA modes, shown by solid and dashed lines, respectively.

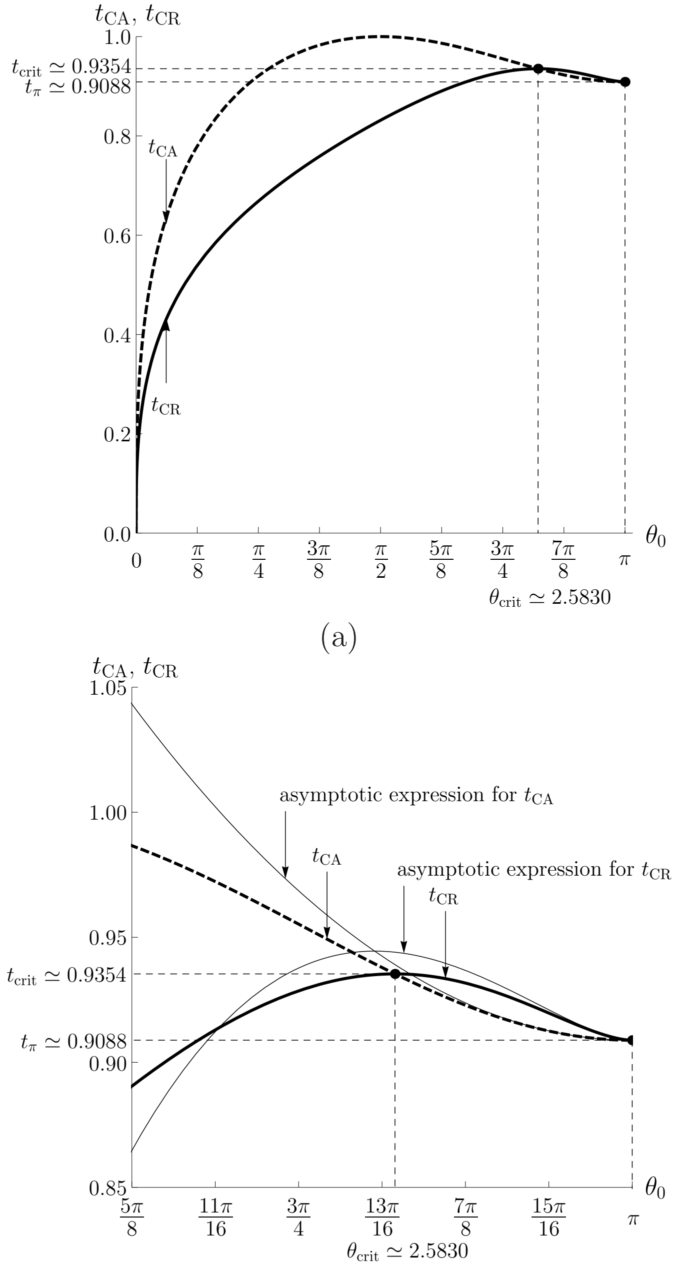

(b)

Figure 2.2: (a) Scaled lifetimes of droplets evaporating in the CR mode, t_{CR}, given by (2.10) and shown with a solid line, and in the CA mode, t_{CA}, given by (2.11) and shown with a dashed line, plotted as functions of the initial contact angle θ_0. (b) An enlargement of (a) near $\theta_0 = \pi$ also showing the asymptotic expressions for t_{CR} and t_{CA} in the limit $\theta_0 \to \pi^-$ given by (2.13) and (2.14), respectively.

by Nguyen and Nguyen [148], but unlike figure 1.12, figure 2.2(a) shows that the diffusion-limited model predicts the t_{CR} and t_{CA} curves coincide at the origin for $\theta_0 = 0$. Figure 2.2(a) shows the maximum value of $t_{\mathrm{CR}} = t_{\mathrm{crit}}$ occurs at $\theta_0 = \theta_{\mathrm{crit}}$, and the maximum value of $t_{\mathrm{CA}} = 1$ occurs at $\theta_0 = \pi/2$. In fact, analysis of the expressions for t_{CR} and t_{CA} given by (2.10) and (2.11), respectively, in the limit $\theta_0 \to \pi^-$ reveals that

$$t_{\mathrm{CR}} = t_\pi \left[1 - \frac{4\log 2 - 1}{12\log 2}(\pi - \theta_0)^2 \log(\pi - \theta_0)\right] + O\left(\pi - \theta_0\right)^2 \tag{2.13}$$

and

$$t_{\mathrm{CA}} = t_\pi \left[1 + \frac{4\log 2 - 1}{24\log 2}(\pi - \theta_0)^2\right] + O\left(\pi - \theta_0\right)^4, \tag{2.14}$$

and in the limit of small initial contact angle, $\theta_0 \to 0^+$, reveals that

$$t_{\mathrm{CR}} = \left(\frac{1}{3}\right)^{2/3} \frac{\pi}{2}\,\theta_0^{1/3} + O\left(\theta_0^{4/3}\right) \tag{2.15}$$

and

$$t_{\mathrm{CA}} = \left(\frac{1}{3}\right)^{2/3} \frac{3\pi}{4}\,\theta_0^{1/3} + O\left(\theta_0^{4/3}\right) \tag{2.16}$$

(and hence $t_{\mathrm{CA}} = 3t_{\mathrm{CR}}/2$ at leading order in this limit).

Figure 2.2(b) is an enlargement of Figure 2.2(a) near $\theta_0 = \pi$ also showing the asymptotic expressions (2.13) and (2.14), and illustrates that both asymptotic expressions, but particularly that for t_{CA}, provide good approximations to the exact values of t_{CR} and t_{CA} for a reasonably wide range of values of θ_0 near π.

2.2 The Convergence of the Extreme Modes on Strongly Hydrophobic Substrates

The evolutions of θ and $R/V_0^{1/3}$ plotted in Figures 2.1 (a) and (b) show that as the value of the initial contact angle θ_0 increases towards π both the value of the (varying) contact angle θ in the CR mode and the value of the (varying) contact radius R in the CA mode stay increasingly close to their initial values θ_0 and R_0, respectively. In other words, the extreme modes of droplet evaporation converge as the value of θ_0 increases towards π, and so, in particular, *the extreme modes become indistinguishable on strongly hydrophobic substrates.*

This behaviour might have been expected for the CA mode, for which $\theta \equiv \theta_0 \approx \pi$ necessarily remains close to π and R decreases by a small amount from its small initial value of $R_0 \approx 0$ to zero, and hence necessarily remains close to its value $R \equiv 0$ in the special case $\theta_0 = \pi$, during its evolution. Indeed, analysis of (2.3) or (2.4) reveals that for a droplet evaporating in the CA mode, the asymptotic expression for the contact radius R is given by

$$R = \left(\frac{3V_0}{4\pi}\right)^{1/3} \left(1 - \frac{t}{t_\pi}\right)^{1/2} (\pi - \theta_0) + O(\pi - \theta_0)^3 \tag{2.17}$$

in the limit $\theta_0 \to \pi^-$, which remains close to $R = 0$ for the entire lifetime of the droplet (*i.e.* until $t = t_\pi$ at leading order).

However, this behaviour is not so immediately obvious for the CR mode, for which $R \equiv R_0 \approx 0$ necessarily remains small but θ decreases by a non-small amount from its initial value of $\theta_0 \approx \pi$ to zero during its evolution. However, analysis of (2.1) reveals that for a droplet evaporating in the CR mode, the asymptotic expression for the contact angle θ is given by

$$\theta = \pi - \left(1 - \frac{t}{t_\pi}\right)^{-1/2} (\pi - \theta_0) + O(\pi - \theta_0)^3 \tag{2.18}$$

in the limit $\theta_0 \to \pi^-$, which indeed remains close to $\theta = \pi$ until near to the end of its lifetime (*i.e.* until near to $t = t_\pi$ at leading order).

Furthermore, as the evolution of V in the case $\theta_0 = 17\pi/18 = 170°$ shown in Figure 2.1(c) shows, V decreases from V_0 to zero in a very similar manner for both extreme modes, and indeed for this value of θ_0 they are virtually indistinguishable. Specifically, (2.17) and (2.18) reveal that, whichever mode the droplet is evaporating in, the asymptotic expression for the volume of the droplet V is given by

$$V = V_0 \left(1 - \frac{t}{t_\pi}\right)^{3/2} + O(\pi - \theta_0)^2 \tag{2.19}$$

in the limit $\theta_0 \to \pi^-$.

The increasing accuracy of the asymptotic expressions (2.17)–(2.19) as θ_0 increases towards π is illustrated in Figure 2.3, which shows the evolutions of θ and V/V_0 for a droplet evaporating in the CR mode, and the evolutions of $R/V_0^{1/3}$ and V/V_0 for a droplet evaporating in the CA mode, plotted as functions of $t/\mathcal{T}$ for droplets on hydrophobic substrates with different initial contact angles, namely $\theta_0 = 11\pi/18 = 110°$, $\theta_0 = 13\pi/18 = 130°$, $\theta_0 = 5\pi/6 = 150°$, and $\theta_0 = 17\pi/18 = 170°$, together with the corresponding asymptotic expressions in the limit $\theta_0 \to \pi^-$ given by (2.17)–(2.19). In particular, Figures 2.3 (a) and (c) show that the asymptotic expressions (2.18) and (2.17) provide good approximations to the evolutions of θ and R, respectively, when θ_0 is greater than about 150°, and Figures 2.3 (b) and (d) show that the asymptotic expression (2.19) provides a good approximation to the evolutions of V in *both* modes for all of the values of

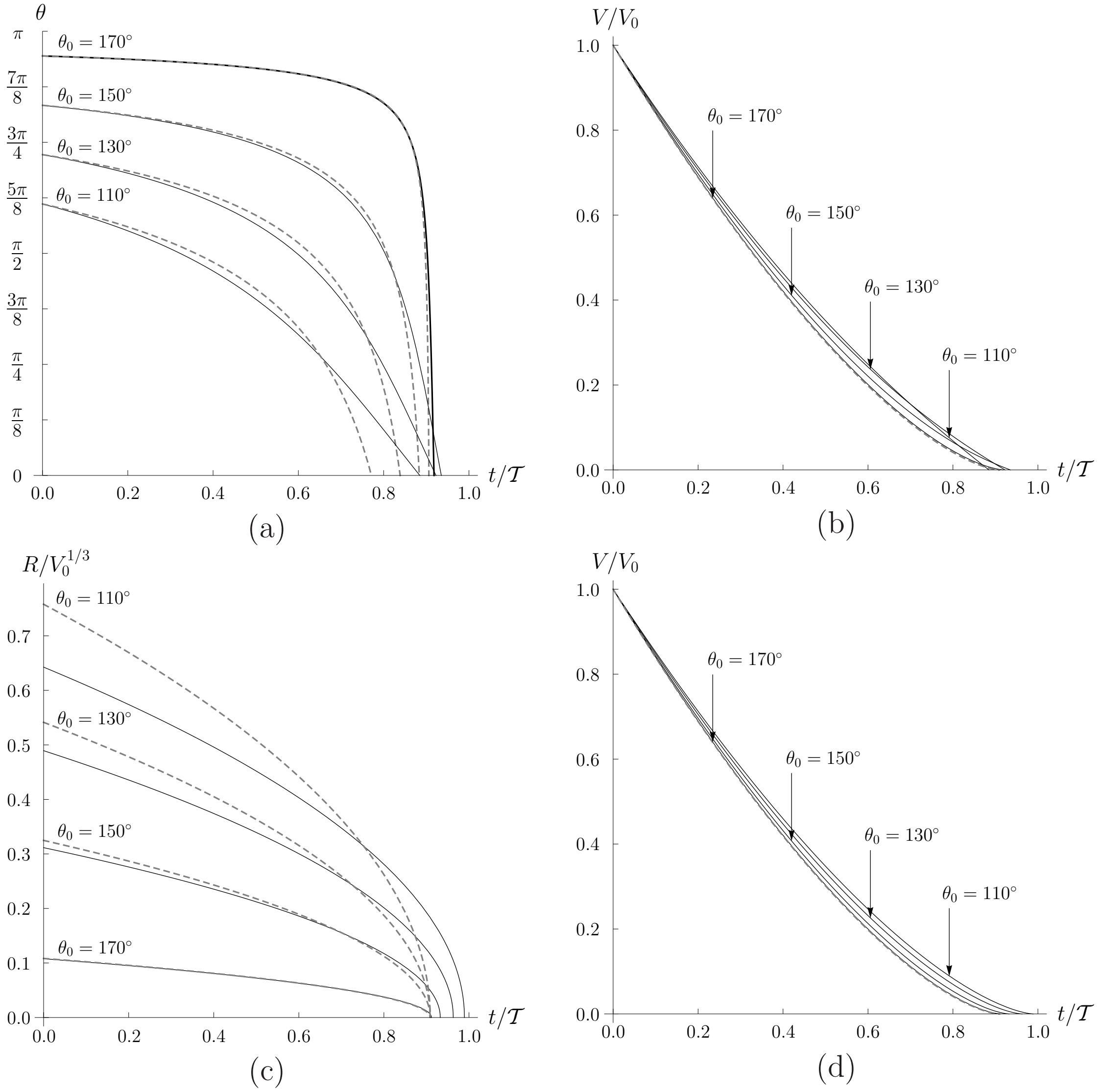

Figure 2.3: Evolutions of (a) the contact angle θ and (b) the scaled volume V/V_0 for a droplet evaporating in the CR mode, and evolutions of (c) the scaled contact radius $R/V_0^{1/3}$ and (d) the scaled volume V/V_0 for a droplet evaporating in the CA mode, plotted as functions of scaled time $t/\mathcal{T}$ for droplets on hydrophobic substrates with different initial contact angles, namely $\theta_0 = 11\pi/18 = 110°$, $\theta_0 = 13\pi/18 = 130°$, $\theta_0 = 5\pi/6 = 150°$, and $\theta_0 = 17\pi/18 = 170°$, together with the corresponding asymptotic expressions in the limit $\theta_0 \to \pi^-$ given by (2.17)–(2.19) shown with dashed lines.

θ_0 shown.

One important consequence of the convergence of the extreme modes is that using the exact solution for the evolution of V in the CA mode given by (2.5), which predicts the so-called "2/3 power law" that $(V/V_0)^{2/3}$ varies linearly with t, to extrapolate experimental data for V to estimate the lifetime of a droplet is also valid for the CR mode provided that θ_0 is sufficiently close to π. This conclusion is entirely consistent with the recent work of Nguyen and Nguyen [152], who found that evolution of V in the CR mode is well approximated by the 2/3 power law when θ_0 is sufficiently close to π.

2.3 Summary

In this chapter we have described the manner in which the extreme modes of droplet evaporation become indistinguishable on strongly hydrophobic substrates. In particular, we obtained simple asymptotic expressions (2.17)–(2.19) which provide good approximations to the evolutions of R, θ, and V, respectively, for a wide range of hydrophobic substrates. As a consequence, on strongly hydrophobic substrates it is appropriate to use the 2/3 power law to extrapolate the lifetimes of droplets evaporating in the CR mode as well as in the CA mode.

Thus having described the evolution of droplets in the extreme modes of evaporation we shall now give complete descriptions of the evolutions and the lifetimes of droplets evaporating in the SS mode and the SJ mode in the following chapters.

Chapter 3

Droplets in the Stick-Slide Mode

In this chapter a complete description of the lifetime of a droplet in the stick-slide (SS) mode is given. In section 3.1 we describe the evolution of a droplet in the SS mode. The predicted lifetimes of a droplet in the SS mode derived in section 3.2 are found to be in good agreement with lifetimes determined from experiments reported in the literature, as shown in section 3.3. Furthermore, the unexpectedly subtle relationship between the lifetime of a droplet in the SS mode and those of initially identical droplets evaporating in the extreme modes is described in section 3.4. In particular, it is shown that the lifetime of a droplet in the SS mode is not, in general, constrained by the lifetimes of a droplet in the extreme modes.

3.1 The Evolution of Droplets in the Stick-Slide Mode

We use the model for the SS mode mentioned in section 1.4.2 (as discussed by, for example, Nguyen and Nguyen [149], and Dash and Garimella [49]), which is sketched in figure 3.1. In this model initially the droplet evaporates in a CR phase

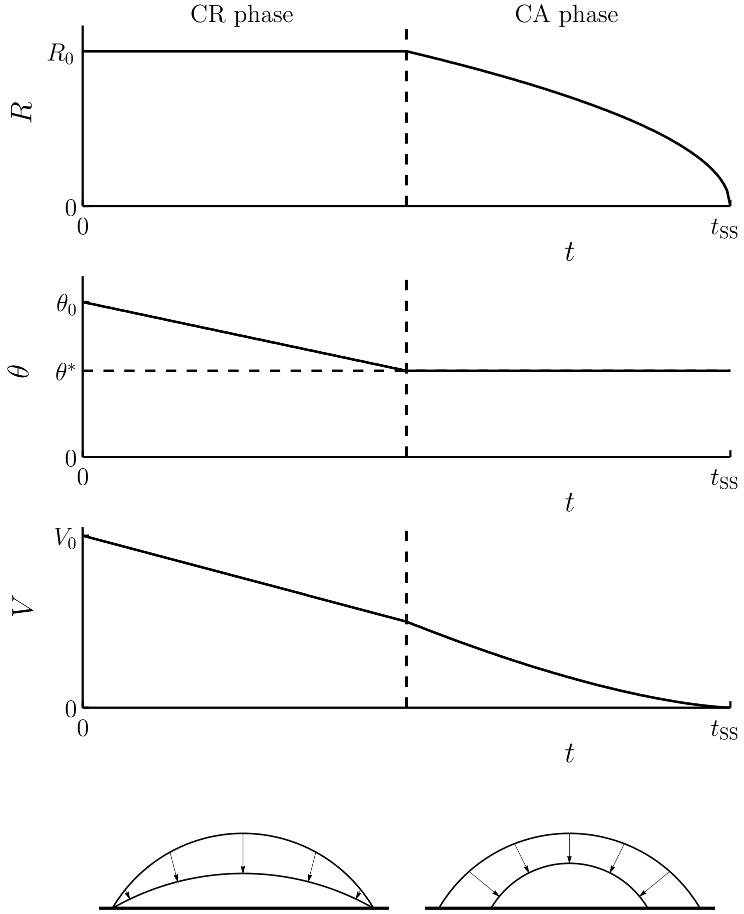

Figure 3.1: Sketch of the stick-slide (SS) mode studied in the present work in which initially the droplet evaporates in a CR phase in which $R = R_0$ and $\theta(t)$ and $V(t)$ decrease until $\theta(t)$ reaches the receding contact angle θ^* ($0 \leq \theta^* \leq \theta_0$), at which the contact line de-pins and subsequently the droplet evaporates in a CA phase in which $\theta(t) = \theta^*$ and $R(t)$ and $V(t)$ decrease to zero at time $t = t_{SS}$.

with $R = R_0$ and with $\theta = \theta(t)$ decreasing from $\theta = \theta_0$ ($0 \leq \theta_0 \leq \pi$) to the receding contact angle $\theta = \theta^*$ (referred to as the "transition contact angle" by [149]) ($0 \leq \theta^* \leq \pi$), after which the droplet evaporates in a CA phase with $\theta = \theta^*$ and with $R = R(t)$ decreasing from R_0 to zero. Note that we use θ^* instead of $\theta_{\rm rec}$ to be consistent with the notation by Nguyen and Nguyen [149]. The initial CR phase occurs only if $\theta_0 > \theta^*$; otherwise the contact line is always de-pinned and the droplet simply evaporates in the CA mode.

For a droplet evaporating in the SS mode, the droplet evaporates in a CR phase with $R = R_0$ constant and so (1.17) becomes an equation for $\theta = \theta(t)$ given by equation (2.1) and in a CA phase with $\theta = \theta^*$ constant and so (1.17) becomes an equation for $R = R(t)$, namely

$$\frac{\mathrm{d}R}{\mathrm{d}t} = -\frac{D(c_{\mathrm{sat}} - c_\infty)}{\rho R} \frac{g(\theta^*)}{\sin\theta^*(2 + \cos\theta^*)} \tag{3.1}$$

which has the exact solution

$$R^2 = R_0^2 - \frac{2D(c_{\mathrm{sat}} - c_\infty)}{\rho} \frac{g(\theta^*)}{\sin\theta^*(2 + \cos\theta^*)} \left(t - \frac{\rho R_0^2}{D(c_{\mathrm{sat}} - c_\infty)} \int_{\theta^*}^{\theta_0} \frac{\mathrm{d}\theta}{g(\theta)} \right), \tag{3.2}$$

and hence

$$\begin{aligned} V = \frac{\pi}{3} \frac{\sin\theta^*(2 + \cos\theta^*)}{(1 + \cos\theta^*)^2} \Bigg[& R_0^2 \\ & - \frac{2D(c_{\mathrm{sat}} - c_\infty)}{\rho} \frac{g(\theta^*)}{\sin\theta^*(2 + \cos\theta^*)} \left(t - \frac{\rho R_0^2}{D(c_{\mathrm{sat}} - c_\infty)} \int_{\theta^*}^{\theta_0} \frac{\mathrm{d}\theta}{g(\theta)} \right) \Bigg]^{3/2}. \end{aligned} \tag{3.3}$$

Like figure 2.1 figure 3.2 shows the evolutions of θ, $R/V_0^{1/3}$, and V/V_0 plotted as functions of $t/\mathcal{T}$ for droplets with different initial contact angles, namely $\theta_0 = \pi/18 = 10°$, $\theta_0 = \pi/2 = 90°$, and $\theta_0 = 17\pi/18 = 170°$, evaporating in the extreme modes. However, unlike figure 2.1, figure 3.2 does not show the evolutions for droplets with initial contact angles $\theta_0 = \theta_{\mathrm{crit}} \simeq 2.5830 \simeq 148°$ evaporating in the extreme modes, but instead it shows shows the evolutions of θ, $R/V_0^{1/3}$, and V/V_0 plotted as functions of $t/\mathcal{T}$ for initially identical droplets evaporating in the SS mode with $\theta_0 = \pi/18$ and $\theta^* = 0$, $\theta_0 = \pi/2$ and $\theta^* = 1.3694 \approx 78°$, and $\theta_0 = 17\pi/18$ and $\theta^* = 2.4732 \approx 142°$. Note, figure 3.2 shows in the case of the droplet evaporating in the SS mode with $\theta_0 = \pi/18$ and $\theta^* = 0$ the contact line never de-pins, and, therefore, the evolutions of θ, $R/V_0^{1/3}$, and V/V_0 are identical to the evolutions of a droplet in the CR mode. However, figure 3.2 also shows in the

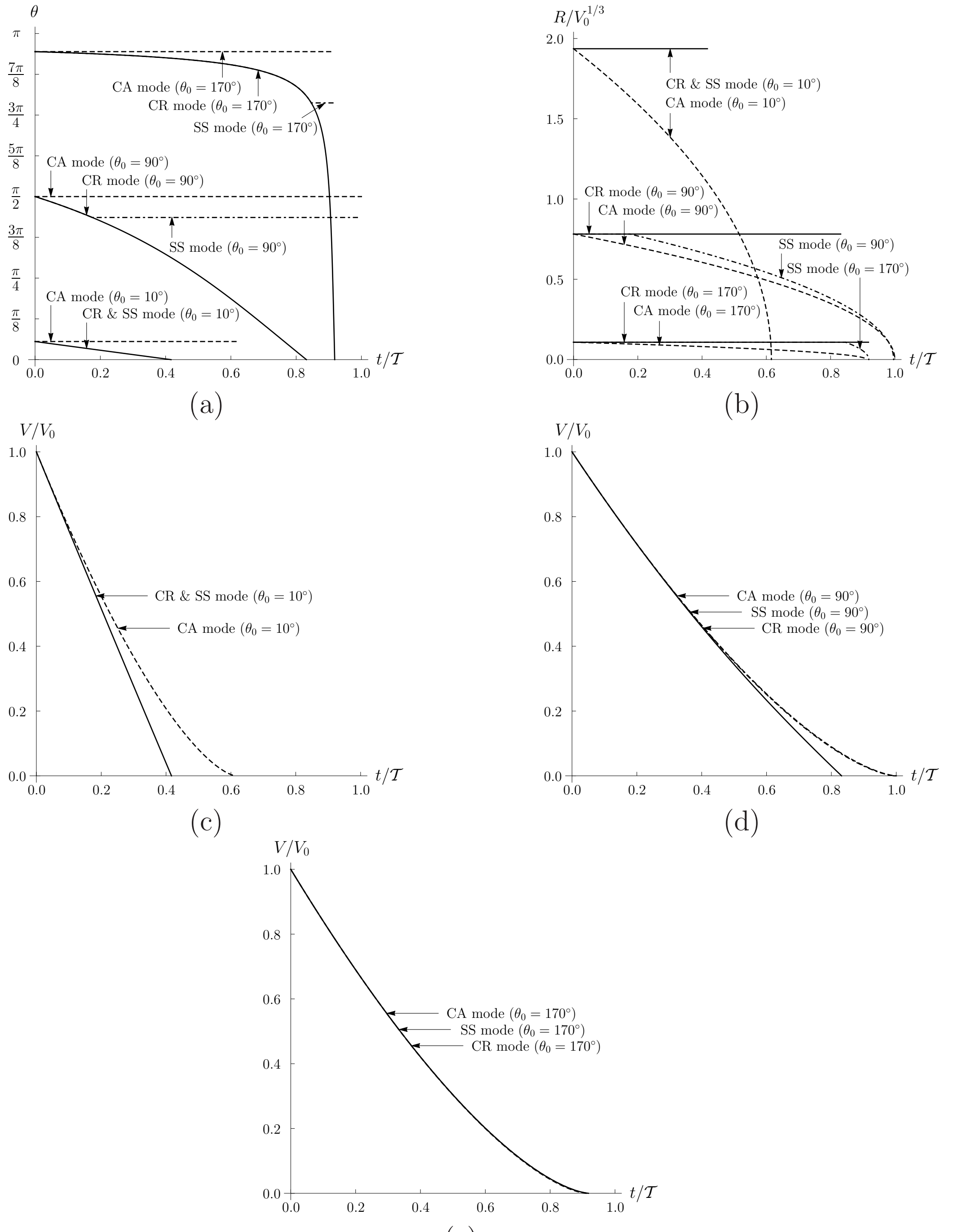

(a) (b)

(c) (d)

(e)

Figure 3.2: Evolutions of (a) the contact angle θ, (b) the scaled contact radius $R/V_0^{1/3}$, and (c)–(e) the scaled volume V/V_0, plotted as functions of scaled time $t/\mathcal{T}$ for droplets with different initial contact angles, namely $\theta_0 = \pi/18 = 10^\circ$, $\theta_0 = \pi/2 = 90^\circ$, and $\theta_0 = 17\pi/18 = 170^\circ$, evaporating in the CR, CA, and SS modes, the latter with $\theta^* = 0$, $\theta^* = 1.3694 \approx 78^\circ$, and $\theta^* = 2.4732 \approx 142^\circ$, respectively, shown by solid, dashed, and dot-dashed lines, respectively.

cases of the droplets evaporating in the SS modes with $\theta_0 = \pi/2$ and $\theta^* = 1.3694$, and $\theta_0 = 17\pi/18$ and $\theta^* = 2.4732$ the evolutions of θ, $R/V_0^{1/3}$, and V/V_0 are only identical to the evolutions of an initially identical droplet in the CR mode, while the droplet evaporates in the CR phase, *i.e.* until $\theta = \theta^*$. Note, for the droplet evaporating in the SS mode with $\theta_0 = \pi/2 = 90°$ and $\theta^* = 1.3694 \approx 78°$, it is in the CA phase for most of its lifetime, whereas for the droplet in the SS mode with $\theta_0 = 17\pi/18$ and $\theta^* = 2.4732$ it is in the CR phase for most of its lifetime. In the previous chapter it was shown that on strongly hydrophobic substrates the extreme modes become indistinguishable; figure 3.2 shows that the extreme modes and the SS mode become indistinguishable for strongly hydrophobic substrates.

Thus having described the evolution of a droplet in the SS mode, we can determine the lifetime of a droplet, which as we have seen in the previous section, is the time it takes for R and/or θ and hence for V to reach zero.

3.2 Theoretical Predictions for the Lifetimes of Droplets in the Stick-Slide Mode

Just as in the previous chapter we scale time t with the maximum lifetime of a droplet evaporating in the CA mode (which occurs for $\theta_0 = \pi/2$), namely $\mathcal{T}$ given in equation (2.9), for the remainder of this chapter. Thus as described in the previous chapter, the lifetime of a droplet evaporating in the CR mode, denoted by $t_{\mathrm{CR}} = t_{\mathrm{CR}}(\theta_0)$, is given by (2.10) and the lifetime of a droplet evaporating in the CA mode, denoted by $t_{\mathrm{CA}} = t_{\mathrm{CA}}(\theta_0)$, is given by (2.11).

The lifetime of a droplet evaporating in the SS mode is denoted by $t_{\mathrm{SS}} = t_{\mathrm{SS}}(\theta_0, \theta^*)$, and unlike t_{CR} and t_{CA}, is, in general, a function of the receding contact angle θ^* as well as of the initial contact angle θ_0, and will not, in general, be equal to either t_{CR} or t_{CA} when $\theta_0 > \theta^*$. Specifically, for $0 \le \theta_0 \le \theta^*$ the droplet simply evaporates in the CA mode, and hence we have $t_{\mathrm{SS}} = t_{\mathrm{CA}}$, where t_{CA} is given by (2.11), but for $\theta_0 \ge \theta^*$ initially the droplet evaporates in a CR phase until θ reaches θ^* after which it evaporates in a CA phase until R reaches zero, and hence we have

$$t_{\mathrm{SS}} = \left(\frac{2(1+\cos\theta_0)^2}{\sin\theta_0(2+\cos\theta_0)}\right)^{2/3} \left[\int_{\theta^*}^{\theta_0} \frac{2\,\mathrm{d}\theta}{g(\theta)} + \frac{\sin\theta^*(2+\cos\theta^*)}{g(\theta^*)}\right], \qquad (3.4)$$

where the first term on the right-hand side of (3.4) represents the duration of the CR phase and the second term represents the duration of the CA phase.

3.3 Experimental Validation of the Model

Before analysing the theoretically predicted lifetime of an evaporating droplet, t_{SS}, given by (3.4), the model is verified by comparison with the results of relevant physical experiments in the literature for which all of the necessary data are available. In particular, we use the 29 sets of experimental results for droplets evaporating in a SS mode obtained by Bourgès-Monnier and Shanahan [26], Uno *et al.* [235], Fukai *et al.* [76], Li *et al.* [126], Song *et al.* [218], Nguyen *et al.* [147], Lim *et al.* [128], Yu *et al.* [249], and Dash and Garimella [49] for which the duration of the second slide phase was at most 10% of the lifetime of the droplet, so that the present idealised SS mode is likely to be an appropriate description of their behaviour. An example of one of these 29 sets, whose details are given in table 3.1, is given in figure 3.3. In particular, figure 3.3 shows the evolution of a water droplet evaporating on silicon coated with a 3-mercaptopropyltrimethoxysilane monolayer in the SS mode, as observed by Fukai *et al.* [76, Figure 3]. In particular, figure 3.3 shows the droplet initially evaporates in a CR phase in which R is approxi-

Reference	Figure	Fluid	Substrate
Bourgès-Monnier and Shanahan [26]	Fig. 1 (stages II–IV)	Water	Polished epoxy resin
	Fig. 2 (stages II–IV)	Water	Polished epoxy resin
Uno *et al.* [235]	Fig. 3(d)	Latex dispersion	ODTES_{100} on glass
Fukai *et al.* [76]	Fig. 3	Water	SO_3H on silicon
	Fig. 4	Water	SO_3H on silicon
	Fig. 5	Xylene	R_f on silicon
Li *et al.* [126]	Fig. 5 (all 9 sets)	Water	Dialkyl disulfides on gold-covered mica
Song *et al.* [218]	Fig. 2	Water	Platinum
Nguyen *et al.* [147]	Fig. 5 (all 4 sets)	Water	Oct-silicon
	Fig. 9(a)	Water	Oct-silicon
	Fig. 9(b)	Water	OTS-silicon
	Fig. 9(c)	Water	Teflon
Lim *et al.* [128]	Fig. 4(c)	Water	Pyrex glass
	Fig. 6(b)	Diethylene glycol with coffee particles	Pyrex glass
Yu *et al.* [249]	Figs 2 and 4 (2 μl droplet)	Water	Teflon on PDMS on glass
Dash and Garimella [49]	Fig. 3 and Table 3 (all 3 sets)	Water	Teflon on silicon

Table 3.1: Details of the 29 sets of experimental results used in this chapter. In the “Substrate” column, “ODTES_{100}” denotes octadecyltriethoxysilane with a static contact angle of roughly 100° for pure water, “SO_3H” denotes 3-mercaptopropyltrimethoxysilane, “R_f” denotes perfluorohexylethyltrimethoxysilane, “Oct-silicon” denotes silicon hydrophobised with octanol, “OTS-silicon” denotes silicon hydrophobised with n-octadecyltrichlorosilane in heptane, and “PDMS” denotes polydimethylsiloxane.

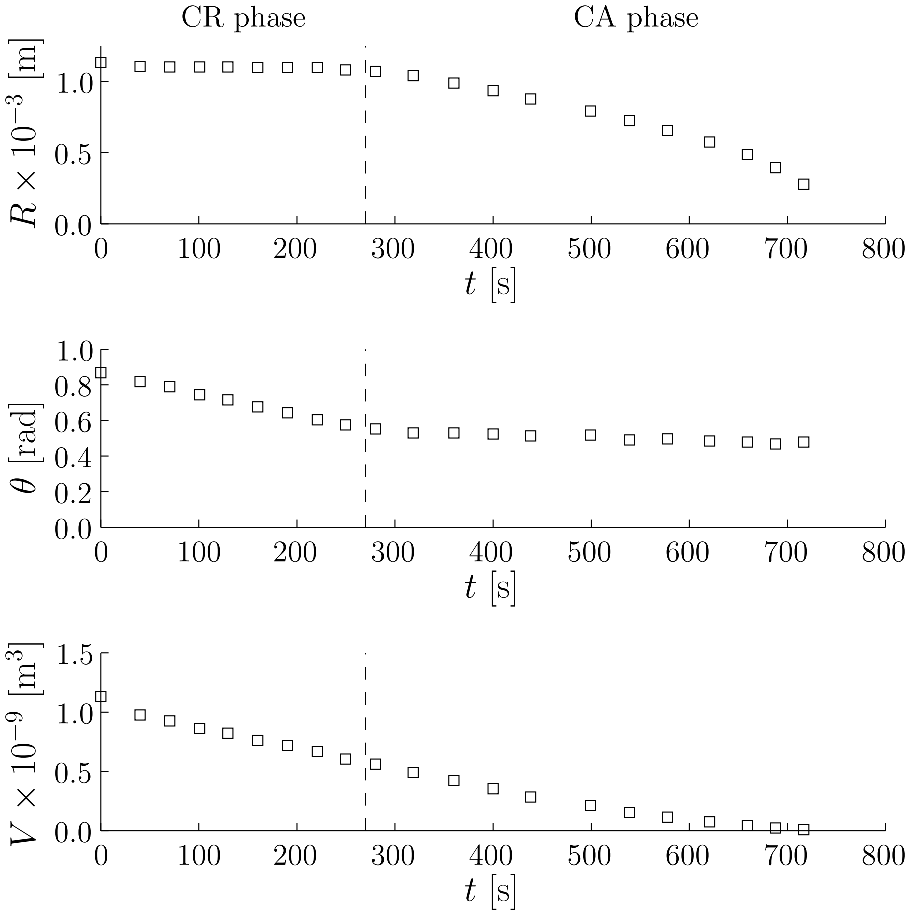

Figure 3.3: Experimental data for the evolution of R, θ, and V of a water droplet evaporating in the SS mode on silicon coated with a 3-mercaptopropyltrimethoxysilane monolayer observed by Fukai *et al.* [76, Figure 3]. In particular, the droplet initially evaporates in a CR phase in which R is approximately constant and θ and V decrease until $\theta = \theta^* \approx 0.56 \simeq 32^\circ$ and thereafter it evaporates in a CA phase in which θ is approximately constant and R and V decrease. Note that the interpolated time at which $\theta = \theta^*$ is denoted by a dashed line and that the second slide phase is negligible for this set of experimental results.

mately constant and θ and V decrease until $\theta = \theta^* \approx 0.56 \simeq 32^\circ$ and thereafter it evaporates in a CA phase in which θ is approximately constant and R and V decrease.

For each of these sets of experimental results the experimentally determined lifetime of the droplet, denoted by t_{exp}, was obtained by fitting the experimental

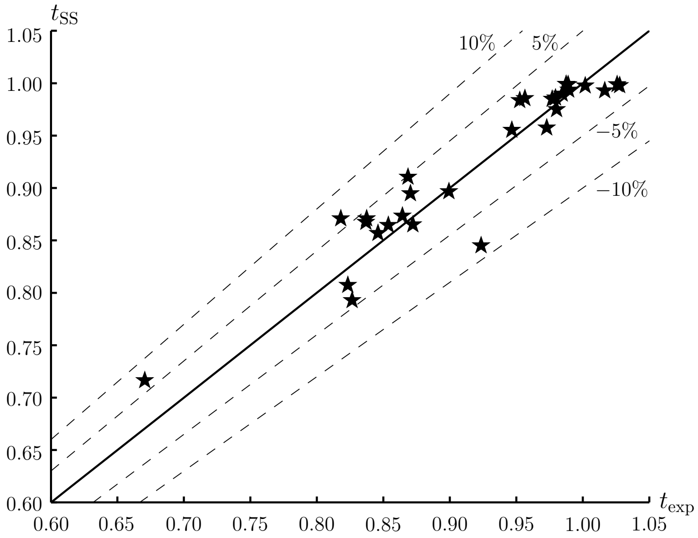

Figure 3.4: The theoretically predicted lifetimes of evaporating droplets, t_{SS}, calculated numerically from (3.4) using the experimentally determined values of θ_0 and θ^* plotted as a function of the corresponding experimentally determined values, t_{exp}, together with a solid line showing $t_{\mathrm{SS}} = t_{\mathrm{exp}}$ and dashed lines showing 5% and 10% deviations from $t_{\mathrm{SS}} = t_{\mathrm{exp}}$.

data for $V^{2/3}$ as a linear function of t and extrapolating to $V = 0$ (which is, of course, exact only for the CA mode as shown in the previous chapter) as proposed by, for example, Nguyen *et al.* [147] and Nguyen and Nguyen [148], see section 1.6. Figure 3.4 shows t_{SS} calculated numerically from (3.4) using the experimentally determined values of θ_0 and θ^* plotted as a function of the corresponding values of t_{exp} together with a solid line showing $t_{\mathrm{SS}} = t_{\mathrm{exp}}$ and dashed lines showing 5% and 10% deviations from $t_{\mathrm{SS}} = t_{\mathrm{exp}}$. In particular, figure 3.4 shows that the theoretically predicted values are in excellent agreement with the experimentally determined values, with all of the values of t_{SS} lying within 10% of t_{exp} and 26 of the 29 values lying within 5%.

3.4 The Lifetimes of Evaporating Droplets

Figures 3.5 and 3.6 show the lifetime of a droplet evaporating in the SS mode, t_{SS}, given by (3.4), together with the lifetimes of initially identical droplets evaporating in the CR and CA modes, t_{CR} and t_{CA}, given by (2.10) and (2.11), plotted as functions of θ_0 for various values of θ^* in the ranges $0 < \theta^* \leq \pi/2$ and $\pi/2 \leq \theta^* < \pi$, respectively. Figures 3.5 and 3.6 show that $t_{\mathrm{CR}} = t_{\mathrm{CA}} = t_{\mathrm{SS}} = 0$ at $\theta_0 = 0$, and that for strongly hydrophobic substrates all three modes considered in the present chapter become indistinguishable, as $t_{\mathrm{CR}} = t_{\mathrm{CA}} = t_{\mathrm{SS}} = t_\pi = (4^{1/3} \log 2)^{-1} \simeq 0.9088$ at $\theta_0 = \pi$. As we have seen in section 2.1 the maximum value of $t_{\mathrm{CR}} = t_{\mathrm{crit}}$ occurs at $\theta_0 = \theta_{\mathrm{crit}}$, and the maximum value of $t_{\mathrm{CA}} = 1$ occurs at $\theta_0 = \pi/2$. The maximum value of t_{SS} depends on the value of θ^*: when $0 \leq \theta^* \leq \pi/2$ it occurs at $\theta_0 = \hat{\theta}_0$, where $\hat{\theta}_0 = \hat{\theta}_0(\theta^*)$ is the unique value of θ_0 in the range $\pi/2 \leq \theta_0 \leq \theta_{\mathrm{crit}}$ at which $t_{\mathrm{SS}} = t_{\mathrm{CA}}$ indicated with solid dots in figure 3.5(b), but when $\pi/2 \leq \theta^* \leq \pi$ it always occurs at $\theta_0 = \pi/2$ at which $t_{\mathrm{SS}} = t_{\mathrm{CA}} = 1$.

Since the SS mode is a simple combination of the extreme modes one might assume, as some previous authors (such as, for example, Nguyen and Nguyen [149]) have done, that the lifetime of a droplet evaporating in this mode is always constrained by the lifetimes of initially identical droplets evaporating in the extreme modes. However, while figures 3.5 and 3.6 show that when $0 < \theta_0 \leq \pi/2$ shown previously in figure 1.16 (and, in particular, in the thin-film limit $\theta_0 \to 0^+$) it is indeed correct that t_{SS} lies between t_{CR} and t_{CA}, they also show that when $\pi/2 < \theta_0 < \pi$ not shown previously in figure 1.16 this result is not, in general, correct. Specifically, figures 3.5 and 3.6 show that $t_{\mathrm{SS}} > \max(t_{\mathrm{CR}}, t_{\mathrm{CA}})$ when θ_0 lies in the range $\hat{\theta}_0 < \theta_0 < \pi$ in the case $0 < \theta^* \leq \pi/2$ and when θ_0 lies in the range $\theta^* < \theta_0 < \pi$ in the case $\pi/2 \leq \theta^* < \theta_{\mathrm{crit}}$. In other words, when $0 < \theta^* < \theta_{\mathrm{crit}}$ (but not otherwise) the lifetime of a droplet evaporating in the SS mode is longer

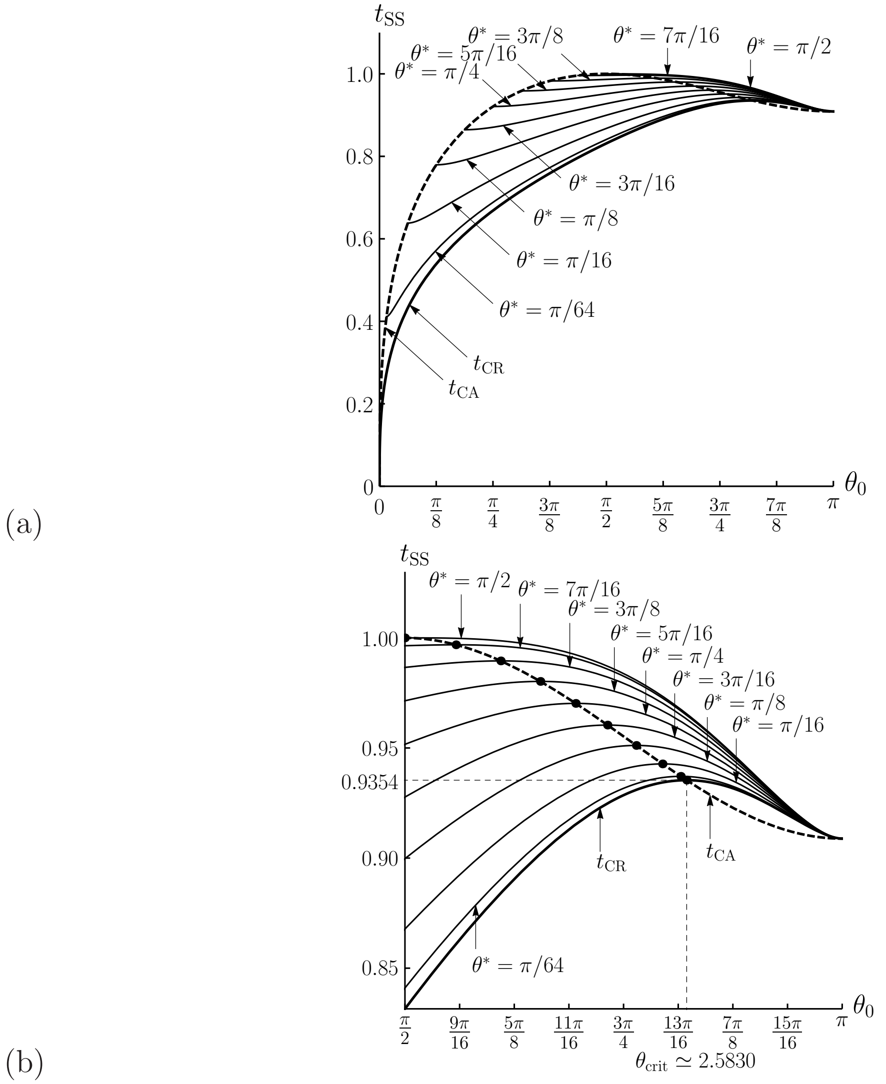

Figure 3.5: The lifetime of a droplet evaporating in the SS mode, t_{SS}, given by (3.4), plotted as a function of the initial contact angle θ_0 for various receding contact angles in the range $0 < \theta^* \leq \pi/2$, namely $\theta^* = \pi/64$, $\pi/16$, $\pi/8$, $3\pi/16$, $\pi/4$, $5\pi/16$, $3\pi/8$, $7\pi/16$, $\pi/2$, together with the lifetimes of initially identical droplets evaporating in the CR and CA modes, t_{CR} and t_{CA}, given by (2.10) and (2.11), respectively. in which the values of $\theta_0 = \hat{\theta}_0$ at which the maximum value of t_{SS} occurs are indicated with solid dots.

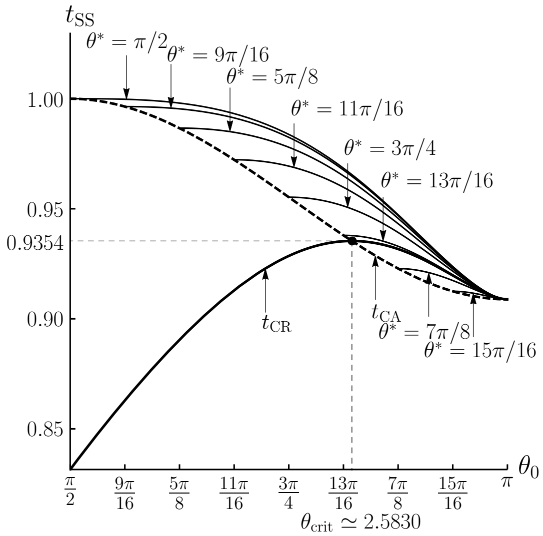

Figure 3.6: As figure 3.5, except for various receding contact angles in the range $\pi/2 \leq \theta^* < \pi$, namely $\theta^* = \pi/2$, $9\pi/16$, $5\pi/8$, $11\pi/16$, $3\pi/4$, $13\pi/16\,(< \theta_{\mathrm{crit}} \simeq 2.5830)$, $7\pi/8\,(> \theta_{\mathrm{crit}})$, $15\pi/16$. For clarity, only the behaviour in the range $\pi/2 \leq \theta_0 \leq \pi$ is shown.

than those of initially identical droplets evaporating in the extreme modes for sufficiently large values of θ_0. Furthermore, figures 3.5 and 3.6 also show that, for any value of θ^*, $t_{\mathrm{CR}}, t_{\mathrm{CA}}, t_{\mathrm{SS}} \leq t_{\mathrm{CA}}(\pi/2) = 1$, *i.e.* the longest lifetime of any droplet evaporating in any of the three modes for all possible values of θ_0 and θ^* is that of a droplet with initial contact angle $\theta_0 = \pi/2$ evaporating in the CA mode. Note that the behaviour of the curves corresponding to t_{SS} is qualitatively different from that tentatively suggested by Shanahan *et al.* [204] (see figure 1.14). Details of the behaviour of t_{CR}, t_{CA} and t_{SS} in appropriate asymptotic limits are given in the next subsection.

3.4.1 Asymptotic Behaviour of t_{SS}

As figures 3.5 and 3.6 show, for all values of θ^* the curves corresponding to t_{SS} depart from the curve corresponding to t_{CA} at $\theta_0 = \theta^*$ with zero slope according to

$$t_{\mathrm{SS}} = t_{\mathrm{CA}}(\theta^*) + A(\theta^*)(\theta_0 - \theta^*)^2 + O\left(\theta_0 - \theta^*\right)^3, \tag{3.5}$$

in the limit $\theta_0 \rightarrow \theta^{*+}$, where the coefficient $A = A(\theta^*)$ is given by

$$\begin{aligned} A(\theta^*) &= \left(\frac{2(1+\cos\theta^*)^2}{\sin\theta^*(2+\cos\theta^*)}\right)^{2/3} \\ &\times \frac{(2\cos^2\theta^* + 2\cos\theta^* - 3)g(\theta^*) - \sin\theta^*(2+\cos\theta^*)g'(\theta^*)}{\sin\theta^*(2+\cos\theta^*)g(\theta^*)^2}, \end{aligned} \tag{3.6}$$

where a dash ($'$) denotes differentiation with respect to argument. In particular, since $A > 0$ for $0 < \theta^* < \pi/2$ but $A < 0$ for $\pi/2 < \theta^* < \pi$, the curves corresponding to t_{SS} have a local minimum at $\theta_0 = \theta^*$ for $0 < \theta^* < \pi/2$ as shown in figure 3.5(a), but a local maximum at $\theta_0 = \theta^*$ for $\pi/2 < \theta^* < \pi$ as shown in figure 3.6. Furthermore, in the limit of large initial contact angle, $\theta_0 \rightarrow \pi^-$, the curves corresponding to t_{SS} approach the value t_π given in equation (2.12) with zero slope according to (2.13) to the order of accuracy shown.

As figure 3.5 shows, in the limit of small receding contact angle, $\theta^* \rightarrow 0^+$, the curves corresponding to t_{SS} approach the curve corresponding to t_{CR} from above for all values of θ_0 according to

$$t_{\mathrm{SS}} = t_{\mathrm{CR}}(\theta_0) + \left(\frac{2(1+\cos\theta_0)^2}{\sin\theta_0(2+\cos\theta_0)}\right)^{2/3}\frac{\pi}{16}\theta^* + O\left(\theta^{*2}\right). \tag{3.7}$$

As figure 3.6 shows, in the limit of large receding contact angle, $\theta^* \rightarrow \pi^-$, the curves corresponding to t_{SS} approach the curve corresponding to t_{CA} from above for all values of θ_0 in the vanishingly small range $\theta^* < \theta_0 < \pi$ according to

$$t_{\mathrm{SS}} = t_\pi\left[1 + \frac{4\log 2 - 1}{24\log 2}(\pi - \theta_0)^2\left\{1 - 2\log\left(\frac{\pi - \theta_0}{\pi - \theta^*}\right)\right\}\right] + O\left(\pi - \theta_0\right)^4. \tag{3.8}$$

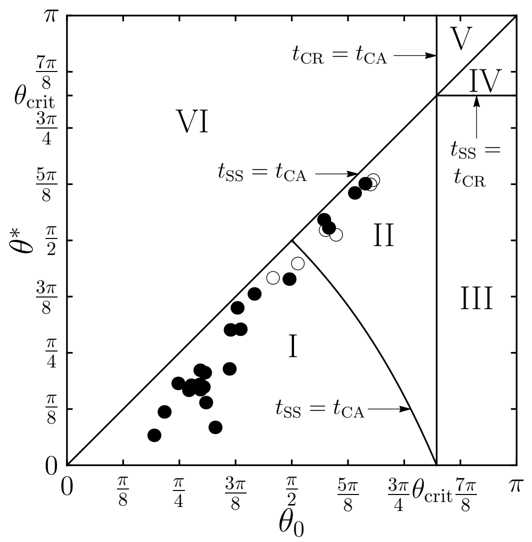

Figure 3.7: Master diagram showing how the θ_0–θ^* parameter plane is divided up into regions in which the six possible orderings of the lifetimes of initially identical droplets evaporating in the CR, CA and SS modes occur. Region I corresponds to $t_{\mathrm{CR}} < t_{\mathrm{SS}} < t_{\mathrm{CA}}$, region II to $t_{\mathrm{CR}} < t_{\mathrm{CA}} < t_{\mathrm{SS}}$, region III to $t_{\mathrm{CA}} < t_{\mathrm{CR}} < t_{\mathrm{SS}}$, region IV to $t_{\mathrm{CA}} < t_{\mathrm{SS}} < t_{\mathrm{CR}}$, region V to $t_{\mathrm{SS}} = t_{\mathrm{CA}} < t_{\mathrm{CR}}$, and region VI to $t_{\mathrm{CR}} < t_{\mathrm{SS}} = t_{\mathrm{CA}}$. In particular, note that $t_{\mathrm{SS}} > \max(t_{\mathrm{CR}}, t_{\mathrm{CA}})$ in regions II and III. For each set of experimental results the appropriate point is denoted by a solid circle if the experimentally determined lifetime of the droplet, t_{exp}, is correctly ordered with respect to the theoretically predicted values of t_{CR} and t_{CA}, and by an open circle if it is not.

3.4.2 Master Diagram

The relationship between the lifetimes of initially identical droplets evaporating in the three different modes is summarised in the master diagram presented in figure 3.7, which shows how the θ_0–θ^* parameter plane is divided up into regions in which the six possible orderings of t_{CR}, t_{CA} and t_{SS} occur. Specifically, in figure 3.7 region I corresponds to $t_{\mathrm{CR}} < t_{\mathrm{SS}} < t_{\mathrm{CA}}$, region II to $t_{\mathrm{CR}} < t_{\mathrm{CA}} < t_{\mathrm{SS}}$, region III to $t_{\mathrm{CA}} < t_{\mathrm{CR}} < t_{\mathrm{SS}}$, region IV to $t_{\mathrm{CA}} < t_{\mathrm{SS}} < t_{\mathrm{CR}}$, region V to $t_{\mathrm{SS}} = t_{\mathrm{CA}} < t_{\mathrm{CR}}$, and region VI to $t_{\mathrm{CR}} < t_{\mathrm{SS}} = t_{\mathrm{CA}}$. In particular, figure 3.7 shows that these are the only possible orderings that can occur. For example, there are no parameter values for which $t_{\mathrm{SS}} < \min(t_{\mathrm{CR}}, t_{\mathrm{CA}})$, *i.e.* the lifetime of a droplet evaporating in the

SS mode can never be less than both of the lifetimes of initially identical droplets evaporating in the extreme modes. The upper left-hand half of the parameter plane (*i.e.* regions V and VI), $\theta_0 > \theta^*$, corresponds to situations in which the SS and CA modes coincide, and so, in particular, the behaviour in it is independent of θ^*. The most interesting behaviour occurs in the lower right-hand half of the parameter plane (*i.e.* regions I–IV), $\theta_0 < \theta^*$, in which the SS mode has both a CR and a CA phase. In particular, approximately 53% of it is occupied by regions II and III in which $t_{\mathrm{SS}} > \max(t_{\mathrm{CR}}, t_{\mathrm{CA}})$, *i.e.* in which the lifetime of a droplet evaporating in the SS mode is longer than the lifetimes of initially identical droplets evaporating in the extreme modes.

Figure 3.7 also includes points corresponding to the 29 sets of experimental results shown previously in figure 3.4. Note that since all of these sets of experimental results include the initial CR phase they all have $\theta_0 > \theta^*$, and hence all of the points lie in the lower right-hand half of the parameter plane. In particular, for each set of experimental results the appropriate point in the θ_0–θ^* parameter plane is denoted by a solid circle if the experimentally determined lifetime of the droplet, t_{exp}, is correctly ordered with respect to the theoretically predicted values of t_{CR} and t_{CA}, and by an open circle if it is not. As figure 3.7 shows, all of the points are in regions I and II, and 23 of the 29 sets of experimental results are correctly ordered, providing encouraging support for the present model. However, note that, since all of the sets of experimental results shown correspond to values of θ_0 satisfying $\theta_0 < \theta_{\mathrm{crit}}$, there are no points in regions III and IV, and so testing the present model for superhydrophobic droplets with $\theta_0 > \theta_{\mathrm{crit}}$ remains an open challenge.

3.5 Summary

In the present chapter we obtained a complete description of the unexpectedly subtle relationship between the lifetime of a droplet on a solid substrate evaporating in a SS mode and those of initially identical droplets evaporating in the extreme modes which is summarised in the master diagram presented in figure 3.7. In particular, we showed that the lifetime of a droplet is not, in general, constrained by those of the extreme modes.

Chapter 4

Droplets in the Stick-Slide Mode with Related Initial and Receding Contact Angles

In the previous chapter we provided a complete description of the lifetime of a droplet evaporating in the SS mode and, in particular, showed that its lifetime is *not* always constrained to lie between the lifetimes of the extreme (*i.e.* the CR and CA) modes, as might have been naively assumed. We also showed that these theoretical predictions are in rather good agreement with the lifetimes measured experimentally by previous authors. In our analysis θ_0 and θ^* were assumed to be independent parameters, and the values of θ_0 and θ^* for each droplet were taken directly from the experimental measurements. In this chapter the consequences of a relationship between θ_0 and θ^* are investigated. Specifically, in section 4.1 we propose a simple relationship between θ_0 and θ^* based on the assumption of a constant maximum pinning force. In section 4.2 we use this relationship to give a complete description of the lifetime of a droplet evaporating in the idealised SS mode, and in section 4.3 we compare this relationship with the experimentally determined values of θ_0 and θ^* and the theoretically predicted lifetimes calculated using it with the experimentally determined lifetimes.

4.1 A Relationship Between θ_0 and θ^*

In this section we propose a simple relationship between θ_0 and θ^* based on the assumption of a constant maximum pinning force.

As mentioned in the previous chapter, if the initial contact angle is equal to the receding contact angle, *i.e.* if $\theta_0 = \theta^*$, then the contact line immediately de-pins and thereafter the droplet simply evaporates in the CA mode with $\theta = \theta_0 = \theta^*$ constant and R decreasing. However, if the initial contact angle is greater than the receding contact angle, *i.e.* if $\theta_0 > \theta^*$, then, as sketched in figure 4.1, the contact line is pinned by a pinning force per unit length $F_{\mathrm{p}} = F_{\mathrm{p}}(t)$ due to surface roughness and/or chemical heterogeneities of the substrate which opposes the unbalanced Young force, and the droplet begins to evaporate in a CR phase with $R = R_0$ constant and θ decreasing. Specifically, the horizontal force balance at the contact line reveals that F_{p} is given by

$$F_{\mathrm{p}}(t) = \gamma \cos(\theta(t)) + \gamma_{\mathrm{SF}} - \gamma_{\mathrm{SA}}, \tag{4.1}$$

where γ, γ_{SA} and γ_{SF} are the interfacial tensions of the fluid–atmosphere, substrate–atmosphere and substrate–fluid interfaces, respectively (see section 1.3). Note that in the special case of an ideal substrate with no pinning force, *i.e.* in the special case $F_{\mathrm{p}} = 0$, equation (4.1) reduces to the well-known Young–Laplace equation, (1.4), for $\theta = \theta_0$. As the droplet continues to evaporate, θ decreases and hence F_{p} increases until it reaches its maximum possible value, denoted by $F_{\mathrm{p\,max}}$, when

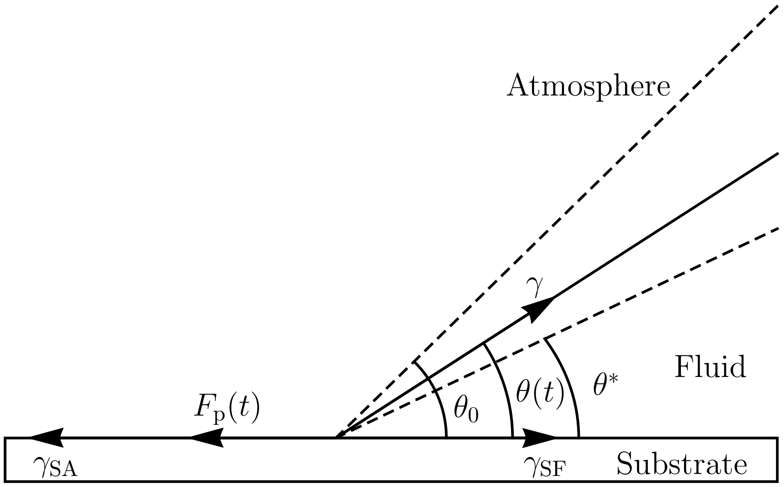

Figure 4.1: Sketch of the contact line of an evaporating droplet with contact angle $\theta(t)$ showing the pinning force $F_{\mathrm{p}}(t)$. The dashed lines show the initial contact angle θ_0 and the receding contact angle θ^* when $\theta_0 > \theta^*$.

$\theta = \theta^*$, at which instant the contact line de-pins and subsequently the droplet evaporates in a CA phase with $\theta = \theta^*$ constant and R decreasing. Subtracting the expression for the initial pinning force, $F_{\mathrm{p}}(0) = \gamma \cos\theta_0 + \gamma_{\mathrm{SF}} - \gamma_{\mathrm{SA}}$, from that for the maximum pinning force, $F_{\mathrm{p\,max}} = \gamma \cos\theta^* + \gamma_{\mathrm{SF}} - \gamma_{\mathrm{SA}}$, gives a relationship between θ_0 and θ^*, namely

$$\cos\theta^* - \cos\theta_0 = f_{\mathrm{p}}, \tag{4.2}$$

where

$$f_{\mathrm{p}} = \frac{F_{\mathrm{p\,max}} - F_{\mathrm{p}}(0)}{\gamma} \tag{4.3}$$

is the scaled difference between the maximum pinning force and the initial pinning force (hereafter simply referred to as the “maximum pinning force” for brevity). Note that, from (4.2), physically realisable values of f_{p} lie in the range $0 \leq f_{\mathrm{p}} \leq 2$, with the extreme values $f_{\mathrm{p}} = 0$ and $f_{\mathrm{p}} = 2$ corresponding to the case $\theta_0 = \theta^*$ and to the case $\theta_0 = \pi$ and $\theta^* = 0$, respectively.

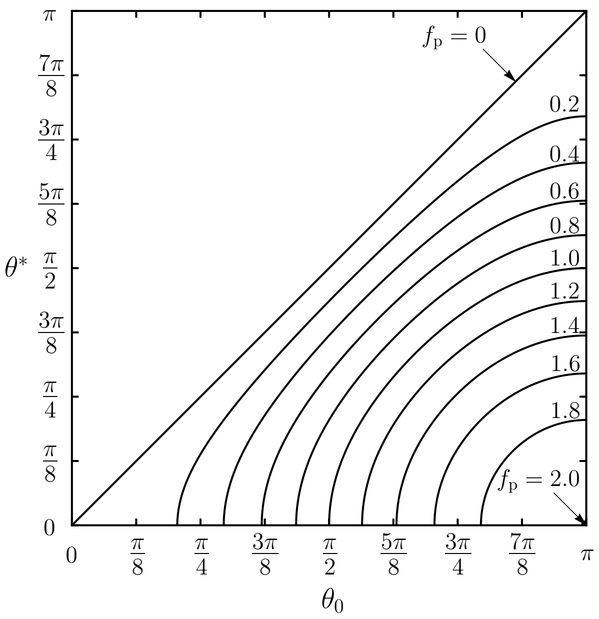

Figure 4.2: The receding contact angle θ^* $(0 \leq \theta^* \leq \theta_0)$ given by (4.4) plotted as a function of the initial contact angle θ_0 for various values of the maximum pinning force f_p spanning the full range of physically realisable values, $0 \leq f_\mathrm{p} \leq 2$, namely $f_\mathrm{p} = 0$, 0.2, 0.4, 0.6, 0.8, 1, 1.2, 1.4, 1.6, 1.8, and 2.

In general, the value of f_p will depend on the nature of the substrate, the fluid and the atmosphere as well as on some or all of the other parameters in the problem (including θ_0 and/or θ^*). In the present work we make the modelling assumption (whose validity will be tested by comparison with experimental results in section 4.3) that the maximum pinning force f_p is *constant* (*i.e.* independent of all of the other parameters in the problem and, in particular, independent of θ_0 and θ^*) and so (4.2) provides a simple expression for θ^* in terms of θ_0 and f_p, namely

$$\theta^* = \max(0, \arccos(f_\mathrm{p} + \cos\theta_0)). \tag{4.4}$$

This relationship between θ_0 and θ^* is crucial to all of the results presented in the remainder of the present work, and so figure 4.2 shows θ^* given by (4.4) plotted as a function of θ_0 for various values of f_p spanning the full range of physically realisable values, $0 \leq f_{\mathrm{p}} \leq 2$. For each value of f_{p}, the corresponding curve is symmetric about the line $\theta^* = \pi - \theta_0$, and intersects the θ_0-axis at the point $(\theta_{0,0}, 0)$ and the line $\theta_0 = \pi$ at the point $(\pi, \pi - \theta_{0,0})$, where $\theta_{0,0} = \arccos(1 - f_{\mathrm{p}})$. For values of θ_0 smaller than $\theta_{0,0}$ (*i.e.* when $0 \leq \theta_0 \leq \theta_{0,0}$) then (4.4) yields $\theta^* = 0$, so that the contact line never de-pins and the droplet evaporates in the CR mode, while for values of θ_0 larger than $\theta_{0,0}$ (*i.e.* when $\theta_{0,0} < \theta_0 \leq \pi$) then (4.4) yields $\theta^* = \arccos(f_{\mathrm{p}} + \cos\theta_0)$ $(0 < \theta^* \leq \pi - \theta_{0,0})$, and the droplet evaporates in the SS mode.

4.2 Theoretical Predictions for the Lifetime of a Droplet in the Stick-Slide Mode with Related Initial and Receding Contact Angles

In this section, we describe the consequences of the relationship between θ_0 and θ^* given by (4.4) on how t_{SS} depends on θ_0 and f_{p}. In particular, we compare t_{SS} with the lifetimes of initially identical droplets (*i.e.* droplets with the same values of R_0 and θ_0, and hence of V_0) evaporating in the extreme modes for the full range of all possible initial contact angles, *i.e.* for $0 \leq \theta_0 \leq \pi$.

As we have seen in the previous chapter the lifetimes of droplets evaporating in the extreme modes given by (2.10) and (2.11) are, by definition, independent of θ^* and hence of f_{p}. However, as we have already seen, the lifetime of a droplet evaporating in the SS mode with θ^* given by (4.4) depends, in general, on f_{p} as well as on θ_0, *i.e.* $t_{\mathrm{SS}} = t_{\mathrm{SS}}(\theta_0, f_{\mathrm{p}})$.

If $0 \leq \theta_0 \leq \theta_{0,0}$, where $\theta_{0,0} = \arccos(1 - f_{\mathrm{p}})$, then $\theta^* = 0$, so that the droplet evaporates in the CR mode, and hence its lifetime is simply given by $t_{\mathrm{SS}} = t_{\mathrm{CR}}(\theta_0)$, where t_{CR} is given by (2.10).

If $\theta_{0,0} < \theta_0 \leq \pi$ then the droplet evaporates in the SS mode with $\theta^* = \arccos(f_{\mathrm{p}} + \cos\theta_0)$, and hence its lifetime is the sum of the duration of the CR phase (*i.e.* the time it takes for θ to decrease from θ_0 to θ^* with $R = R_0$) and the duration of the CA phase (*i.e.* the time it takes for R to decrease from $R = R_0$ to $R = 0$ with $\theta = \theta^*$), and is given by (3.4) in the previous chapter. Note that (3.4) reduces to $t_{\mathrm{SS}} = t_{\mathrm{CR}}$ when $\theta^* = 0$, and so it is, in fact, valid for all values of θ_0.

Figure 4.3(a) shows t_{SS} given by (3.4) plotted as a function of θ_0 ($0 \leq \theta_0 \leq \pi$) for a range of values of f_{p}, together with the lifetimes of initially identical droplets evaporating in the extreme modes, t_{CR} and t_{CA}, given by (2.10) and (2.11), respectively. For clarity, figure 4.3(b) shows the behaviour in the range $\pi/2 \leq \theta_0 \leq \pi$ in greater detail.

The most striking feature of figure 4.3 is that the *shapes* of the curves representing t_{SS} are *qualitatively different* from those obtained in the previous chapter (figures 3.5 and 3.6) in the case when θ_0 and θ^* are independent parameters. Specifically, as figure 4.3 shows, whatever the value of f_{p}, the curves representing t_{SS} coincide with the curve representing t_{CR} for $0 \leq \theta_0 \leq \theta_{0,0}$, depart from it with vertical slope at $\theta_0 = \theta_{0,0}$ according to

$$t_{\mathrm{SS}} = t_{\mathrm{CR}} + \frac{2^{1/6}\pi(2 - f_{\mathrm{p}})^{5/4}}{8 f_{\mathrm{p}}^{1/12}(3 - f_{\mathrm{p}})^{2/3}}\sqrt{\theta_0 - \theta_{0,0}} + O\left(\theta_0 - \theta_{0,0}\right) \tag{4.5}$$

as $\theta_0 \to {\theta_{0,0}}^+$, increase to a local maximum at a value of θ_0 in the range $\pi/2 \leq \theta_0 \leq \pi$ (marked with a solid dot in figure 4.3(b)) and then decrease, ultimately reaching the value $t_{\mathrm{SS}} = t_\pi$ with zero slope at $\theta_0 = \pi$. For contrast, recall that, unlike the present curves, the corresponding curves in figures 3.5 and 3.6 coincide with the curve representing t_{CA} (not t_{CR}) when $0 \leq \theta_0 \leq \theta^*$ and depart from

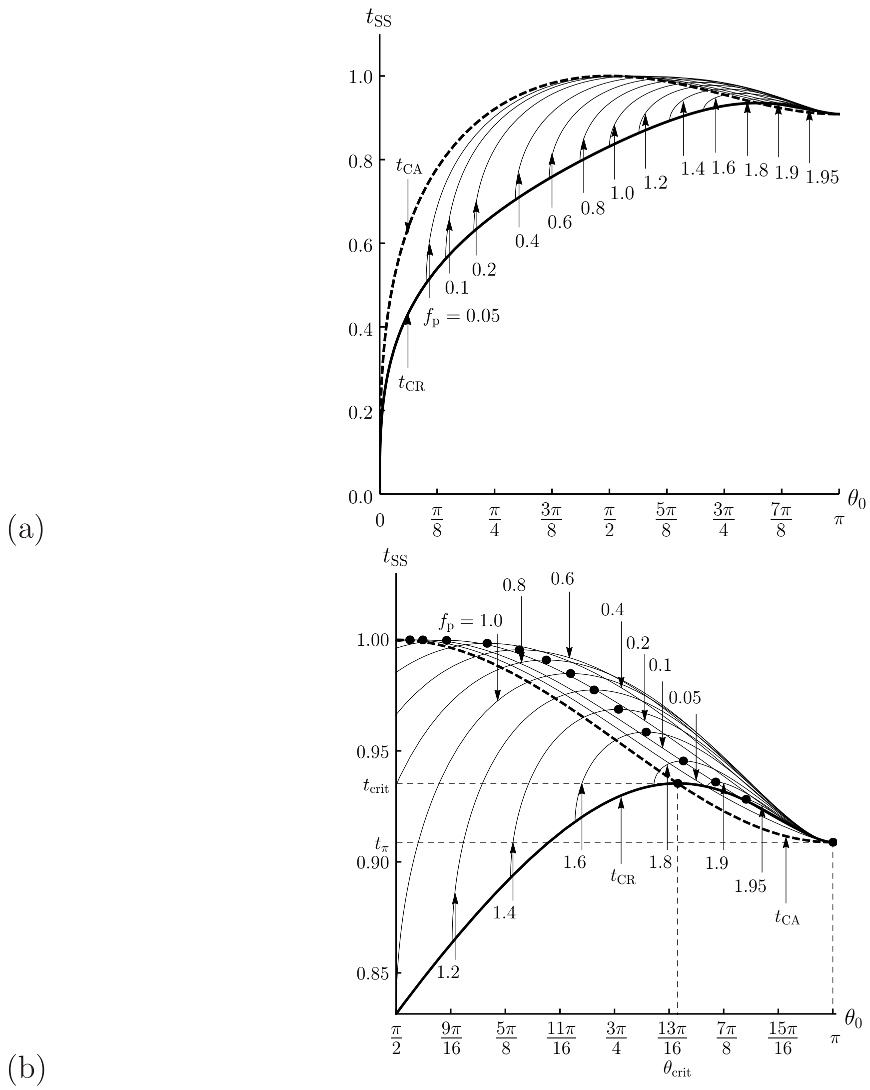

Figure 4.3: (a) The lifetime of a droplet evaporating in the SS mode, t_{SS}, given by (3.4) plotted as a function of the initial contact angle θ_0 ($0 \le \theta_0 \le \pi$) for a range of values of the maximum pinning force, f_p, namely $f_p = 0.05$, 0.1, 0.2, 0.4, 0.6, 0.8, 1.0, 1.2, 1.4, 1.6, 1.8, 1.9 and 1.95, together with the lifetimes of initially identical droplets evaporating in the extreme modes, t_{CR} and t_{CA}, given by (2.10) and (2.11), respectively. Part (b) shows the behaviour in the range $\pi/2 \le \theta_0 \le \pi$ in greater detail. Note that $t_{SS} = t_{CR}(\theta_0)$ when $0 \le \theta_0 \le \theta_{0,0}$, and that $t_{CR} = t_{CA} = t_{crit} \simeq 0.9354$ at $\theta_0 = \theta_{crit} \simeq 2.5830$ and $t_{SS} = t_{CR} = t_{CA} = t_\pi \simeq 0.9088$ at $\theta_0 = \pi$. In part (b) the local maximum of t_{SS}, which occurs at a value of θ_0 in the range $\pi/2 \le \theta_0 \le \pi$ and is also the global maximum of t_{SS} except when f_p lies in the range $1.9046 \le f_p \le 2$, is marked with a solid dot (●).

it with zero (not vertical) slope at $\theta_0 = \theta^*$. However, also recall that, like the present curves, the corresponding curves in figures 3.5 and 3.6 always lie below $t_{\mathrm{CA}}(\pi/2) = 1$ and always lie on or above the minimum of the two extreme modes (*i.e.* $t_{\mathrm{SS}} \geq \min(t_{\mathrm{CR}}, t_{\mathrm{CA}})$ for $0 \leq \theta_0 \leq \pi$), but may lie above the maximum of the two extreme modes when $\pi/2 < \theta_0 < \pi$. Moreover, the total envelope of the present curves as f_{p} varies between 0 and 2 is the same as the total envelope of the curves in figures 3.5 and 3.6 as θ^* varies between 0 and π.

As figure 4.3 illustrates, in the limit $f_{\mathrm{p}} \to 0^+$ then $\theta_{0,0} \to 0^+$ and the curve representing t_{SS} approaches that representing t_{CA} from below for $0 < \theta_0 \leq \pi/2$ and from above for $\pi/2 < \theta_0 < \pi$ according to

$$\begin{aligned} t_{\mathrm{SS}} = t_{\mathrm{CA}} &+ \left(\frac{2(1+\cos\theta_0)^2}{\sin\theta_0(2+\cos\theta_0)} \right)^{2/3} \\ &\times \left(\frac{3 - 2\cos\theta_0 - 2\cos^2\theta_0}{g(\theta_0)\sin\theta_0} + \frac{g'(\theta_0)(2+\cos\theta_0)}{g^2(\theta_0)} \right) f_{\mathrm{p}} + O\left(f_{\mathrm{p}}^2\right). \end{aligned} \tag{4.6}$$

Furthermore, as figure 4.3 also illustrates, in the limit $f_{\mathrm{p}} \to 2^-$ then $\theta_{0,0} \to \pi^-$ and the curve representing t_{SS} converges to that representing t_{CR} from above in the vanishingly small range $\theta_{0,0} < \theta_0 < \pi$. In addition, as figure 4.3(b) illustrates, for most values of f_{p} the local maximum of t_{SS} is also its global maximum, but for values of f_{p} sufficiently close to 2 (specifically, for values of f_{p} in the range $1.9046 \leq f_{\mathrm{p}} \leq 2$) the global maximum of t_{SS} is $t_{\mathrm{SS}} = t_{\mathrm{CR}} = t_{\mathrm{CA}} = t_{\mathrm{crit}}$ at $\theta_0 = \theta_{\mathrm{crit}}$. As figure 4.3(b) also illustrates, for most values of f_{p} the curves representing t_{SS} lie above the curve representing t_{CR} near $\theta_0 = \pi$, but for values of f_{p} in the range $0 \leq f_{\mathrm{p}} \leq f_{\mathrm{p}\pi}$, where $f_{\mathrm{p}\pi} \simeq 0.1520$, they lie below it (but still above the curve representing t_{CA}).

In summary, figure 4.3 shows that for sufficiently small values of θ_0 (*i.e.* for values in the range $0 \leq \theta_0 \leq \theta_{0,0}$) the droplet evaporates in the CR mode and has lifetime $t_{\mathrm{SS}} = t_{\mathrm{CR}}(\theta_0)$, while for larger values of θ_0 (*i.e.* for values in the range $\theta_{0,0} < \theta_0 \leq \pi$) the droplet evaporates in the SS mode and has lifetime $t_{\mathrm{SS}} = t_{\mathrm{SS}}(\theta_0, f_{\mathrm{p}})$ which is never less than both t_{CR} and t_{CA}.

Note that the present curves are qualitatively much more similar to (but still not identical to) that tentatively suggested by Shanahan *et al.* [204] (shown in figure 1.14) than those obtained in figures 3.5 and 3.6. In particular, Shanahan *et al.* [204] hypothesised the existence of a sigmoidal curve representing "a transition between the two [extreme] regimes over a range of intermediate values of θ_0 [approximately $20^\circ \leq \theta_0 \leq 45^\circ$], corresponding to the change between pinning and (virtually) continuous triple line [*i.e.* contact line] recession" but that "its position, however, is not known". In particular, while the present curves depart from the curve representing t_{CR} at $\theta_0 = \theta_{0,0}$ and cross the curve representing t_{CA} (albeit always at a value of θ_0 in the range $\pi/2 < \theta_0 < \pi$), they are not sigmoidal and have a more complicated structure than that envisaged in figure 1.14.

Since the results presented in figure 4.3 are fairly complicated, we follow the approach taken in the previous chapter and summarise all of the possible relationships between the lifetimes of initially identical droplets evaporating in the CR, CA and SS modes in the master diagram shown in figure 4.4, which shows how the θ_0–f_{p} parameter plane is divided up into regions in which the six possible orderings of t_{CR}, t_{CA} and t_{SS} occur. Four of these six regions, namely region I, which corresponds to $t_{\mathrm{CR}} < t_{\mathrm{SS}} < t_{\mathrm{CA}}$, region II, which corresponds to $t_{\mathrm{CR}} < t_{\mathrm{CA}} < t_{\mathrm{SS}}$, region III, which corresponds to $t_{\mathrm{CA}} < t_{\mathrm{CR}} < t_{\mathrm{SS}}$, and region IV, which corresponds to $t_{\mathrm{CA}} < t_{\mathrm{SS}} < t_{\mathrm{CR}}$, appear in the corresponding diagram, figure 3.7, in the previous chapter, and so are labelled in the same way. The other two regions, namely region VII, which corresponds to $t_{\mathrm{CA}} < t_{\mathrm{SS}} = t_{\mathrm{CR}}$, and region VIII, which corresponds to $t_{\mathrm{SS}} = t_{\mathrm{CR}} < t_{\mathrm{CA}}$, correspond to $\theta^* = 0$ and hence collapse onto the θ_0-axis in

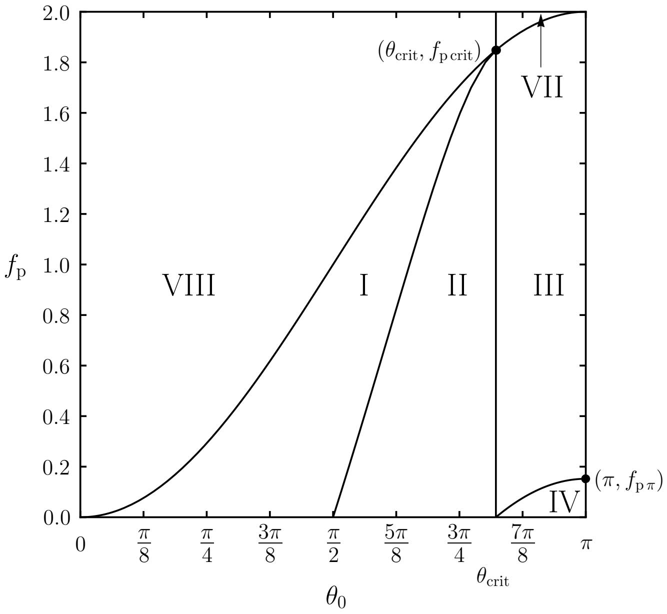

Figure 4.4: Master diagram showing how the θ_0–$f_{\rm p}$ parameter plane is divided up into regions in which the six possible orderings of the lifetimes of initially identical droplets evaporating in the CR, CA and SS modes occur. Region I corresponds to $t_{\rm CR} < t_{\rm SS} < t_{\rm CA}$, region II to $t_{\rm CR} < t_{\rm CA} < t_{\rm SS}$, region III to $t_{\rm CA} < t_{\rm CR} < t_{\rm SS}$, region IV to $t_{\rm CA} < t_{\rm SS} < t_{\rm CR}$, region VII to $t_{\rm CA} < t_{\rm SS} = t_{\rm CR}$, and region VIII to $t_{\rm SS} = t_{\rm CR} < t_{\rm CA}$. In particular, note that $t_{\rm SS} > \max(t_{\rm CR}, t_{\rm CA})$ in regions II and III. Note that regions I–IV, but not regions VII and VIII, appear in the corresponding diagram, figure 3.7 in the previous chapter, and that regions V and VI in figure 3.7 do not appear here.

the corresponding diagram, figure 3.7, and so appear here for the first time. Similarly, two additional regions in figure 3.7, namely region V, which corresponds to $t_{\rm SS} = t_{\rm CA} < t_{\rm CR}$, and region VI which corresponds to $t_{\rm CR} < t_{\rm SS} = t_{\rm CA}$, correspond to $f_{\rm p} = 0$ and hence collapse onto the θ_0-axis in figure 4.4 and so do not appear here. As figure 4.4 shows, as $f_{\rm p}$ increases from 0 to 2, region IV disappears as $f_{\rm p}$ passes through the critical value $f_{\rm p\,\pi} \simeq 0.1520$, and regions I and II disappear and region VII appears as $f_{\rm p}$ passes through the critical value $f_{\rm p\,crit}$, where $f_{\rm p\,crit}$ is the value of $f_{\rm p}$ at which $\theta_{0,0} = \theta_{\rm crit}$, *i.e.* $f_{\rm p\,crit} = 1 - \cos(\theta_{\rm crit}) \simeq 1.8480$. In particular, figure 4.4 confirms that $t_{\rm SS}$ is never less than both $t_{\rm CR}$ and $t_{\rm CA}$, and shows that regions I and IV (*i.e.* the regions in which $t_{\rm SS}$ lies between $t_{\rm CR}$ and $t_{\rm CA}$), regions

II and III (*i.e.* the regions in which t_{SS} is greater than both t_{CR} and t_{CA}), and regions VII and VIII (*i.e.* the regions in which $t_{\mathrm{SS}} = t_{\mathrm{CA}}$) all occupy substantial proportions of parameter space.

4.3 Comparison with Experimental Results

In figure 3.4 in the previous chapter we showed that the theoretical predictions of the present model are in rather good agreement with the lifetimes obtained from 29 sets of experimental data for droplets evaporating in an SS mode in which the second slide phase is smaller than 10% of the lifetime of the droplet obtained by previous authors. However, in order to make this comparison, the values of θ_0 and θ^* of these data sets, which are given in table 4.1 for reference, were taken directly from the experimental measurements. In particular, in the context of the present work, this is equivalent to determining the value of f_{p} *for each experiment* directly from the experimental measurements, and these values of f_{p} (calculated from the corresponding values of θ_0 and θ^* using (4.2)) are also given in table 4.1. The open question here is therefore to determine how well the relationship (4.4) *using only a single value of* f_{p} *for all of the experiments* agrees with the experimentally determined values of θ_0 and θ^*, and how well the theoretically predicted lifetimes calculated using this relationship agree with the experimentally determined lifetimes.

Figure 4.5 (a) shows f_{p} as a function of θ_0, while figure 4.5 (b) shows θ^* plotted as a function of θ_0 obtained from the 29 sets of experimental data listed in table 4.1. Figure 4.5 also includes a solid curve showing the value of f_{p} that best fits all 29 sets of experimental data, namely $f_{\mathrm{p}} = 0.2005$ in part (a) and the relationship (4.4) with this value of f_{p} in part (b). In figure 4.5 (b) the corresponding value of

Reference	Fluid	Substrate	θ_0	θ^*	f_p
Bourgès-Monnier and Shanahan [201]	Water	Polished epoxy resin	0.97	0.44	0.34
	Water	Polished epoxy resin	1.04	0.26	0.46
Uno *et al.* [235]	Latex dispersion	ODTES$_{100}$ on glass	1.83	1.66	0.17
Fukai *et al.* [76]	Water	SO$_3$H on silicon	0.87	0.56	0.20
	Water	SO$_3$H on silicon	0.85	0.52	0.21
	Xylene	R$_\mathrm{f}$ on silicon	1.19	1.10	0.08
Li *et al.* [126]	Water	Dialkyl disulfides on gold-covered mica	1.80	1.72	0.08
			1.44	1.31	0.13
			1.55	1.30	0.25
			1.31	1.20	0.11
			1.21	0.95	0.23
			1.14	0.95	0.17
			0.93	0.66	0.19
			0.78	0.57	0.13
			0.61	0.21	0.16
Song *et al.* [218]	Water	Platinum	1.61	1.41	0.20
Nguyen *et al.* [147]	Water	Oct-silicon	0.93	0.53	0.27
			0.93	0.57	0.25
			0.95	0.55	0.28
			0.92	0.56	0.24
	Water	Oct-silicon	0.96	0.65	0.23
	Water	OTS-silicon	1.81	1.64	0.16
	Water	Teflon	1.88	1.61	0.27
Lim *et al.* [128]	Water	Pyrex glass	1.14	0.67	0.36
	Diethylene glycol with coffee particles	Pyrex glass	0.68	0.37	0.15
Yu *et al.* [249]	Water	Teflon on PDMS on glass	2.01	1.90	0.10
Dash and Garimella [49]	Water	Teflon on silicon	2.14	1.99	0.13
			2.12	1.96	0.14
			2.08	1.93	0.14

Table 4.1: Details of the 29 sets of experimental data for droplets used in Chapter 3 and which will be used in figures 4.5 and 4.6. The values of θ_0 and θ^* were taken directly from the experimental measurements and the values of f_p were calculated from them using (4.2). The expressions for the abbreviations in the "Substrate" column can be found in table 3.1.

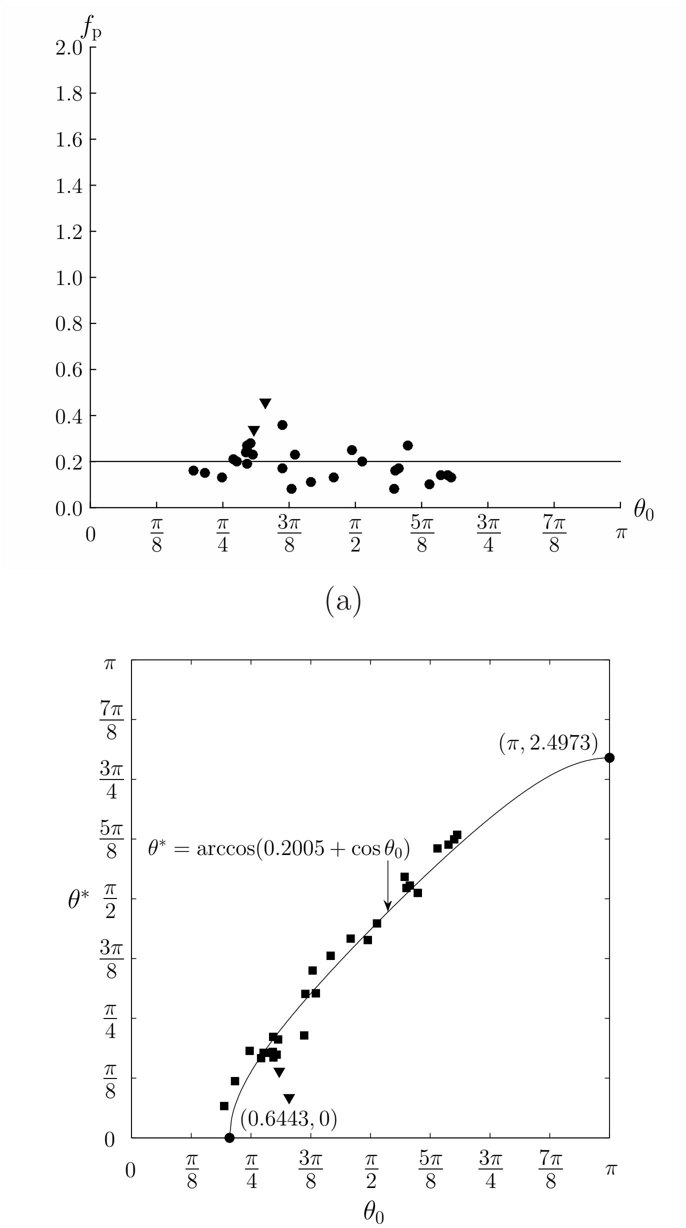

(a)

(b)

Figure 4.5: (a) The maximum pinning force f_p plotted as a function of the initial contact angle θ_0 and (b) the receding contact angle θ^* plotted as a function of the initial contact angle θ_0 obtained from the 29 sets of experimental data listed in table 4.1. The values from the two experiments by Bourgès-Monnier and Shanahan [201] are denoted by inverted triangles (▼) rather than by squares (■). The solid curve shows the value of f_p that best fits all 29 sets of experimental data, namely $f_p = 0.2005$ in part (a) and the relationship (4.4) with this value of f_p in part (b).

$\theta_{0,0}$ is $\theta_{0,0} \simeq 0.6443 \simeq 37^\circ$, and hence the corresponding values of θ^* vary between $\theta^* = 0$ and $\theta^* = \pi - \theta_{0,0} \simeq 2.4973 \simeq 143^\circ$.

As we have already described in section 4.1, in general, the value of f_p will depend on the nature of the substrate, the fluid and the atmosphere and so will, in general, be different for each of the different experiments, and this is confirmed by the range of values of f_p given in table 4.1. In so far as the previous authors listed in table 4.1 discuss the chemical composition of the substrates used in their experiments, they believe them to be chemically homogeneous, although Nguyen *et al.* [147] state that "the origin of the large CAH [contact angle hysteresis] on Oct-silicon may reflect surface chemical heterogeneity".

However, there is certainly considerable variation in the surface roughness of the substrates used in the different experiments. Probably the two most common methods of describing the roughness of the surface of a real substrate are the arithmetic average roughness, R_a, and the root mean square roughness, R_q, given by

$$R_a = \frac{1}{n}\sum_{i=1}^{n} |z(x_i)|, \tag{4.7}$$

and

$$R_q = \sqrt{\frac{1}{n}\sum_{i=1}^{n} z^2(x_i)}, \tag{4.8}$$

respectively, where $z(x)$ is the deviation of the substrate height from the mean height measured for a number, n, of equally spaced points x, denoted by x_i with $1 \leq i \leq n$. Note that these parameters provide a means to quantify surface roughness, but they are not able to completely characterise the topography of a substrate (see, for example, Ramiasa *et al.* [171]). Of those authors who quantify the roughness of their substrates, Bourgès-Monnier and Shanahan [201] give an R_a value of around 0.1 mm, Li *et al.* [126] give an R_q value of around 1 nm, and

Nguyen *et al.* [147] give R_q values of around 0.1 nm (modified silicon) and 10 nm (Teflon). In the light of all this, what is most immediately striking about the results presented in figure 4.5 is, despite the fact that they are from different experiments by different authors on a variety of substrates with a range of surface roughnesses and chemical heterogeneities using several fluids, how surprisingly close most of them lie to the relationship (4.4) with $f_\mathrm{p} = 0.2005$, *i.e.* how surprisingly well the relationship (4.4) with this single value of f_p holds for *all* 29 sets of experimental data. The quality of the fit is confirmed by an R^2 value of $R^2 = 0.9676$, and by the fact that even if the two experiments by Bourgès-Monnier and Shanahan [201] with the largest known roughness values and two of the three largest values of f_p in table 4.1 (denoted by inverted triangles rather than by squares in figure 4.5) are excluded, then the value of f_p that best fits all of the remaining 27 sets of experimental data decreases only slightly to 0.1858 and the corresponding R^2 value rises only slightly to $R^2 = 0.9800$.

Figure 4.6 shows the lifetimes of the droplets obtained from the 29 sets of experimental data listed in table 4.1 plotted as a function of θ_0. Also shown are the theoretical predictions for the lifetimes of initially identical droplets evaporating in the CR, CA and SS modes, t_CR, t_CA and t_SS, the latter calculated using $f_\mathrm{p} = 0.2005$. In particular, figure 4.6 shows that, while, as expected, the agreement is by no means perfect, the theoretical prediction for t_SS using this single value of f_p is reasonably close to *all* 29 of the experimentally determined lifetimes (even those from the two experiments by Bourgès-Monnier and Shanahan [201]), and that it captures the qualitative behaviour of the experimental results surprisingly well.

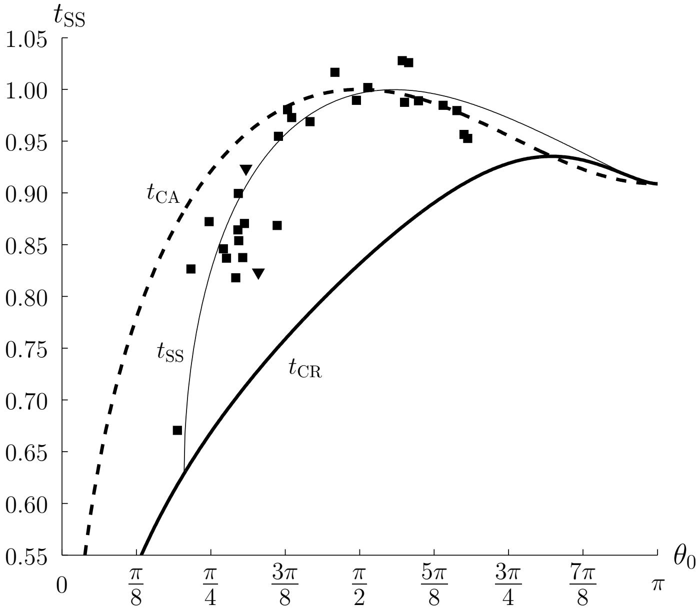

Figure 4.6: The lifetimes of the droplets obtained from the 29 sets of experimental data listed in table 4.1 plotted as a function of the initial contact angle θ_0. The lifetimes from the two experiments by Bourgès-Monnier and Shanahan [201] are denoted by inverted triangles (▼) rather than by squares (■). Also shown are the theoretical predictions for the lifetimes of initially identical droplets evaporating in the CR, CA and SS modes, t_{CR}, t_{CA} and t_{SS}, the latter calculated using $f_p = 0.2005$.

4.4 Summary

We proposed the simple relationship (4.4) between the initial contact angle θ_0 and the receding contact angle θ^* based on the assumption of a constant maximum pinning force f_p, and used this relationship to give a complete description of how the lifetime of a droplet evaporating in the idealised SS mode t_{SS} depends on θ_0 and f_p. In particular, we showed that the dependence of t_{SS} on θ_0 is qualitatively different from that described in the previous chapter in the case when θ_0 and θ^* are independent parameters, and is qualitatively much more similar to (but still not identical to) that tentatively suggested by Shanahan *et al.* [204] (see figure 1.14). Furthermore, we also showed that both the relationship (4.4) using only a single value of f_p for all of the experiments and the theoretically predicted lifetimes calculated using it agree surprisingly well with the experimentally determined values of θ_0 and θ^*, and the experimentally determined lifetimes, respectively. Despite this impressive level of agreement, we do not, of course, seek to claim that the present model using a single value of f_{p} is the universal model for droplet evaporation. Rather, we simply wish to point out that, since the present model yields theoretically predicted lifetimes that are in surprisingly good agreement with all of the experimentally determined lifetimes obtained from all 29 sets of experimental data listed in table 4.1, it it likely to be a useful description of droplet evaporation in a wide range of situations.

Chapter 5

Droplets in the Stick-Jump Mode

Whereas in the previous two chapters we focused on the evaporation of droplets evaporating in the SS mode, the following two chapters focus on droplets evaporating in the stick-jump (SJ) mode, which comprises a number of stick phases in which the contact radius R is constant and θ decreases, and a number of rapid jump phases, in which the contact angle θ jumps to a higher value and R jumps to a lower value (see Chapter 1). A simple model for a droplet in the SJ mode is proposed in section 5.1; this model does not attempt to resolve the details of the local behaviour at the contact line, but captures the global behaviour of the droplet. The model is used to give a complete description of the evolution of a droplet in the SJ mode in section 5.2, and in the limit of small contact angles in section 5.3. Furthermore, we show in section 5.4 that in appropriate special cases the proposed model of the SJ mode reduces to models for previously discussed simpler modes of evaporation. In section 5.5 we discuss the model for the SJ mode developed in the recent publication by Dietrich *et al.* [56] and compare it with our proposed model. In section 5.6 we test the validity of assumptions made in the model by comparison with experimental results available in the literature and, finally, in section 5.7 we compare experimentally determined values of both the change in contact radius during a jump phase and the duration of a stick phase with the theoretically predicted values. Then in Chapter 6 we use the proposed model to describe the lifetime of a droplet evaporating in the SJ mode.

5.1 Modelling the Stick-Jump Mode

As discussed in Chapter 1, surface roughness and/or chemical heterogeneity can cause the pinning of the contact line of a droplet. The pinning and de-pinning of the contact line was described in the previous chapter in terms of a maximum pinning force. For a droplet evaporating in the SJ mode, in which the contact line pins, de-pins and re-pins multiple times, the behaviour of the contact line can also be described in terms of a minimum as well as a maximum pinning force. For droplets with suspended particles this pinning, de-pinning and re-pinning of the contact line is influenced by the deposition of particles and can lead to multiple ring deposition patterns (see figure 1.2 (d)). However, in this thesis we will not attempt to model the local behaviour at the contact line in detail, but only the global behaviour of the droplet by describing the evolutions of R, θ, and hence V. Figure 5.1 gives an example of the evolution of a water droplet with a 0.1% concentration of titanium oxide particles evaporating on a CYTOP substrate showing three jump phases, as observed in the experiments by Orejon *et al.* [153]. Two main observations can be made from figure 5.1, and these will be used to develop a simple model capturing the global behaviour of droplets evaporating in the SJ mode. Firstly, figure 5.1 shows that the jump phases occur on a much shorter time scale than the stick phases; this behaviour has also been observed by Moffat *et al.* [144], Askounis *et al.* [5, 6, 7], McHale *et al.* [142], Xu *et al.* [245], and Kajiya *et al.*

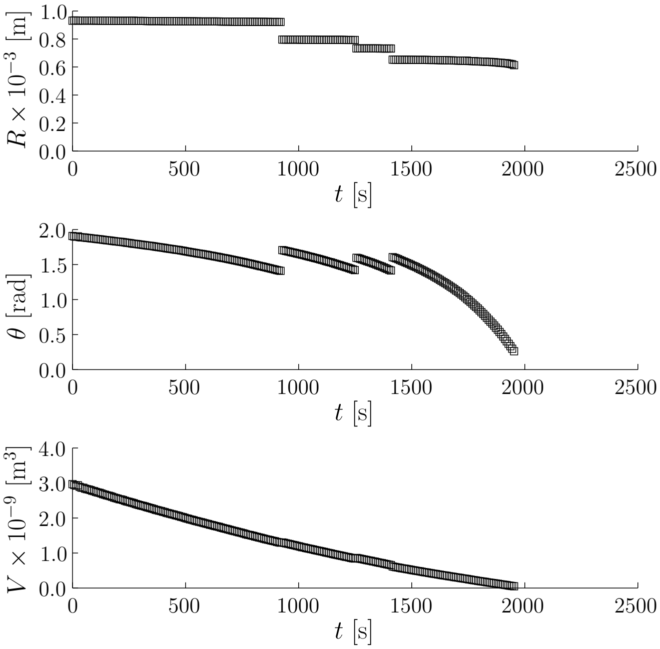

Figure 5.1: Evolution of the contact radius R, the contact angle θ, and volume V of a droplet evaporating in the stick–jump (SJ) mode as observed in the experiment by Orejon *et al.* [153] for a water droplet with 0.1% concentration of titanium oxide particles evaporating on a CYTOP substrate.

[108]. For example, the typical duration of a jump phase is less than 8 s (which is the interval at which the measurements were taken), while the average duration of a stick phase is about 8 minutes for the data set of Orejon *et al.* [153] shown in figure 5.1. Thus we assume that jump phases occur instantaneously in the proposed model. Secondly, figure 5.1 shows that both the contact angles at which the contact line de-pins and the contact angles at which the contact line re-pins remain approximately constant throughout the entire evaporation process. Note that, in general, these two contact angles may not always remain constant; for example, in some circumstances inertial effects or the deposition of particles may cause the contact angles at which the contact line de-pins and re-pins to vary. Therefore, we assume in the proposed model that the contact angles at which the contact line de-pins and re-pins, denoted by $\theta_{\min}$ and $\theta_{\max}$, respectively, are

constant throughout the entire evaporation process.

The proposed model for a droplet evaporating in the SJ mode comprises alternating stick and jump phases. During the n^{th} $(n \geq 1)$ stick phase, the contact line is pinned and the contact radius R takes the constant value R_n, the contact angle $\theta = \theta(t)$ decreases non-linearly to θ_{min}, the contact angle at which the contact line de-pins, and the volume V decreases non-linearly. We denote the time of the end of the n^{th} stick phase by t_n. During the n^{th} jump phase, which occurs instantaneously at $t = t_n$, R decreases discontinuously from R_n to a new value R_{n+1} $(\leq R_n)$, $\theta = \theta(t)$ increases discontinuously from θ_{min} to θ_{max} (with $\theta_{\text{min}} \leq \theta_{\text{max}}$), and the volume V is constant. Note that the droplet always first evaporates in a stick phase starting at $t_0 = 0$ with $\theta = \theta_0$ $(\geq \theta_{\text{min}})$, where again θ_0 denotes the initial contact angle. In particular, this means that for the first stick phase the contact radius R_1 is given by $R_1 \equiv R_0$, where again R_0 denotes the initial contact radius.

A sketch of a droplet evaporating in the simplified model for the SJ mode considered in the present work is given in figure 5.2. In particular, part (a) shows the evolution of the contact radius R, the contact angle θ, and volume V of a droplet. Parts (b) and (c) show sketches of the change in the droplet profiles during the n^{th} stick phase and the n^{th} jump phase, respectively.

As in the previous three chapters, we assume that the diffusion of vapour into the surrounding air is the rate-limiting mechanism of evaporation (see section 1.5.1), so that the rate of change of the volume of the droplet, $\mathrm{d}V/\mathrm{d}t$, during the n^{th} stick phase is given by equation (1.17), where $R = R_n$ is constant and $\theta = \theta(t)$ varies.

The present simple model will be used to describe the evolution of droplets in the SJ mode, in particular, by describing the evolutions of R, θ and V as the

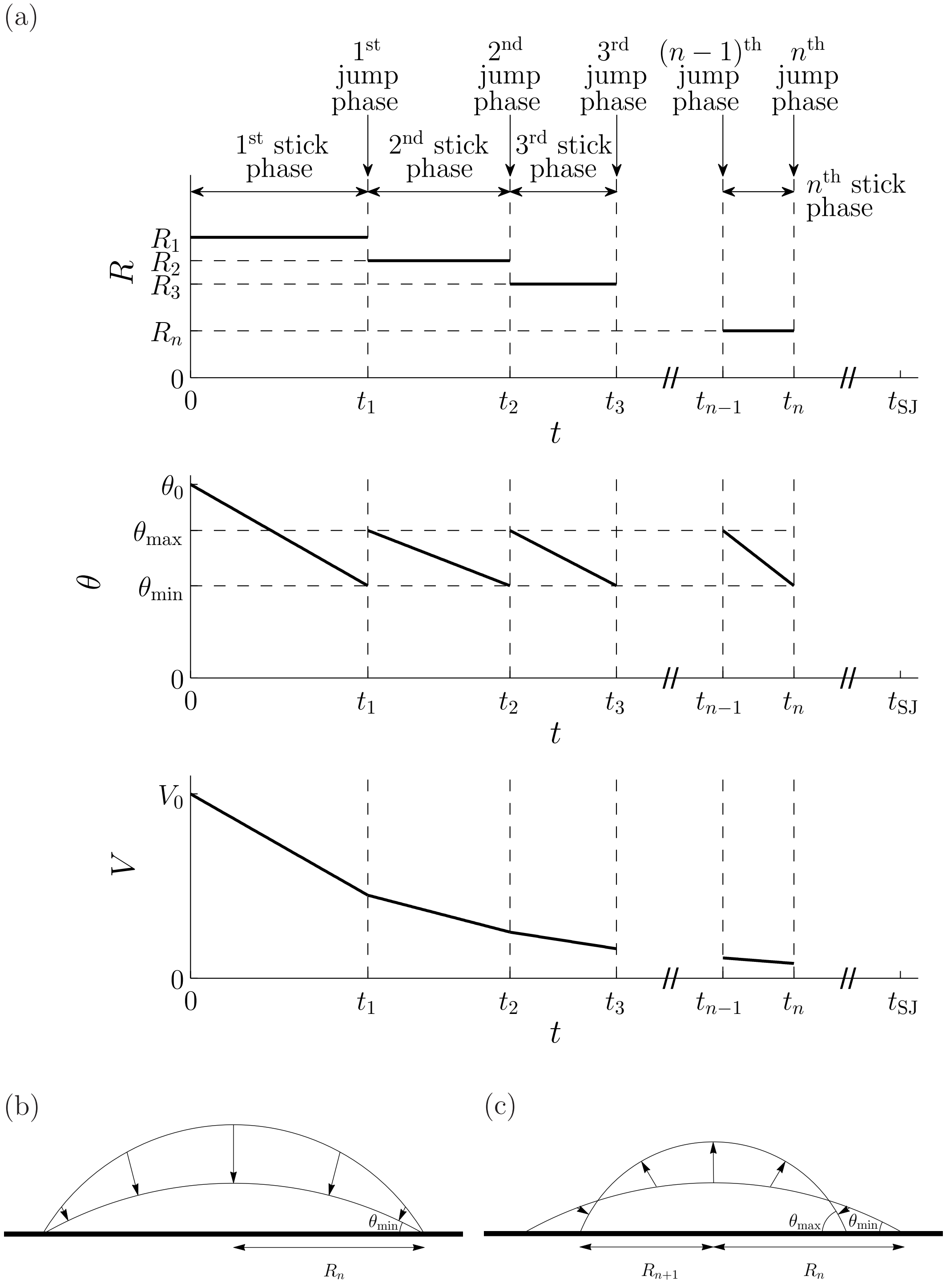

Figure 5.2: Sketches of (a) the evolution of the contact radius R, the contact angle θ, and volume V of a droplet evaporating in the stick–jump (SJ) mode considered in the present work. During the n^{th} stick phase, which occurs for time t in the interval $t_{n-1} < t < t_n$, the contact radius $R = R_n$ is constant, the contact angle $\theta(t)$ decreases non-linearly to a constant value θ_{min}, and the volume V decreases non-linearly, while during the n^{th} jump phase, which occurs instantaneously at $t = t_n$, R decreases discontinuously from R_n to a new value R_{n+1}, θ increases discontinuously to θ_{max}, and V is constant. Parts (b) and (c) show sketches of the change in the droplet profiles during the n^{th} stick phase and the n^{th} jump phase, respectively.

droplet evaporates, in the following section.

5.2 The Evolution of Droplets in the Stick-Jump Mode

As we have described previously, during the n^{th} jump phase R and θ are discontinuous and V is constant. This has two important consequences for the evolution of a droplet in the SJ mode. Firstly, the evolutions of R, θ, and hence V, are given by piecewise functions. Specifically, $R(t)$ is piecewise constant with discontinuous jumps to lower values, $\theta(t)$ is piecewise non-linearly decreasing with discontinuous jumps to higher values, and $V(t)$ is non-linearly but continuously decreasing with a discontinuous slope at each jump. Secondly, as V is constant during the n^{th} instantaneous jump phase, the volume at the end of the n^{th} stick phase is the same as the volume at the start of the $(n+1)^{\text{th}}$ stick phase. Therefore, using equation (1.2) we have

$$\frac{\pi R_n^3}{3}\frac{\sin\theta_{\min}(2+\cos\theta_{\min})}{(1+\cos\theta_{\min})^2} = \frac{\pi R_{n+1}^3}{3}\frac{\sin\theta_{\max}(2+\cos\theta_{\max})}{(1+\cos\theta_{\max})^2}, \tag{5.1}$$

where the left-hand and right-hand sides of the equation represent V just before the n^{th} jump phase and just after the n^{th} jump phase, respectively. Thus, rearranging (5.1) we obtain the following relationship between R_n and R_{n+1}:

$$R_{n+1} = \Lambda R_n = \Lambda^n R_1 \equiv \Lambda^n R_0, \tag{5.2}$$

where $\Lambda = \Lambda(\theta_{\min}, \theta_{\max})$ is given by

$$\Lambda = \frac{\sin\theta_{\max}}{\sin\theta_{\min}}\left(\frac{\cos^3\theta_{\min} - 3\cos\theta_{\min} + 2}{\cos^3\theta_{\max} - 3\cos\theta_{\max} + 2}\right)^{1/3} < 1. \tag{5.3}$$

Thus $R(t)$ is piecewise constant with $R(t) = R_n = \Lambda^{n-1}R_0$ in the interval $t_{n-1} < t < t_n$. From equation (5.2) the change in the contact radius during the n^{th} jump phase, $\delta R_n = R_n - R_{n+1}$, can be expressed as a function of R_n only, namely

$$\delta R_n = (1 - \Lambda)R_n. \tag{5.4}$$

Since $R(t)$ is piecewise constant, equation (1.17) becomes an equation for $\theta = \theta(t)$, namely

$$\frac{\mathrm{d}\theta}{\mathrm{d}t} = -\frac{D(c_{\text{sat}} - c_\infty)}{\rho}\frac{g(\theta)}{R_n^2}, \tag{5.5}$$

in the interval $t_{n-1} < t < t_n$. Equation (5.5) can be solved numerically subject to one of the following two initial conditions: for the first stick phase ($n = 1$) θ starts from θ_0, *i.e.* $\theta = \theta_0$ at $t = 0$, and for all subsequent stick phases ($n > 1$) θ starts from θ_{max}, *i.e.* $\theta = \theta_{\text{max}}$ at $t = t_{n-1}$.

Integrating equation (5.5) subject to the appropriate initial condition for $t_{n-1} < t < t_n$ gives the entire evolution for $\theta = \theta(t)$, and hence for $V = V(t)$ and the duration of the n^{th} stick phase, denoted by $\delta t_n = t_n - t_{n-1}$. In particular, since $t_0 = 0$, the duration of the first stick phase, δt_1, is given by t_1, the time at which the first stick phase ends, namely

$$\delta t_1 = t_1 = \frac{\rho}{D(c_{\text{sat}} - c_\infty)}R_0^2\int_{\theta_{\text{min}}}^{\theta_0}\frac{\mathrm{d}\theta}{g(\theta)}, \tag{5.6}$$

or, equivalently,

$$\delta t_1 = k_0 R_0^2, \tag{5.7}$$

where the constant k_0 is given by

$$k_0 = \frac{\rho}{D(c_{\text{sat}} - c_\infty)}\int_{\theta_{\text{min}}}^{\theta_0}\frac{\mathrm{d}\theta}{g(\theta)}. \tag{5.8}$$

Using equation (5.2) the duration of all subsequent stick phases ($n > 1$) is given by

$$\delta t_n = \frac{\rho}{D(c_{\mathrm{sat}} - c_\infty)} \Lambda^{2(n-1)} R_0^2 \int_{\theta_{\mathrm{min}}}^{\theta_{\mathrm{max}}} \frac{\mathrm{d}\theta}{g(\theta)} \tag{5.9}$$

or, equivalently,

$$\delta t_n = k R_n^2, \tag{5.10}$$

where the constant k is given by

$$k = \frac{\rho}{D(c_{\mathrm{sat}} - c_\infty)} \int_{\theta_{\mathrm{min}}}^{\theta_{\mathrm{max}}} \frac{\mathrm{d}\theta}{g(\theta)}. \tag{5.11}$$

The time at which the n^{th} stick phase ends, namely $t = t_n$, is obtained by adding the durations of *all* of the preceding stick phases, *i.e.*

$$t_n = \delta t_1 + \delta t_2 + \delta t_3 + \ldots + \delta t_n = \sum_{i=0}^{n-1} \delta t_{i+1}. \tag{5.12}$$

Therefore, using equations (5.6) and (5.9) we obtain

$$t_n = \frac{\rho}{D(c_{\mathrm{sat}} - c_\infty)} R_0^2 \left(\int_{\theta_{\mathrm{max}}}^{\theta_0} \frac{\mathrm{d}\theta}{g(\theta)} + \sum_{i=0}^{n-1} \Lambda^{2i} \int_{\theta_{\mathrm{min}}}^{\theta_{\mathrm{max}}} \frac{\mathrm{d}\theta}{g(\theta)} \right) \tag{5.13}$$

and hence we obtain the following explicit expression for t_n:

$$t_n = \frac{\rho}{D(c_{\mathrm{sat}} - c_\infty)} R_0^2 \left(\int_{\theta_{\mathrm{max}}}^{\theta_0} \frac{\mathrm{d}\theta}{g(\theta)} + \frac{1 - \Lambda^{2n}}{1 - \Lambda^2} \int_{\theta_{\mathrm{min}}}^{\theta_{\mathrm{max}}} \frac{\mathrm{d}\theta}{g(\theta)} \right). \tag{5.14}$$

As described previously, a droplet evaporates completely, *i.e.* $V = 0$, when R and/or θ are equal to zero. However, in the present model θ is bounded below by θ_{min}, so that $V = 0$ if and only if $R = 0$. Equation (5.2) shows that $R \neq 0$ for finite n, but that $R \to 0$ as $n \to \infty$. In other words, according to the present model infinitely many stick and jump phases are required for the droplet to evaporate

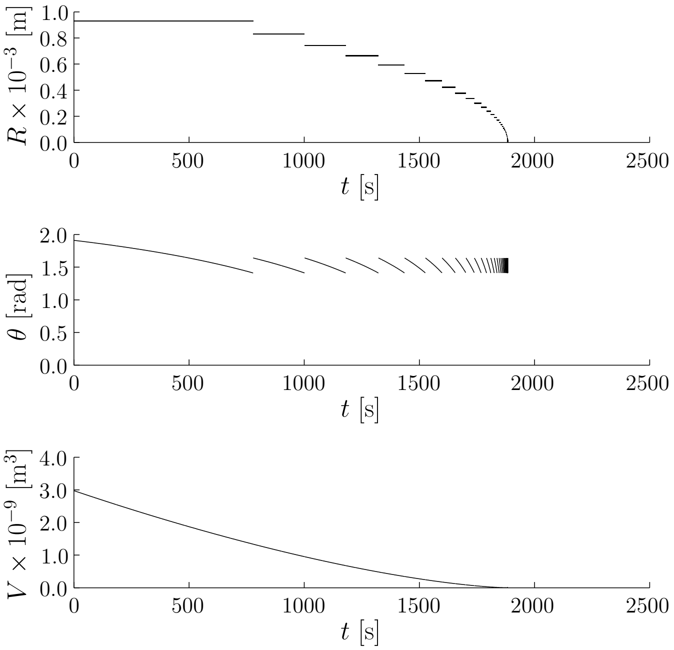

Figure 5.3: Theoretically predicted evolution of the contact radius R, the contact angle θ, and volume V of a droplet evaporating in the SJ mode using the experimentally determined values from the experiment by Orejon *et al.* [153] for a water droplet with a 0.1% concentration of titanium oxide particles evaporating $\theta_0 = 1.91$, $\theta_{\min} = 1.41$, $\theta_{\max} = 1.64$ and $R_0 = 0.93 \times 10^{-3}$ m.

completely. Letting $n \to \infty$ in equation (5.14) shows that this infinite number of stick and jump phases occurs in a finite time (and not, as might have been naively assumed, in an infinite time), denoted by t_{SJ}. In the next chapter we shall analyse the lifetime of a droplet in the SJ mode, t_{SJ}, in greater detail.

Figure 5.3 shows the theoretically predicted evolution of R, θ and V of a droplet evaporating in the SJ mode using the experimentally determined values from the experiment by Orejon *et al.* [153] for a water droplet with a 0.1% concentration of titanium oxide particles evaporating on a CYTOP substrate with $\theta_0 = 1.91$, $\theta_{\min} = 1.41$, $\theta_{\max} = 1.64$ and $R_0 = 0.93 \times 10^{-3}$ m. The means of determining these values from experiments will be described in detail in section 5.6.

Equations (5.4), (5.6) and (5.10) show that δR_n and δt_n $(n \geq 1)$ can be expressed as a function of R_n only and, in particular, that $\delta R_n \propto R_n$ and $\delta t_n \propto R_n^2$.

Thus the model predicts that, as the droplet evaporates R_n decreases and hence the change in R during a jump phase as well as the duration of the stick phases decrease (see figure 5.3). Also note that the present prediction $\delta R_n \propto R_n$ is different from the result derived by Shanahan [201], namely $\delta R_n \propto \sqrt{R_n}$, whose model of the pinning and de-pinning of the contact line is described in Chapter 1. This difference comes from the fact that whereas in the present model $\delta\theta = \theta_{\max} - \theta_{\min}$ is a prescribed constant, in the model described by Shanahan [201] $\delta\theta$ is not a constant, but is determined using a Gibbs free energy argument. Thus in cases when $\delta\theta$ is approximately constant, $\delta R_n \propto R_n$ describes the relationship between δR_n and R_n more accurately than $\delta R_n \propto \sqrt{R_n}$. Note that Shanahan [201] did not give an explicit expression for the δt_n.

In summary, we have developed a model that is based on the assumptions that the jump phases occur instantaneously, that $\theta_{\min}$ and $\theta_{\max}$ are constant throughout the entire evaporation process, and that during the n^{th} stick phase the contact radius is constant, which we used to describe the evolution of a droplet in the SJ mode. Although in the present work we consider the whole range of contact angles, $0 \le \theta \le \pi$, in the following section we investigate the present model in the limit of small contact angles, which, as we shall show, leads to considerable mathematical simplifications.

5.3 The Evolution of Droplets in the Stick-Jump Mode in the Limit of Small Contact Angles

In the limit of small contact angles, *i.e.* $\theta \to 0^+$, with, in particular, θ_0, $\theta_{\min}$ and $\theta_{\max} \to 0^+$, the previously obtained results for the evaporation of a droplet in the SJ mode simplify considerably.

In the limit of small contact angles the expression for V, given by (1.2), reduces to

$$V = \frac{\pi}{4} R^3 \theta, \tag{5.15}$$

so that, since V is constant during the n^{th} jump phase, equation (5.1) reduces to

$$\frac{\pi}{4} R_n^3 \theta_{\text{min}} = \frac{\pi}{4} R_{n+1}^3 \theta_{\text{max}}. \tag{5.16}$$

Thus, the relationship between R_n and R_{n+1} given by (5.2) reduces to

$$R_{n+1} = \lambda R_n = \lambda^n R_1 \equiv \lambda^n R_0, \tag{5.17}$$

where $\lambda = \lambda(\theta_{\text{min}}, \theta_{\text{max}})$ is the small angle limit of Λ given by (5.3), namely

$$\lambda = \left(\frac{\theta_{\text{min}}}{\theta_{\text{max}}} \right)^{1/3} < 1, \tag{5.18}$$

so that $R(t)$ is piecewise constant with $R(t) = R_n = \lambda^{n-1} R_0$ in the interval $t_{n-1} < t < t_n$.

As stated in section 1.5.1, $g(0) = 16/\pi$, so that using (5.17) the rate of change of θ, given by (5.5), reduces to

$$\frac{\mathrm{d}\theta}{\mathrm{d}t} = -\frac{16 D (c_{\text{sat}} - c_\infty)}{\pi \rho \lambda^{2(n-1)} R_0^2} \tag{5.19}$$

in the interval $t_{n-1} < t < t_n$, subject to the appropriate initial condition discussed in the previous section. Thus, the evolution of θ in the first stick phase is given by

$$\theta(t) = \theta_0 - \frac{16 D (c_{\text{sat}} - c_\infty)}{\pi \rho R_0^2} t, \tag{5.20}$$

and in all subsequent stick phases ($n > 1$) is given by

$$\theta(t) = \theta_{\mathrm{max}} - \frac{16D(c_{\mathrm{sat}} - c_\infty)}{\pi\rho\lambda^{2(n-1)}R_0^2}\left(t - t_{n-1}\right). \tag{5.21}$$

Similarly, expressions for the duration of the first stick phase, δt_1, given by (5.6), and the duration of all subsequent stick phases ($n > 1$), δt_n, given by (5.9), reduce to

$$t_1 = \frac{\pi\rho}{16D(c_{\mathrm{sat}} - c_\infty)}R_0^2(\theta_0 - \theta_{\mathrm{min}}) \tag{5.22}$$

and

$$\delta t_n = \frac{\pi\rho}{16D(c_{\mathrm{sat}} - c_\infty)}\lambda^{2(n-1)}R_0^2(\theta_{\mathrm{max}} - \theta_{\mathrm{min}}), \tag{5.23}$$

respectively, and hence the time at which the n^{th} stick phase ends, t_n, reduces to

$$t_n = \frac{\pi\rho}{16D(c_{\mathrm{sat}} - c_\infty)}R_0^2\left(\frac{1-\lambda^{2n}}{1-\lambda^2}\left(\theta_{\mathrm{max}} - \theta_{\mathrm{min}}\right) + \theta_0 - \theta_{\mathrm{max}}\right). \tag{5.24}$$

Having described the evolution of droplets in the SJ mode in the limit of small contact angles in this section, we shall continue to consider the whole range of contact angle, *i.e.* $0 \leq \theta \leq \pi$, for the remainder of the present work. In the next section we shall show that in appropriate special cases the present model for the SJ mode reduces to previously discussed models for simpler modes of evaporation.

5.4 “Universality” of the Model

As described in Chapter 1, many different modes of evaporation including the extreme (CR and CA) modes and the SS mode described in the previous chapters have been observed experimentally. The present model of the SJ mode can be considered a “universal” model in the sense that in appropriate special cases it reduces to models for all three of these simpler modes of evaporation. Specifically, in the special case $\theta_{\mathrm{min}} = 0$ the SJ mode comprises a single stick phase with $R = R_0$ constant and θ decreasing from θ_0 to $\theta_{\mathrm{min}} = 0$, and so the CR mode is recovered. In the special case $\theta_{\mathrm{min}} = \theta_{\mathrm{max}} := \theta^*$ the SJ mode comprises a first stick phase with $R = R_0$ constant and θ decreasing from θ_0 to θ_{min} followed by an infinite number of stick and jump phases in which $\theta = \theta_{\mathrm{min}} = \theta_{\mathrm{max}} = \theta^*$ is constant and R decreases from R_0 to zero, and so the SS mode described in Chapters 3 and 4 is recovered. In the special case $\theta_0 = \theta_{\mathrm{min}} = \theta_{\mathrm{max}}$ the SJ mode comprises an infinite number of stick and jump phases in which $\theta = \theta_0 = \theta_{\mathrm{min}} = \theta_{\mathrm{max}}$ is constant and R decreases from R_0 to zero, and so the CA mode is recovered. In the special case $\theta_0 = \theta_{\mathrm{max}}$ the simplified version of the model of the SJ mode recently proposed by Dietrich *et al.* [56] is recovered; this model of the SJ mode will be discussed further in the following section.

5.5 On the Recent Publication by Dietrich *et al.* [56]

In a recent publication Dietrich *et al.* [56] modelled the dissolution of sessile alcohol droplets in water by considering the mathematically equivalent problem of an evaporating sessile droplet. In particular, they developed a model for a droplet evaporating in the SJ mode. As in the present model, Dietrich *et al.* [56] assumed in their model that the jump phases occur instantaneously and that, in our notation, θ_{min} and θ_{max} remain constant throughout the entire evaporation process. In particular, they used the fact that the volume is constant during the jump phases, given by (5.1), to derive the same relationship between R_n and R_{n+1}, (5.2), and described the duration of the n^{th} stick phase, (5.9), and hence the lifetime of a droplet in the SJ mode. However, unlike the present model, in which θ_0, $\theta_{\min}$ and $\theta_{\max}$ are all independent parameters, Dietrich *et al.* [56] proposed a simplified version of the model in which $\theta_0 = \theta_{\max}$. In other words, unlike in the present model in which the first stick phase is, in general, qualitatively different from all of the subsequent stick phases (since θ decreases from θ_0 and not from $\theta_{\max}$), in the model proposed by Dietrich *et al.* [56] the first stick phase is qualitatively the same as all of the subsequent stick phases (since θ always decreases from $\theta_0 = \theta_{\max}$). However, Dietrich *et al.* [56] themselves, as well as, for example, Orejon *et al.* [153] and Askounis *et al.* [6, 7], showed that in practice θ_0 will not necessarily be equal to $\theta_{\max}$. The difference between θ_0 and $\theta_{\max}$ reflects the different conditions of the pinning of the contact line: when the droplet is first deposited onto the substrate, the contact line is pinned on a dry substrate, whereas when the contact line re-pins during a jump phase the contact line re-pins on a previously wetted substrate. Thus, the present model, unlike the model developed by Dietrich *et al.* [56], captures these different conditions of the pinning of the contact line. Despite the fact that the present model is made more complicated by having an additional parameter, we shall still be able to use it to describe the lifetime of a droplet in the SJ mode in the next chapter. However, we first test the validity of the assumptions built into the model by comparison with experimental results in the next section.

5.6 Comparisons between the Assumptions of the Model and Experimental Results

As described previously, the present model is based on the assumptions that the jump phases occur instantaneously, that $\theta_{\min}$ and $\theta_{\max}$ are constant throughout the entire evaporation process, and that during the n^{th} stick phase the contact radius is constant. The validity of these assumptions is tested by comparison with the results of relevant physical experiments available in the literature.

In particular, we use the twelve data sets of experimental results for droplets evaporating in the SJ mode obtained by Moffat *et al.* [144], Askounis *et al.* [5, 6, 7], and Orejon *et al.* [153]. These data sets involve water or ethanol droplets with different concentrations of titanium oxide or silicon dioxide nanoparticles evaporating on CYTOP, PTFE or silicon substrates, in either air or nitrogen atmospheres. Details of these twelve data sets can be found in table 5.1 and the parameters that characterise the evaporation of these droplet are given in table 5.2.

In these data sets we define a jump phase to occur when θ increases by at least 1° for consecutive data points. The experimentally determined values of θ_0 are defined to be the values of θ at $t = 0$. The experimentally measured values of θ just before and just after the n^{th} jump phase, denoted by $\theta_{\min n}$ and $\theta_{\max n}$, respectively, are averaged to obtain the experimentally determined values for $\theta_{\min}$ and $\theta_{\max}$, respectively. The experimentally determined values for θ_0, $\theta_{\min}$ and $\theta_{\max}$, together with the number of jump phases for the twelve data sets considered here, are given in table 5.3. The experimentally determined values for the contact radius during the n^{th} stick phase, R_n, are taken to be the values of R just before the n^{th} jump phase, and the experimentally determined values for the change in the contact radius during the n^{th} jump phase, δR_n are obtained by calculating the difference between R just before and just after the n^{th} jump phase. The experimentally determined values for the durations of the first stick phase, δt_1, are taken to be the times just before the first jump phase, and the durations of all subsequent stick phases, δt_n $(n > 1)$, are obtained by calculating the difference between t just before the $(n+1)^{\mathrm{th}}$ jump phase and just after the n^{th} jump phase.

Reference	Figure	Substrate	Fluid	Particles	Concentration	Atmosphere
Orejon *et al.* [153]	Fig. 5	CYTOP on silicon	Water	TiO_2	0.1% – 0.01%	Air
	Fig. 6	PTFE on silicon	Water	TiO_2	0.1% – 0.01%	Air
Moffat *et al.* [144]	Fig. 5	PTFE on silicon	Ethanol	TiO_2	0.1%	Nitrogen
Askounis *et al.* [5]	Fig. 1	PTFE on silicon	Ethanol	TiO_2	0.1%	Nitrogen
Askounis *et al.* [6]	Fig. 1	Silicon	Water	SiO_2	0.125%	Air
Askounis *et al.* [7]	Fig. 1	Silicon	Water	SiO_2	0.125%	Air (750 mbar)

Table 5.1: Details of the twelve data sets of experimental results used to validate the model. In the "Particles" column, "TiO_2" denotes titanium oxide and "SiO_2" denotes silicon dioxide. Note that, with the exception of the experiment by Askounis *et al.* [7], which was conducted at an atmospheric pressure of $p_a = 750$ mbar, all experiments were conducted at an atmospheric pressure of $p_a = 1000$ mbar.

	p_a [mbar]	ρ [kg m^{-3}]	D [m^{2}s^{-1}]	c_{sat} [kg m^{-3}]	c_∞ [kg m^{-3}]
water in air	1000	998	$2.46\times10^{-5} \pm 4.92 \times 10^{-6}$	0.0194	0.0058
water in air	750	998	$1.85\times10^{-5} \pm 9.25 \times 10^{-7}$	0.0194	0.0058
ethanol in nitrogen	1000	787	$1.49\times10^{-5} \pm 2.98 \times 10^{-6}$	0.1095	0

Table 5.2: Parameter values characterising the evaporation process of the water and ethanol droplets, where p_a denotes the atmospheric pressure. Note that in the data sets by Askounis *et al.* [6, 7] the humidity is not given: we shall therefore assume that it is 30%, as reported by Orejon *et al.* [153] and Askounis [8]. The value of ρ is taken from Perry *et al.* [163]. The value of D is determined from the formula by Reid *et al.* [173], and the value of c_{sat} is determined from the formula used by Shanahan *et al.* [204]. Note that, according to Reid *et al.* [173], there can be differences of 18% between the calculated values of D and the values determined in experiments, so that the above value of D is given with 20% error bars (see, for example, Sefiane *et al.* [187]).

Reference	Substrate	Concentration	Number of jump phases	θ_0 [rad]	θ_{min} [rad]	θ_{max} [rad]
Orejon *et al.* [153]	CYTOP	0.1%	3	1.91	1.41	1.64
Orejon *et al.* [153]	CYTOP	0.05%	8	1.96	1.57	1.72
Orejon *et al.* [153]	CYTOP	0.025%	10	1.93	1.75	1.83
Orejon *et al.* [153]	CYTOP	0.01%	11	1.88	1.49	1.53
Orejon *et al.* [153]	PTFE	0.1%	7	1.93	1.61	1.75
Orejon *et al.* [153]	PTFE	0.05%	5	1.93	1.60	1.68
Orejon *et al.* [153]	PTFE	0.025%	8	1.91	1.32	1.37
Orejon *et al.* [153]	PTFE	0.01%	4	1.96	1.78	1.82
Moffat *et al.* [144]	PTFE	0.1%	8	0.75	0.68	0.76
Askounis *et al.* [5]	PTFE	0.1%	6	0.70	0.56	0.70
Askounis *et al.* [6]	Silicon	0.125%	4	0.84	0.22	0.33
Askounis *et al.* [7]	Silicon	0.125%	6	0.85	0.37	0.46

Table 5.3: Number of jump phases observed in the experiments, together with the experimentally determined values for the initial contact angle, θ_0, the contact angle at which the contact line de-pins, θ_{min}, the contact angle at which the contact line re-pins, θ_{max}, and the initial contact radius, R_0, for the twelve data sets described in table 5.1.

In all of the twelve data sets considered here the jump phases occur on a much shorter time scale than the stick phases (see section 5.1), validating one of the assumptions of the model.

In order to quantify the extent to which θ_{min} and θ_{max} are constant throughout the entire evaporation process, we compare the experimentally measured values of θ just before and just after every jump phase, $\theta_{\mathrm{min}\,n}$ and $\theta_{\mathrm{max}\,n}$, with the corresponding averaged values, namely θ_{min} and θ_{max}, respectively. This comparison is shown in figure 5.4. In particular, figure 5.4 shows the measured values of $\theta_{\mathrm{min}\,n}$ (grey) and $\theta_{\mathrm{max}\,n}$ (black) and the corresponding averaged values, namely θ_{min} (grey) and θ_{max} (black), respectively, denoted by solid lines, as functions of R_n for the twelve data sets considered here. Note that throughout this chapter a different symbol is used to denote each of the twelve different data sets considered here. For each data set, the smaller the differences are between $\theta_{\mathrm{min}\,n}$ and $\theta_{\mathrm{max}\,n}$ and θ_{min}

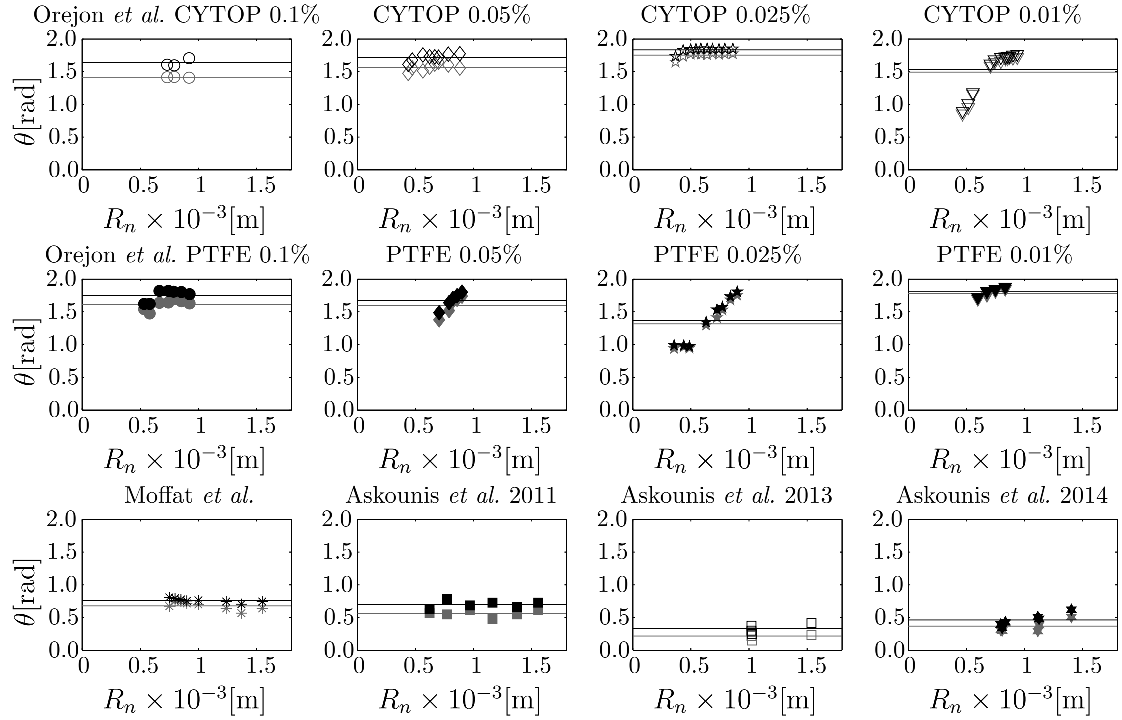

Figure 5.4: Experimentally measured values of θ just before and just after the n^{th} jump phase, $\theta_{\min n}$ (grey) and $\theta_{\max n}$ (black), and the corresponding averaged values, namely $\theta_{\min}$ (grey) and $\theta_{\max}$ (black), respectively, denoted by solid lines, as functions of R_n for the twelve data sets described in table 5.1.

and $\theta_{\max}$, respectively, the better the data set satisfies the assumption that $\theta_{\min}$ and $\theta_{\max}$ are constant throughout the entire evaporation process.

In order to quantify the extent to which R is constant during a stick phase, we consider the maximum absolute change in R (in %) during the n^{th} stick phase, denoted by ΔR_n and given by

$$\Delta R_n = \max \left| \frac{(R_n - R(t)) \times 100}{R_n} \right| \qquad \text{for } t_{n-1} < t < t_n, \tag{5.25}$$

for all twelve sets of experimental data. Figure 5.5 shows the experimentally determined values for ΔR_n, again denoted by a different symbol for each data set, as functions of R_n for the twelve data sets considered here. For each data set, the closer ΔR_n is to zero in figure 5.5, the better the data set satisfies the assumption

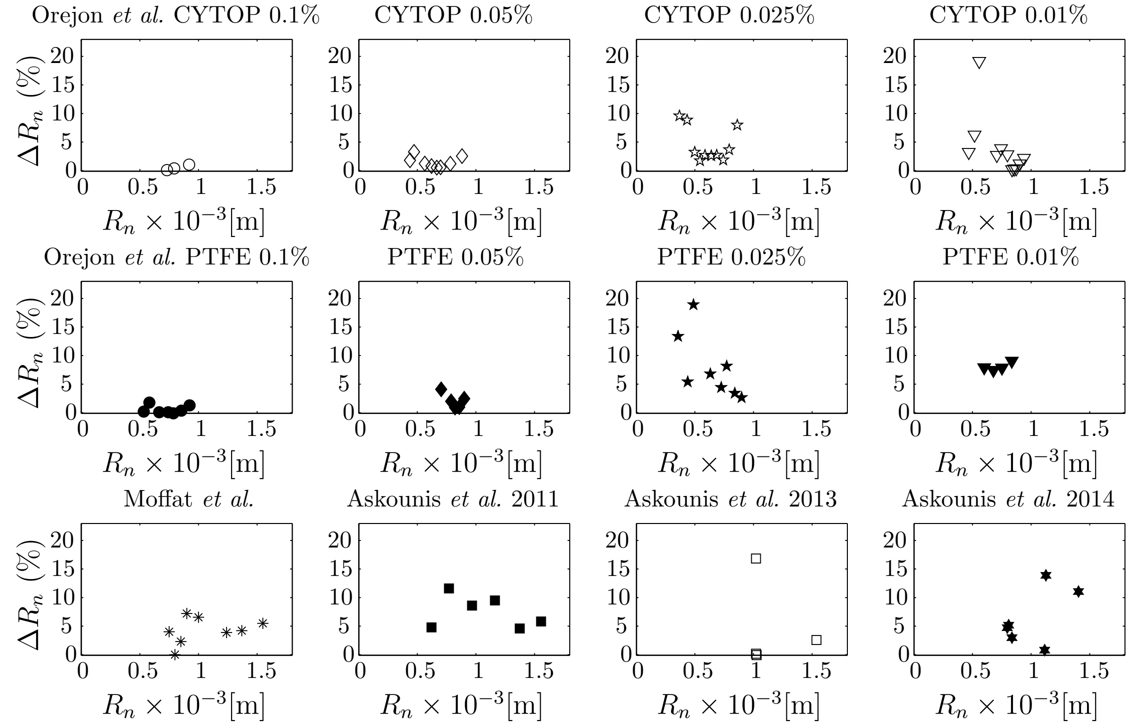

Figure 5.5: Experimentally determined values of the maximum absolute change in R (in %) during the n^{th} stick phase, ΔR_n, given by (5.25), as functions of R_n for the twelve data sets described in table 5.1.

Reference	Substrate	Concentration	ΔR (in %)	$\Delta\theta_{\min}$ (in %)	$\Delta\theta_{\max}$ (in %)
Orejon *et al.* [153]	CYTOP	0.1%	1.0	0.5	4.2
Orejon *et al.* [153]	CYTOP	0.05%	3.3	5.9	6.4
Orejon *et al.* [153]	CYTOP	0.025%	9.6	6.0	5.4
Orejon *et al.* [153]	CYTOP	0.01%	19.2	42.6	41.3
Orejon *et al.* [153]	PTFE	0.1%	1.8	8.5	7.4
Orejon *et al.* [153]	PTFE	0.05%	4.1	13.8	11.2
Orejon *et al.* [153]	PTFE	0.025%	18.9	33.2	32.1
Orejon *et al.* [153]	PTFE	0.01%	9.0	4.8	5.0
Moffat *et al.* [144]	PTFE	0.1%	7.2	16.3	7.5
Askounis *et al.* [5]	PTFE	0.1%	11.6	15.0	11.3
Askounis *et al.* [6]	Silicon	0.125%	16.9	32.4	26.8
Askounis *et al.* [7]	Silicon	0.125%	13.9	37.9	34.0

Table 5.4: Experimentally determined maximum absolute changes in R, $\theta_{\min}$ and $\theta_{\max}$ (in %) namely, ΔR, $\Delta\theta_{\min}$ and $\Delta\theta_{\max}$, given by (5.26)–(5.28), for the twelve data sets described in table 5.1.

that R_n is constant during a stick phase.

In order to summarise and analyse the results shown in figures 5.4 and 5.5, the maximum absolute change in R (in %) for *all* stick phases, ΔR, namely,

$$\Delta R = \max(\Delta R_n), \tag{5.26}$$

and the maximum absolute change in $\theta_{\min}$ and $\theta_{\max}$ (in %) for *all* jump phases, $\Delta\theta_{\min}$ and $\Delta\theta_{\max}$, namely,

$$\Delta\theta_{\min} = \max\left|\frac{(\theta_{\min} - \theta_{\min n}) \times 100}{\theta_{\min}}\right| \tag{5.27}$$

and

$$\Delta\theta_{\max} = \max\left|\frac{(\theta_{\max} - \theta_{\max n}) \times 100}{\theta_{\max}}\right|, \tag{5.28}$$

respectively, are given in table 5.4 for all twelve data sets. Table 5.4 shows that for these data sets ΔR is always smaller than 20%, but that $\Delta\theta_{\min}$ and $\Delta\theta_{\max}$

can be up to 43%. In particular, table 5.4 shows that there are seven data sets, namely Orejon *et al.* [153] (CYTOP 0.1%, 0.05%, 0.025%, and PTFE 0.1%, 0.05%, 0.01%), and Askounis *et al.* [5], for which ΔR, $\Delta\theta_{\mathrm{min}}$ and $\Delta\theta_{\mathrm{max}}$ are all less than 15%, so that for these seven data sets R_n, θ_{min} and θ_{max} can be considered to be approximately constant. In particular, this means for these seven data sets the three assumptions of the model are satisfied very well. However, table 5.4 also shows that for the other five data sets, namely Orejon *et al.* [153] CYTOP 0.01% and PTFE 0.025%, Moffat *et al.* [144], Askounis *et al.* [6, 7], at least one value of ΔR, $\Delta\theta_{\mathrm{min}}$ and $\Delta\theta_{\mathrm{max}}$ is larger than 15%, so that for these five data sets at least one value of R_n, θ_{min} and θ_{max} cannot be considered to be approximately constant. This means for these five data sets one or more of these three assumptions of the model are not satisfied well. We therefore expect that the model will work very well for the seven data sets, but less well for the other five data sets.

An interesting observation can be made regarding figure 5.4: there are four data sets, namely Orejon *et al.* [153] CYTOP 0.01% and PTFE 0.05%, 0.025%, 0.01%, for which as R_n increases, the experimentally measured values for $\theta_{\mathrm{min}\,n}$ and $\theta_{\mathrm{max}\,n}$ also increase, and, more notably, that they increase approximately at the same rate, so that $\delta\theta_n := \theta_{\mathrm{max}\,n} - \theta_{\mathrm{min}\,n}$ is approximately constant. Figure 5.6 shows the experimentally measured values of $\delta\theta_n$ together with $\delta\theta := \theta_{\mathrm{max}} - \theta_{\mathrm{min}}$ calculated using the experimentally determined values θ_{min} and θ_{max} as given in table 5.3, denoted by solid lines, as a function of R_n for the twelve data sets considered here. Note that it would be natural to assume that $\delta\theta_n$ is a good quantity to test whether the assumptions of the model, namely that θ_{min} and θ_{max} are constant for the entire evaporation process, are satisfied. However, this is not the case, since, as we have already mentioned, as R_n increases, $\theta_{\mathrm{min}\,n}$ and $\theta_{\mathrm{max}\,n}$ may increase at the same rate, so that $\delta\theta_n$ is approximately constant, even though $\theta_{\mathrm{min}\,n}$ and $\theta_{\mathrm{max}\,n}$

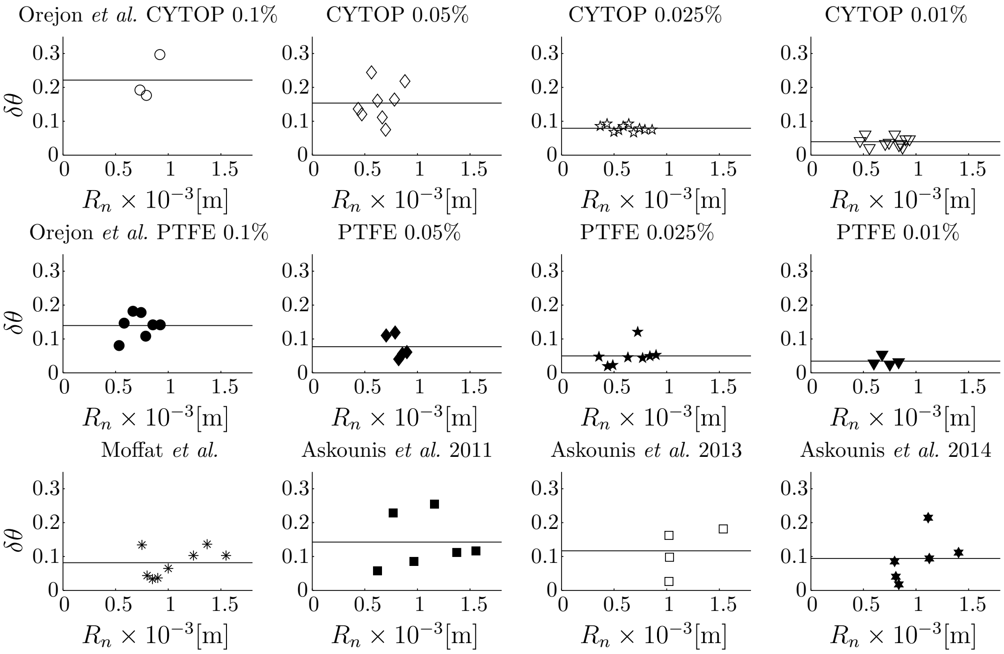

Figure 5.6: Experimentally measured values of $\delta\theta_n := \theta_{\max n} - \theta_{\min n}$ together with $\delta\theta := \theta_{\max} - \theta_{\min}$ calculated using the experimentally determined values of $\theta_{\min}$ and $\theta_{\max}$ as given in table 5.3, denoted by solid lines, as functions of R_n for the twelve data sets described in table 5.1.

themselves are *not* approximately constant (see, Orejon *et al.* [153] CYTOP 0.01% and PTFE 0.025%). Figure 5.6 indicates that for the present twelve data sets $\delta\theta$ is approximately constant, so that at least for these data sets $\delta R_n \propto R_n$ (see equation (5.4)) describes the relationship between δR_n and R_n more accurately than $\delta R_n \propto \sqrt{R_n}$ derived by Shanahan [201].

Thus we have shown that for seven data sets the assumptions of the model are satisfied very well, but that at least one of them is not satisfied very well for the other five data sets. In the following section, we compare the theoretical predictions of the present model for both the change in the contact radius during a jump phase and the duration of the stick phase with experimentally measured values from all twelve data sets.

5.7 Comparisons between the Theoretical Predictions of the Model and Experimental Results

As mentioned previously, for droplets with suspended particles the pinning, de-pinning and re-pinning of the contact line is influenced by the deposition of particles. Since the suspended particles are never deposited in exactly the same way in different experiments, the pinning, de-pinning and re-pinning of the contact line is never exactly the same in different experiments, *i.e.* there is always some stochastic variation in the experimental results. We shall show in this section that although the present model does not capture this variation, it is nevertheless able to predict the experimental data quantitatively. As the present model predicts an infinite number of stick phases (see section 5.2), which, of course, is not possible in practice, we shall test whether it is able to predict the evolution of R and θ (and hence V) during the finite number of stick and jump phases observed in experiments. In particular, we compare the experimentally determined values of the change in the contact radius during the n^{th} jump phase, δR_n, and the duration of the n^{th} stick phase, δt_n, as functions of the contact radius during the n^{th} stick phase, R_n, as given by (5.4), (5.7) and (5.10), using the values of Λ, k_0, and k given in table 5.5 calculated from equations (5.2), (5.8) and (5.11), respectively, with the theoretically predicted values. The results of this comparison have the advantage over the results of the comparison between the theoretically predicted and experimentally determined values of $R(t)$ and $\theta(t)$ that the accumulation of errors is reduced.

Reference	Substrate	Concentration	Λ	k_0 [s m^{-2}]	k [s m^{-2}]
Orejon *et al.* [153]	CYTOP	0.1%	0.90	9.00×10^8	3.24×10^8
Orejon *et al.* [153]	CYTOP	0.05%	0.92	8.32×10^8	2.53×10^8
Orejon *et al.* [153]	CYTOP	0.025%	0.96	4.32×10^8	1.73×10^8
Orejon *et al.* [153]	CYTOP	0.01%	0.98	7.20×10^8	5.47×10^7
Orejon *et al.* [153]	PTFE	0.1%	0.93	7.70×10^8	4.00×10^8
Orejon *et al.* [153]	PTFE	0.05%	0.96	6.97×10^8	1.28×10^8
Orejon *et al.* [153]	PTFE	0.025%	0.98	1.00×10^9	5.53×10^7
Orejon *et al.* [153]	PTFE	0.01%	0.98	4.59×10^8	8.81×10^7
Moffat *et al.* [144]	PTFE	0.1%	0.96	7.45×10^6	8.54×10^6
Askounis *et al.* [5]	PTFE	0.1%	0.92	1.44×10^7	1.44×10^7
Askounis *et al.* [6]	Silicon	0.125%	0.83	3.85×10^8	6.39×10^7
Askounis *et al.* [7]	Silicon	0.125%	0.92	4.07×10^8	7.12×10^7

Table 5.5: Values of Λ, k_0 and k calculated from equations (5.2), (5.8), and (5.11), respectively, using the experimentally determined values of θ_0, $\theta_{\min}$ and $\theta_{\max}$ described in table 5.3 for the twelve data sets described in table 5.1.

5.7.1 The Change in the Contact Radius During a Jump Phase

Figure 5.7 (a) shows the theoretically predicted change in the contact radius during the n^{th} jump phase, δR_n, as given in equation (5.4) using the values of Λ given in table 5.5, denoted by a solid line, as well as the experimentally determined values for δR_n as functions of the contact radius during the n^{th} stick phase, R_n, for all twelve data sets. Note that a small number of the experimentally determined values of δR_n obtained by Askounis *et al.* [6, 7] are actually *negative*, which means that the contact radius during the $(n+1)^{\text{th}}$ stick phase, R_{n+1}, is actually *larger* than the contact radius during the previous n^{th} stick phase, R_n. This behaviour cannot, of course, be captured by the present model.

Figure 5.7 (b) shows $\delta R_n/(1-\Lambda)$ as a function of R_n for the seven data sets which satisfy the assumptions of the model well (see table 5.4), namely Orejon *et al.* [153] (CYTOP 0.1%, 0.05%, 0.025%, and PTFE 0.1%, 0.05%, 0.01%), and

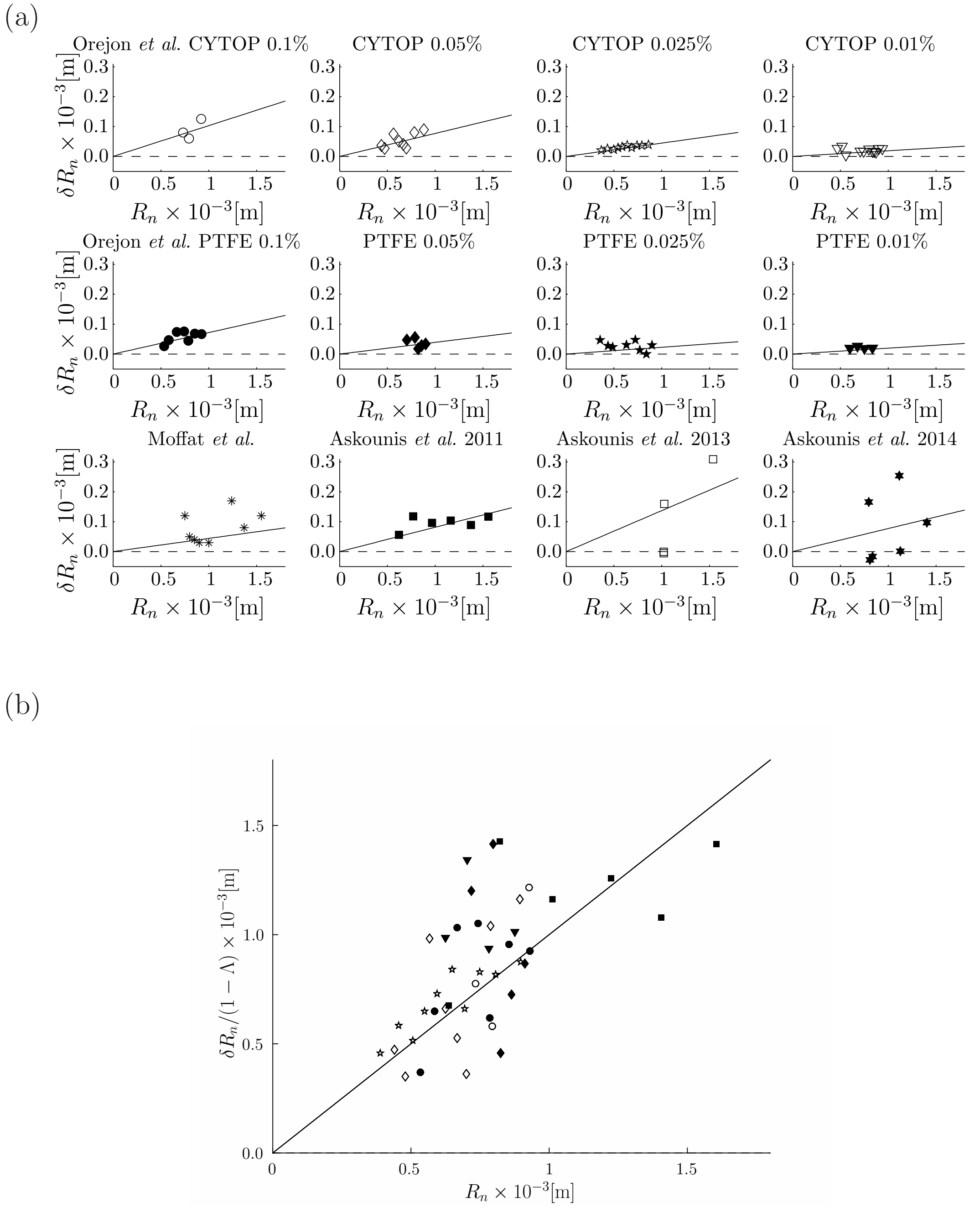

Figure 5.7: Part (a) shows the theoretically predicted change in the contact radius during the n^{th} jump phase, δR_n, denoted by solid lines, as given in equation (5.4) and the experimentally determined values as a function of the contact radius during the n^{th} stick phase, R_n, for all twelve data sets described in table 5.1. The dashed line denotes the axis $\delta R_n = 0$. Part (b) shows $\delta R_n/(1-\Lambda)$ for the seven data sets which satisfy the assumptions of the model well (see table 5.4), so that for these data sets the theoretically predicted values collapse onto the single straight line $\delta R_n/(1-\Lambda) = \delta R_n$. Note that the same symbols are used for each data set in both parts of the figure.

Askounis *et al.* [5]. This means that the theoretically predicted values collapse onto the single straight line $\delta R_n/(1-\Lambda) = R_n$, and comparisons between the seven data sets can therefore be made readily.

Figure 5.7 shows that, despite the stochastic variation in the experimental results, the agreement between the theoretical predictions for δR_n and the experimentally determined values is reasonably good for all twelve data sets. In particular, figure 5.7 (b) shows that the model quantitatively predicts δR_n for the seven data sets which satisfy the assumptions of the model well, since the points representing the experimentally determined values are clustered closely around the straight line representing the theoretical predictions.

Thus having compared the theoretically predicted values for δR_n with the experimentally determined values, the next subsection focuses on the comparison between the theoretically predicted duration of the stick phase and the experimentally determined values.

5.7.2 The Duration of a Stick Phase

As described previously, in the present model the first stick phase is qualitatively different from all of the other subsequent stick phases (see equations (5.7) and (5.10)). Therefore, in order to compare the theoretically predicted durations of all of the stick phases, *i.e.* δt_n for any $n \geq 1$, with the experimentally determined values, we scale the duration of the first stick phase by k_0 and the durations of all of the subsequent stick phases by k, given by equations (5.8) and (5.11), respectively.

Figure 5.8 shows $\delta t_1/k_0$ and $\delta t_n/k$ (for $n > 1$), denoted by solid lines, as given in equations (5.7) and (5.10) using the values for k_0 and k as given in table 5.5, respectively, and the experimental determined values as functions of R_n, for all twelve data sets considered here. In particular, figure 5.8 (a) shows that, with the

(a)

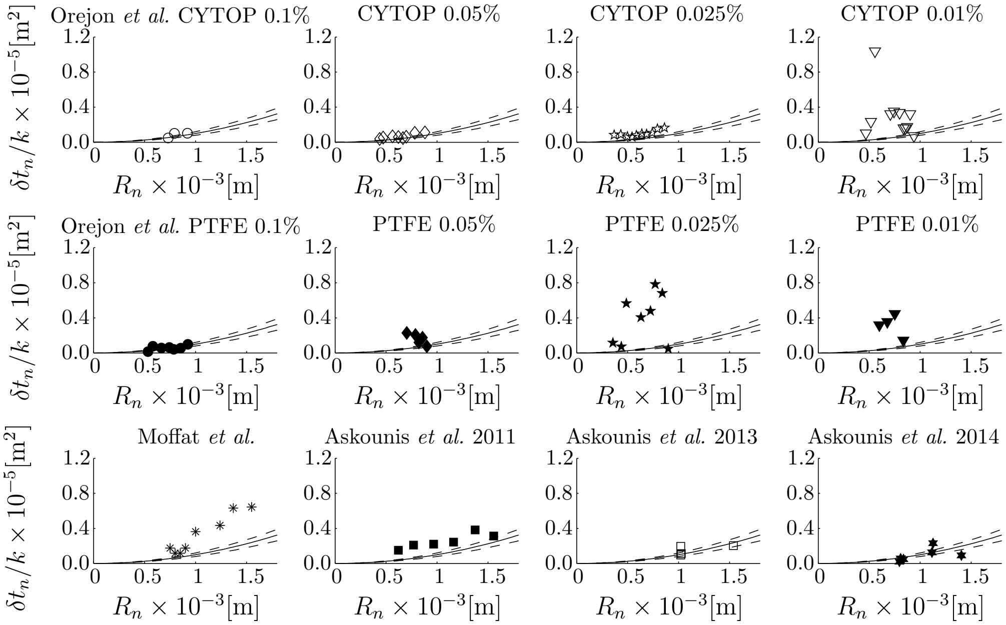

(b)

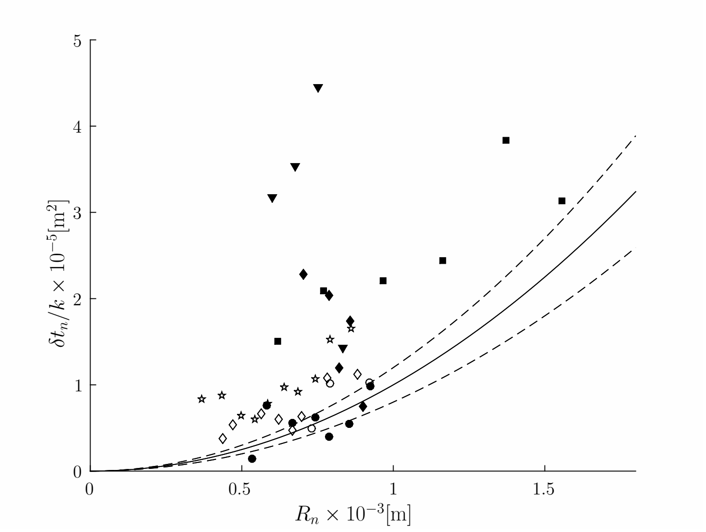

Figure 5.8: Part (a) shows the scaled theoretically predicted duration of the n^{th} stick phase, namely $\delta t_1/k_0$ and $\delta t_n/k$ (for $n > 1$), denoted by solid lines, as given in equations (5.7) and (5.10), respectively, and the experimental determined values for $\delta t_1/k_0$ and $\delta t_n/k$ as functions of R_n, for all twelve data sets described in table 5.1. The dashed lines represent a $\pm 20\%$ change in the value of D. Part (b) shows the results of part (a) for the seven data sets which satisfy the assumptions of the model well (see table 5.4) in a single figure. Note that the same symbols are used for each data set in both parts of the figure.

exception of the data set by Moffat *et al.* [144], since the data points with the largest values of R_n are always very close to the predicted curves for all these data sets, the model predicts the experimentally determined duration of the first stick phase represented by the largest value of R_n very well.

Figure 5.8 shows that, despite the stochastic variation in the experimental results, the agreement between the theoretical predictions for δt_n and the experimentally determined values is also reasonably good for all twelve data sets. In particular, figure 5.8 (b) shows that the present model quantitatively predicts δt_n for the seven data sets which satisfy the assumptions of the model well. Thus the experimentally determined values of *both* δt_n and δR_n, and therefore the evolution of R and θ, are predicted very well only for the seven data sets for which all three assumptions of the model are satisfied.

Since, according to Reid *et al.* [173], there can be differences of 18% between the calculated values and the experimentally determined values of D, it is the least certain value of the parameters in table 5.2, and so the effect of a ±20% change in D (see, for example, Sefiane *et al.* [187]) is denoted by the dashed lines in figure 5.8. However, this change in D does not significantly improve the agreement between the model predictions and the experimental data.

5.8 Summary

In this chapter a simple model for a droplet evaporating in the SJ mode, which does not attempt to resolve the details of the local behaviour near the contact line but captures the global behaviour of the droplet, was developed and used to give a complete description the evolution of R and θ, and hence V, and, in particular, the duration of the n^{th} stick phase, δt_n, and the time at which the n^{th} stick phase ends,

t_n. It was also shown that in appropriate special cases the present model reduces to simpler models for previously discussed simpler modes of evaporation. Finally, by comparing the theoretical predictions of the present model with experimental results, it was shown that the present model is quantitatively able to predict the experimental data, which satisfy the assumptions of the model well.

Chapter 6

The Lifetimes of Droplets in the Stick-Jump Mode

In this chapter we use the model for a droplet evaporating in the SJ mode described in the previous chapter to predict its lifetime. In particular, in section 6.1 we describe the theoretical predictions for the lifetimes of droplets in the SJ mode, which we compare in section 6.2 to the lifetimes determined from the experiments discussed in the previous chapter. In section 6.3 the relationship between the lifetimes of droplets in the SJ mode and those of initially identical droplets evaporating in the two extreme modes is described. In particular, we shall show that there is a region in the parameter space in which the lifetime of droplets in the SJ mode is shorter than the lifetimes of droplets evaporating in the extreme modes. Furthermore, it will be shown that in appropriate special cases the lifetimes of droplets in the SJ mode reduce to the lifetimes of droplets in previously discussed simpler modes of evaporation. Finally, in section 6.4 simple approximations for the lifetimes of droplets in the SJ mode are suggested and compared with the theoretical predictions for the lifetimes of droplets in the SJ mode as well as with experimentally determined lifetimes.

6.1 Theoretical Predictions for the Lifetimes of Droplets in the Stick-Jump Mode

As we have described in section 5.2, the present model for the SJ mode predicts that the droplet evaporates completely in a finite time after an infinite number of stick and jump phases. Letting $n \to \infty$ in the expression for the time at which the n^{th} stick phase ends, given by (5.14), and scaling time with $\mathcal{T}$ given in equation (2.9), as in previous chapters, we find that the lifetime of a droplet in the SJ mode, denoted by $t_{\mathrm{SJ}} = t_{\mathrm{SJ}}(\theta_0, \theta_{\min}, \theta_{\max})$, is given by

$$t_{\mathrm{SJ}} = \left(\frac{2(1+\cos\theta_0)^2}{\sin\theta_0(\cos\theta_0+2)}\right)^{2/3} \left[\int_{\theta_{\max}}^{\theta_0} \frac{2\,\mathrm{d}\theta}{g(\theta)} + \frac{1}{1-\Lambda^2}\int_{\theta_{\min}}^{\theta_{\max}} \frac{2\,\mathrm{d}\theta}{g(\theta)}\right], \tag{6.1}$$

or, equivalently,

$$t_{\mathrm{SJ}} = \left(\frac{2(1+\cos\theta_0)^2}{\sin\theta_0(\cos\theta_0+2)}\right)^{2/3} \left[\int_{\theta_{\min}}^{\theta_0} \frac{2\,\mathrm{d}\theta}{g(\theta)} + \frac{\Lambda^2}{1-\Lambda^2}\int_{\theta_{\min}}^{\theta_{\max}} \frac{2\,\mathrm{d}\theta}{g(\theta)}\right], \tag{6.2}$$

where the first term on the right-hand side of (6.2) represents the duration of the first stick phase and the second term represents the duration of all of the subsequent stick phases. (The jump phases are all instantaneous and so, of course, do not contribute directly to the right-hand side of (6.2).)

6.2 Experimental Validation of the Model

By comparing the finite number of stick and jump phases observed in experiments with the corresponding finite number of the theoretically infinite number of stick and jump phases predicted by the present model, it has been shown in section 5.7 that the present model is able to predict the experimental data for change in the contact radius, δR_n, during the n^{th} jump phase and the duration of the n^{th} stick phase, δt_n, reasonably well. It is, however, *not* clear if the present model is able to predict the lifetime of a droplet in the SJ mode accurately, since this aspect of the model was not tested in the previous chapter. This will be done in this section by comparing the predictions of the model with results of the experiments discussed in the previous chapter.

We use the twelve data sets for droplets evaporating in the SJ mode obtained by Moffat *et al.* [144], Askounis *et al.* [5, 6, 7], and Orejon *et al.* [153] discussed in the previous chapter. Details of these data sets can be found in tables 5.1–5.5. In particular, tables 5.3 and 5.5 show that for all of the data sets except for that of Askounis *et al.* [6], the values for θ_{min} and θ_{max} are fairly similar and hence the values for Λ are fairly close to 1. Furthermore, table 5.3 shows that the $\max(\theta_0, \theta_{\mathrm{max}})/\theta_{\mathrm{min}} \gtrsim 0.7$ for the data sets by Moffat *et al.* [144], Askounis *et al.* [5], and Orejon *et al.* [153], but that $\max(\theta_0, \theta_{\mathrm{max}})/\theta_{\mathrm{min}} \simeq 0.3$ and 0.4 for the two data sets by Askounis *et al.* [6, 7], respectively. These approximated values show that, with the exception of the latter two data sets, the values of θ_0, θ_{min} and θ_{max} are all fairly similar, so that for these data sets the SJ mode is very similar the CA mode (recall that in the special case $\theta_0 = \theta_{\mathrm{min}} = \theta_{\mathrm{max}}$ the SJ mode reduces to the CA mode, see section 5.4); therefore comparison with experimental results in these cases is essentially a validation for the lifetime of a droplet in the CA mode. Moreover, as already noted, for the two data sets of Askounis *et al.* [6, 7] two of the three assumptions of the model, namely that θ_{min} and θ_{max} are constant throughout the entire evaporation process and that R remains constant during a stick phase, are not satisfied very well. Thus further experiments with small

Reference	Substrate	Concentration	t_{SJ}	t_{exp}	Error (in %)
Orejon *et al.* [153]	CYTOP	0.1%	0.9983	0.9878	−1.06
Orejon *et al.* [153]	CYTOP	0.05%	0.9976	0.9836	−1.42
Orejon *et al.* [153]	CYTOP	0.025%	0.9950	0.9860	−0.91
Orejon *et al.* [153]	CYTOP	0.01%	0.9987	0.9909	−0.79
Orejon *et al.* [153]	PTFE	0.1%	0.9975	0.9834	−1.43
Orejon *et al.* [153]	PTFE	0.05%	0.9981	0.9844	−1.39
Orejon *et al.* [153]	PTFE	0.025%	0.9955	0.9809	−1.49
Orejon *et al.* [153]	PTFE	0.01%	0.9944	0.9810	−1.37
Moffat *et al.* [144]	PTFE	0.1%	0.9042	0.8912	−1.46
Askounis *et al.* [5]	PTFE	0.1%	0.8776	0.9035	2.87
Askounis *et al.* [6]	Silicon	0.125%	0.7789	0.9429	17.39
Askounis *et al.* [7]	Silicon	0.125%	0.8250	0.9437	12.58

Table 6.1: The theoretically predicted lifetimes of evaporating droplets, t_{SJ}, calculated numerically from (6.2) using the experimentally determined values for θ_0, θ_{min} and θ_{max} given in table 5.3 together with the experimentally determined values, t_{exp}, and the percentage error between those two values (calculated from $(t_{\mathrm{exp}} - t_{\mathrm{SJ}}) \times 100/t_{\mathrm{exp}}$) for the twelve data sets described in table 5.1.

values of $\max(\theta_0, \theta_{\mathrm{max}})/\theta_{\mathrm{min}}$ which satisfy the assumptions of the model better are required to give a more convincing validation for the lifetime as predicted by the present model. In the absence of such experiments we shall continue to consider all twelve data sets in the present chapter.

For each of the twelve data sets described in table 5.1 the experimentally determined lifetime of the droplet, t_{exp}, was obtained by fitting $V^{2/3}$ as a linear function of t and extrapolating to $V = 0$ as described in section 3.3. In table 6.1 and figure 6.1 we compare t_{SJ} calculated numerically from (6.2) using the experimentally determined values for θ_0, θ_{min} and θ_{max} with t_{exp}. In particular, table 6.1 and figure 6.1 show that, with the exception of the two data sets by Askounis *et al.* [6, 7], the agreement between the experimentally determined lifetimes and the theoretically predicted lifetimes is excellent, with percentage errors smaller than 3%. However, for these two data sets the model under-predicts the experimentally determined lifetimes by approximately 17% and 13%, respectively. As mentioned previously,

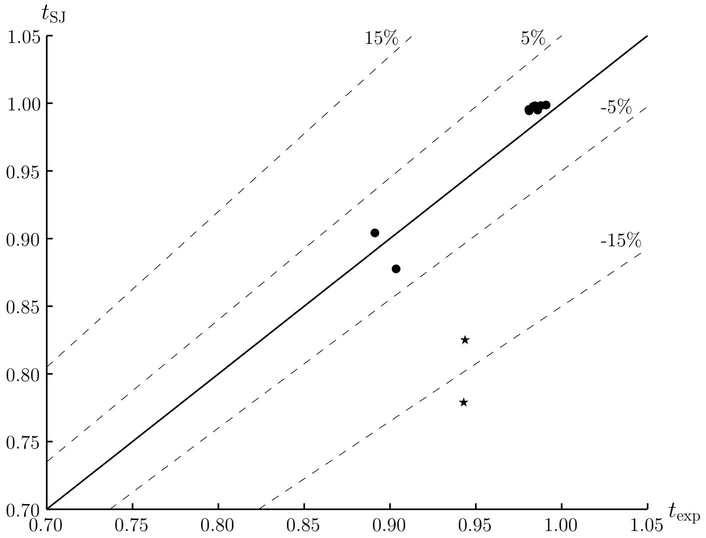

Figure 6.1: The theoretically predicted lifetimes of evaporating droplets, t_{SJ}, calculated numerically from (6.2) using the experimentally determined values of θ_0, θ_{min} and θ_{max}, plotted as a function of the corresponding experimentally determined values, t_{exp}, together with a solid line showing $t_{\mathrm{SJ}} = t_{\mathrm{exp}}$ and dashed lines showing 5% and 15% deviations from $t_{\mathrm{SJ}} = t_{\mathrm{exp}}$. The values from the two experiments by Askounis *et al.* [6, 7] are denoted by stars (★) rather than by dots (●); note, that these two data sets have the largest errors, namely 17% and 13%, respectively.

these two data sets do not satisfy the assumptions of the model very well, and so it is perhaps surprising that the error is not larger. Note that the present errors are of the same order of magnitude as the errors reported by Dietrich *et al.* [56], who found a maximum error of 20% between the predicted and the experimentally determined lifetimes for dissolving droplets. These results show that the model predicts the experimentally determined lifetimes well. Thus we shall analyse the lifetimes of droplets in the SJ mode, and the relationship between them and the lifetimes of initially identical droplets evaporating in the extreme modes in greater detail in the next section.

6.3 Analysis of the Lifetimes of Droplets in the Stick-Jump Mode

The lifetimes of droplets in the extreme (CR and CA) modes, given by (2.10) and (2.11), are, as we have shown in section 2.1, by definition dependent only on θ_0, whereas the lifetimes of droplets in the SJ mode given by (6.2) are dependent on $\theta_{\rm min}$ and $\theta_{\rm max}$ as well as θ_0. In order to compare the lifetimes of droplets in the two extreme modes with the lifetime of droplets in the SJ mode, we shall plot them *all* as functions of θ_0.

In order to describe how different values of $\theta_{\rm min}$ and $\theta_{\rm max}$ affect $t_{\rm SJ}$ given by (6.2), we consider the $\theta_{\rm min}$–$\theta_{\rm max}$ parameter plane, shown in figure 6.2 (a). Note that, since by definition $\theta_{\rm min} \leq \theta_{\rm max}$, only the upper triangle of the $\theta_{\rm min}$–$\theta_{\rm max}$ parameter plane is physically realisable. This upper triangle is divided into the three regions **A**, **C**, and **E**, which are separated by the two curves **B** and **D**, corresponding to different orderings of $t_{\rm CR}$, $t_{\rm CA}$ and $t_{\rm SJ}$ at $\theta_0 = \theta_{\rm min}$. Specifically, for values of $\theta_{\rm min}$ and $\theta_{\rm max}$ in region **A** $t_{\rm CR} < t_{\rm CA} < t_{\rm SJ}$ at $\theta_0 = \theta_{\rm min}$, on curve **B** $t_{\rm CR} < t_{\rm CA} = t_{\rm SJ}$ at $\theta_0 = \theta_{\rm min}$, in region **C** $t_{\rm CR} < t_{\rm SJ} < t_{\rm CA}$ at $\theta_0 = \theta_{\rm min}$, on curve **D** $t_{\rm CR} = t_{\rm SJ} < t_{\rm CA}$ at $\theta_0 = \theta_{\rm min}$, and in region **E** $t_{\rm SJ} < \min(t_{\rm CR}, t_{\rm CA})$ at $\theta_0 = \theta_{\rm min}$. Three examples of transects through the $\theta_{\rm min}$–$\theta_{\rm max}$ parameter plane, namely $\theta_{\rm min} = \pi/16$, $\theta_{\rm max} = \theta_{\rm min} + \pi/4$, and $\theta_{\rm max} = 7\pi/8$, are given in figure 6.2 (a) and example values of $\theta_{\rm min}$ and $\theta_{\rm max}$ on these transects corresponding to the points $\mathcal{A}$–$\mathcal{R}$ are indicated. Specifically, on the first transect $\theta_{\rm min}$ is constant but $\theta_{\rm max}$ varies, namely $\theta_{\rm min} = \pi/16$ (example values of $\theta_{\rm min}$ and $\theta_{\rm max}$ on this transect are denoted by $\mathcal{A}$–$\mathcal{G}$), on the second transect both $\theta_{\rm min}$ and $\theta_{\rm max}$ vary, namely $\theta_{\rm max} = \theta_{\rm min} + \pi/4$ (example values of $\theta_{\rm min}$ and $\theta_{\rm max}$ on this transect are denoted by $\mathcal{H}$–$\mathcal{M}$), and on the third transect $\theta_{\rm min}$ varies but $\theta_{\rm max}$ is constant, namely

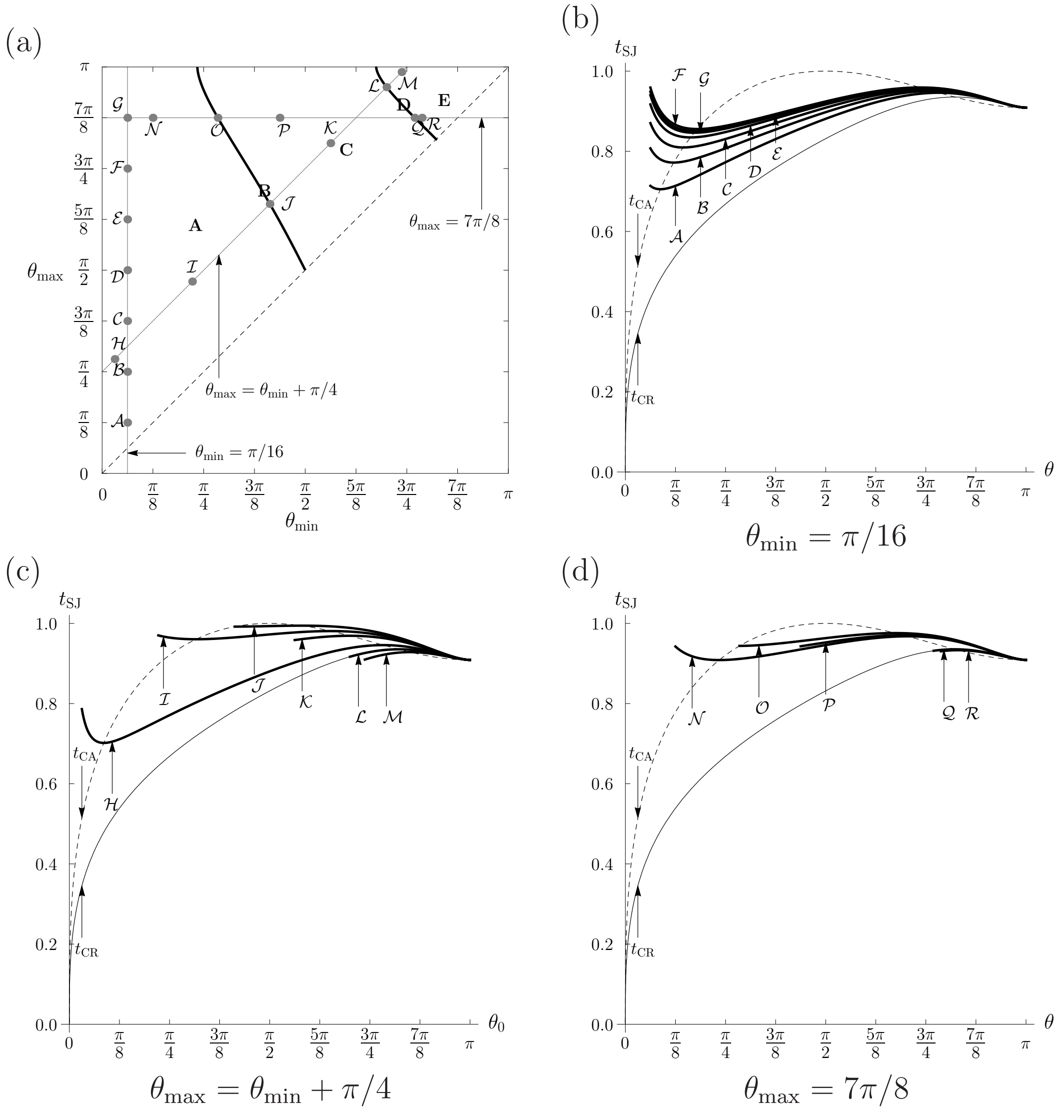

$\theta_{\min} = \pi/16$

$\theta_{\max} = \theta_{\min} + \pi/4$

$\theta_{\max} = 7\pi/8$

Figure 6.2: Part (a) shows how the $\theta_{\min}$–$\theta_{\max}$ parameter plane is divided into the three regions **A**, **C**, and **E**, which are separated by the two curves **B** and **D**, according to the ordering of t_{CR}, t_{CA} and t_{SJ} at $\theta_0 = \theta_{\min}$. Specifically, for values of $\theta_{\min}$ and $\theta_{\max}$ in region **A** $t_{\mathrm{CR}} < t_{\mathrm{CA}} < t_{\mathrm{SJ}}$ at $\theta_0 = \theta_{\min}$, on curve **B** $t_{\mathrm{CR}} < t_{\mathrm{CA}} = t_{\mathrm{SJ}}$ at $\theta_0 = \theta_{\min}$, in region **C** $t_{\mathrm{CR}} < t_{\mathrm{SJ}} < t_{\mathrm{CA}}$ at $\theta_0 = \theta_{\min}$, on curve **D** $t_{\mathrm{CR}} = t_{\mathrm{SJ}} < t_{\mathrm{CA}}$ at $\theta_0 = \theta_{\min}$, and in region **E** $t_{\mathrm{SJ}} < \min(t_{\mathrm{CR}}, t_{\mathrm{CA}})$ at $\theta_0 = \theta_{\min}$. Note that, since by definition $\theta_{\min} \leq \theta_{\max}$, only the upper triangle of the $\theta_{\min}$–$\theta_{\max}$ parameter plane is physically realisable. Parts (b)–(d) give examples of plots of the lifetimes of droplets in the SJ mode, t_{SJ}, as a function of θ_0 given in equation (6.2) given by the thick solid line for example values of $\theta_{\min}$ and $\theta_{\max}$, denoted by $\mathcal{A}$–$\mathcal{R}$, that are obtained by three different transects through the $\theta_{\min}$–$\theta_{\max}$ parameter plane, namely $\theta_{\min} = \pi/16$, $\theta_{\max} = \theta_{\min} + \pi/4$, and $\theta_{\max} = 7\pi/8$ together with the lifetimes of droplets in the two extreme modes, t_{CR} and t_{CA} as functions of θ_0 given in equations (2.10) and (2.11) and given by the solid and the dashed line, respectively.

$\theta_{\max} = 7\pi/8$ (example values of $\theta_{\min}$ and $\theta_{\max}$ on this transect are denoted by $\mathcal{N}$–$\mathcal{R}$). These example values of $\theta_{\min}$ and $\theta_{\max}$ ($\mathcal{A}$–$\mathcal{R}$) are used to plot the lifetimes of a droplet in the SJ mode, t_{SJ}, as given in equation (6.2), together with the lifetimes of droplets in the two extreme modes, t_{CR} and t_{CA}, as given in equations (2.10) and (2.11), respectively, as functions of θ_0 in figure 6.2 (b)–(d). For each curve shown in figure 6.2 (b)–(d), since $\theta_{\min} \leq \theta_0$, t_{SJ} is defined only for θ_0 in the range $\theta_{\min} \leq \theta_0 \leq \pi$. This is different from the lifetimes of droplets in the extreme modes or the lifetimes of droplet in the SS mode described in Chapters 2–4, which are defined for all values of θ_0 in the range $0 \leq \theta_0 \leq \pi$. Figure 6.2 (b)–(d) also show that $t_{\mathrm{SJ}} = t_{\mathrm{CR}} = t_{\mathrm{CA}} = t_{\pi}$, given by (2.12), for $\theta_0 = \pi$, irrespective of the values of $\theta_{\min}$ and $\theta_{\max}$, and that in the limit $\theta_0 \to \pi^-$ the curve representing t_{SJ} approaches t_{π} from above with zero slope, just like the curve representing t_{CR}, given in equation (2.13). However, in general, the curve representing t_{SJ} is fairly complicated and, especially for large contact angles, the t_{SJ} curves become difficult to distinguish in figure 6.2 (b)–(d). Therefore, in order to illustrate the behaviour of the t_{SJ} curves more clearly, figure 6.3 (b)–(f) show sketches of typical t_{SJ} curves corresponding to values of $\theta_{\min}$ and $\theta_{\max}$ in the regions/on the curves **A**–**E** in figure 6.2 (a), which is re-drawn for clarity in figure 6.3 (a) without the transects, together with sketches of the t_{CR} and t_{CA} curves.

Figure 6.3 (b) shows that for values of $\theta_{\min}$ and $\theta_{\max}$ in region **A** in figure 6.3 (a), the t_{SJ} curve has a local minimum at $\theta_0 = \theta_{0,\min}$ (with $\theta_{\min} < \theta_{0,\min} < \pi/2$) when $t_{\mathrm{SJ}} = t_{\mathrm{CA}}$, and a local maximum at $\theta_0 = \theta_{0,\max}$ (with $\pi/2 < \theta_{0,\max} < \pi$) when $t_{\mathrm{SJ}} = t_{\mathrm{CA}}$. Note that whereas the local maximum at $\theta_0 = \theta_{0,\max}$ is always a global maximum, depending on the values of $\theta_{\min}$ and $\theta_{\max}$, the local minimum at $\theta_0 = \theta_{0,\min}$ may be a global minimum. In particular, if $t_{\mathrm{SJ}} < t_{\pi}$ at $\theta_0 = \theta_{0,\min}$ then the t_{SJ} curve has a global minimum at $\theta_0 = \theta_{0,\min}$, and if $t_{\mathrm{SJ}} > t_{\pi}$ at $\theta_0 = \theta_{0,\min}$

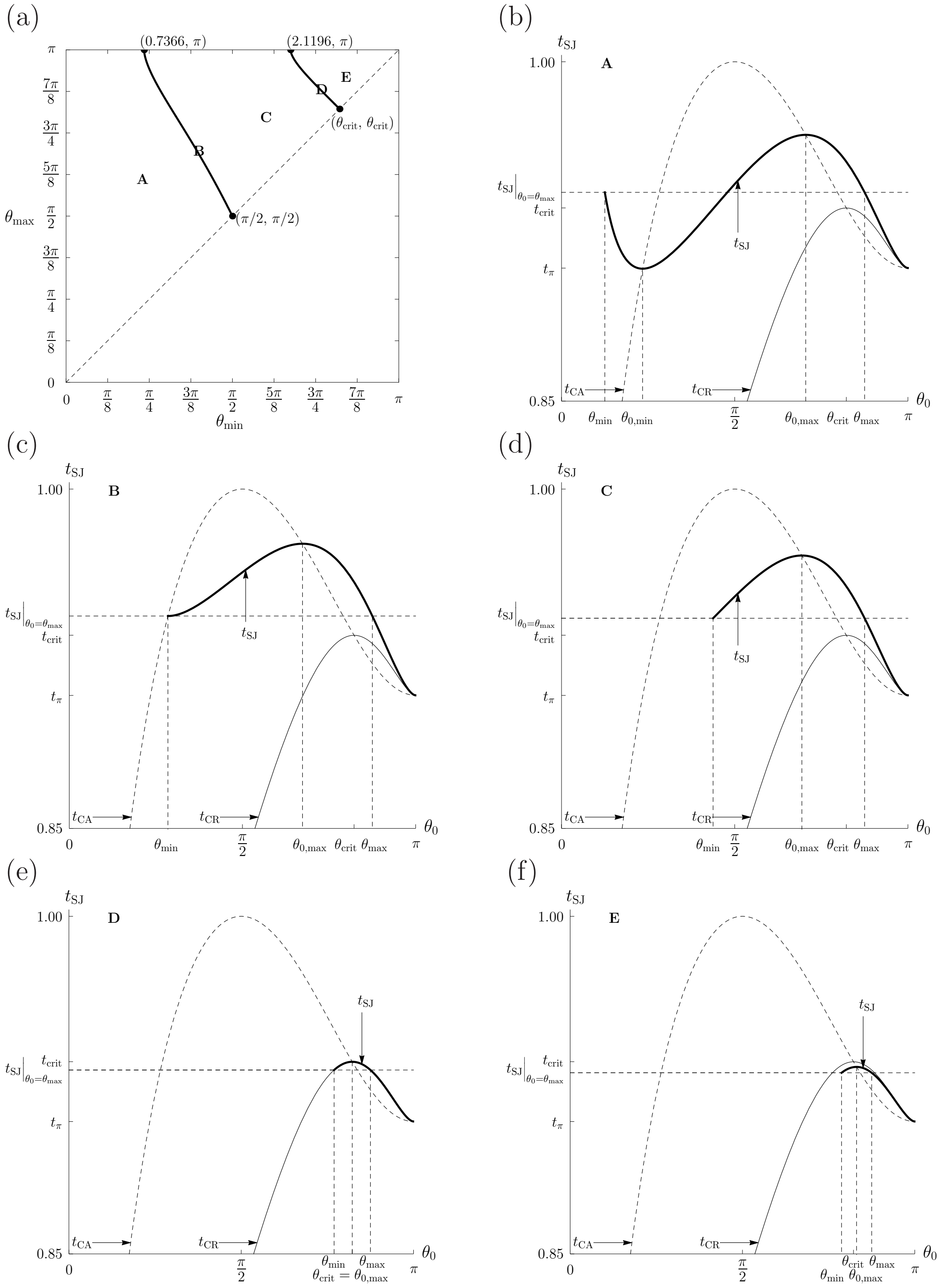

Figure 6.3: Part (a) is the same as figure 6.2 (a) but without the transects. Parts (b)–(f) shows sketches of typical lifetimes of a droplet in the SJ mode, t_{SJ}, as a function of θ_0 for different values of θ_{min} and θ_{max} in the regions/on the curves **A**–**E**, respectively, shown in part (a), together with sketches of the lifetimes of droplets in the two extreme modes, t_{CR} and t_{CA}, as functions of θ_0.

then the t_{SJ} curve has a global minimum at $\theta_0 = \pi$.

Figure 6.3 (c) shows that for values of θ_{min} and θ_{max} on the curve **B** in figure 6.3 (a) the t_{SJ} curve departs from the t_{CA} curve with zero slope at $\theta_0 = \theta_{\mathrm{min}} = \theta_{0,\mathrm{min}}$, so that for values of θ_{min} and θ_{max} in the regions/on the curves **B**–**E** the local minimum at $\theta_0 = \theta_{0,\mathrm{min}}$ disappears and the t_{SJ} curve always has only a global minimum at $\theta_0 = \pi$ and a global maximum at $\theta_0 = \theta_{0,\mathrm{max}}$.

Figure 6.3 (b)–(f) show that the position of the t_{SJ} curve with respect to that of the t_{CR} curve changes. Whereas for values of θ_{min} and θ_{max} in the regions/on the curves **A**–**C** we have $t_{\mathrm{SJ}} \geq t_{\mathrm{CR}}$ for $\theta_{\mathrm{min}} \leq \theta_0 \leq \pi$, *i.e.* the lifetime of a droplet in the SJ mode is larger than the lifetime of a droplet in the CR mode (see figure 6.3 (b)–(d)), for values of θ_{min} and θ_{max} in region **E** we have $t_{\mathrm{SJ}} \leq t_{\mathrm{CR}}$ for $\theta_{\mathrm{min}} \leq \theta_0 \leq \pi$, *i.e.* the lifetime of a droplet in the SJ mode is smaller than the lifetime of a droplet in the CR mode (see figure 6.3 (f)). In particular, figure 6.3 (f) shows that for values of θ_{min} and θ_{max} in region **E** the t_{SJ} curve can be lower than *both* the t_{CR} and t_{CA} curves, *i.e.* $t_{\mathrm{SJ}} \leq \min(t_{\mathrm{CR}}, t_{\mathrm{CA}})$. For values of θ_{min} and θ_{max} on the curve **D** we have $t_{\mathrm{SJ}} = t_{\mathrm{CR}}$ for $\theta_{\mathrm{min}} \leq \theta_0 \leq \pi$ with $\theta_{0,\mathrm{max}} = \theta_{\mathrm{crit}}$ where $t_{\mathrm{SJ}} = t_{\mathrm{CR}} = t_{\mathrm{crit}}$, *i.e.* the lifetime of a droplet in the SJ mode is equal to the lifetime of a droplet in the CR mode (see 6.3 (e)) even though the evolutions of the droplets are different.

Note that the present SJ curves are qualitatively different from the curves obtained in figures 3.5, 3.6 and 4.3 in Chapters 3 and 4, respectively, and different from the curves obtained by Dietrich *et al.* [56], all of which represent special cases of the present SJ mode. Specifically, in Chapters 3 and 4 we considered the lifetimes of droplets in the SS mode, which corresponds to the special case $\theta_{\mathrm{min}} = \theta_{\mathrm{max}} = \theta^*$ (see section 5.4), and Dietrich *et al.* [56] considered the lifetimes of droplets in a SJ mode which corresponds to the special case $\theta_0 = \theta_{\mathrm{max}}$ (see section 5.5). The t_{SJ} curves obtained in figures 3.5, 3.6 and 4.3 and by Dietrich *et al.* [56] always depart from the curves representing the lifetime of droplets in the extreme modes. In particular, the t_{SJ} curves depart from the t_{CA} curve in figures 3.5, 3.6 and in the work by Dietrich *et al.* [56] and from the t_{CR} curve in figure 4.3. This behaviour is qualitatively different from the present t_{SJ} curves, which, in general, do not depart from the t_{CA} or t_{CR} curves. Note, however, that, like the present curves, the corresponding curves obtained in Chapters 3 and 4 and the corresponding curves obtained by Dietrich *et al.* [56] always lie below $t_{\mathrm{CA}}(\pi/2) = 1$, but that, unlike the present curves, which may lie below the minimum of the two extreme modes (*i.e.* $t_{\mathrm{SJ}} \leq \min(t_{\mathrm{CR}}, t_{\mathrm{CA}})$), the corresponding curves obtained in Chapters 3 and 4 and the corresponding curves obtained by Dietrich *et al.* [56] always lie on or above the minimum of the two extreme modes (*i.e.* $t_{\mathrm{SJ}} \geq \min(t_{\mathrm{CR}}, t_{\mathrm{CA}})$).

To summarise, the sketches in figure 6.3 (b)–(f) show that, depending on the values of θ_{min} and θ_{max}, the t_{SJ} curve has a global minimum either at $\theta_0 = \theta_{0,\mathrm{min}}$ or $\theta_0 = \pi$, but it always has a global maximum at $\theta_0 = \theta_{0,\mathrm{max}}$ and that t_{SJ} may be smaller than $\min(t_{\mathrm{CR}}, t_{\mathrm{CA}})$. This means that all six orderings of t_{CR}, t_{CA} and t_{SJ} can occur; this will be summarised and discussed in greater detail in the following subsection.

6.3.1 Master Diagram

As the sketches in figure 6.3 (b)–(f) show, the ordering of the lifetimes of droplets evaporating in the three modes, namely t_{SJ}, t_{CR} and t_{CA}, depends on the three parameters θ_0, θ_{min} and θ_{max}. As in Chapters 3 and 4, we summarise the orderings of the lifetimes of droplets in the different modes in a master diagram. As a three-dimensional parameter space is difficult to visualise, we shall consider two-dimensional parameter planes for different ranges/values of the third parameter. Specifically, we divide the θ_0–θ_{min} parameter plane for different ranges/values

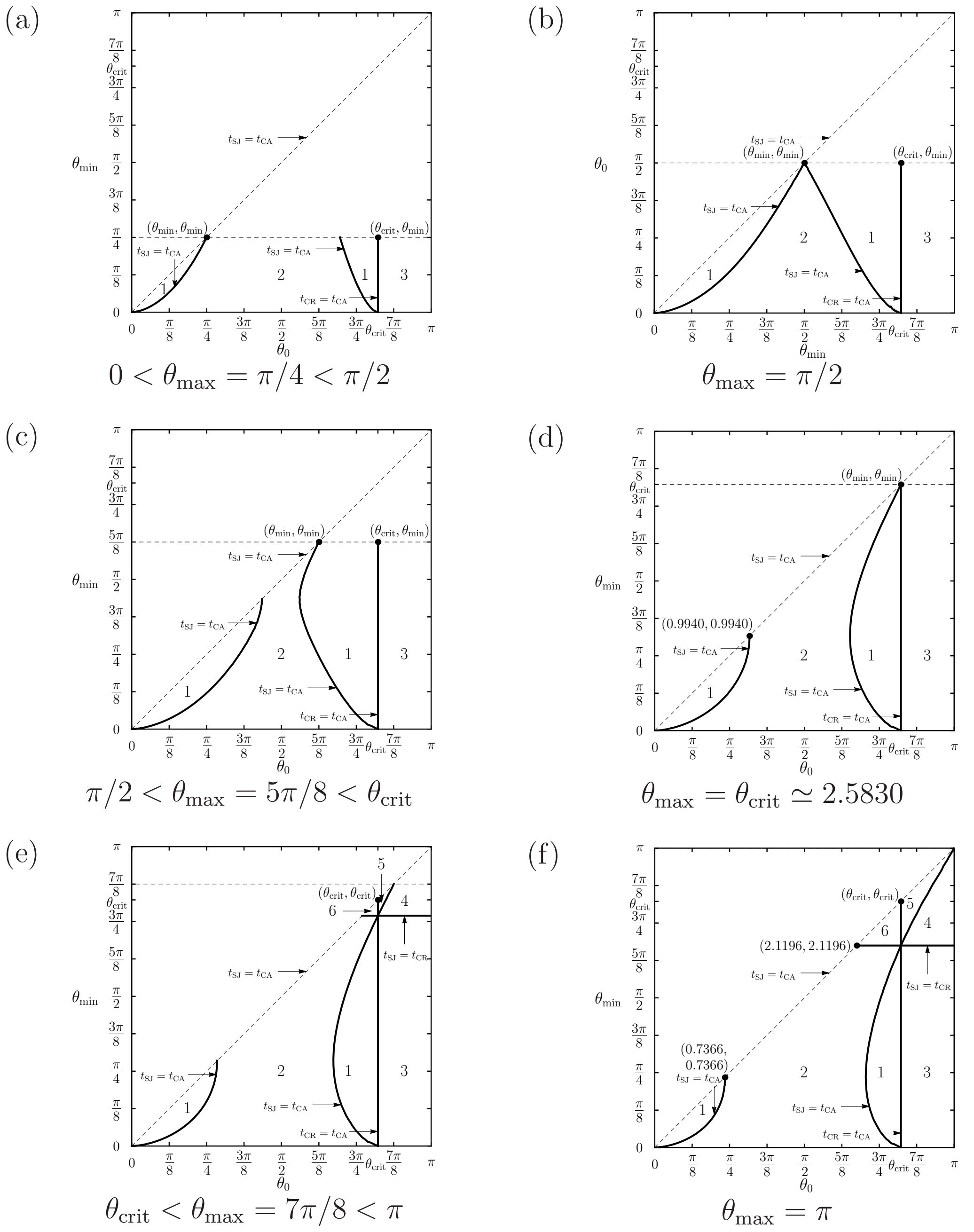

$0 < \theta_{\rm max} = \pi/4 < \pi/2$

$\theta_{\rm max} = \pi/2$

$\pi/2 < \theta_{\rm max} = 5\pi/8 < \theta_{\rm crit}$

$\theta_{\rm max} = \theta_{\rm crit} \simeq 2.5830$

$\theta_{\rm crit} < \theta_{\rm max} = 7\pi/8 < \pi$

$\theta_{\rm max} = \pi$

Figure 6.4: Parts (a)–(f) show how the θ_0–$\theta_{\rm min}$ parameter plane is divided into regions in which the six orderings of the lifetimes of initially identical droplets evaporating in the CR, CA, and SJ modes, $t_{\rm CR}$, $t_{\rm CA}$ and $t_{\rm SJ}$, occur for six different ranges/values of $\theta_{\rm max}$. Specifically, region 1 corresponds to $t_{\rm CR} < t_{\rm CA} < t_{\rm SJ}$, region 2 to $t_{\rm CR} < t_{\rm SJ} < t_{\rm CA}$, region 3 to $t_{\rm CA} < t_{\rm CR} < t_{\rm SJ}$, region 4 to $t_{\rm CA} < t_{\rm SJ} < t_{\rm CR}$, region 5 to $t_{\rm SJ} < t_{\rm CA} < t_{\rm CR}$, and region 6 to $t_{\rm SJ} < t_{\rm CR} < t_{\rm CA}$. Since $\theta_{\rm min} \le \theta_{\rm max}$ and $\theta_{\rm min} \le \theta_0$, only the trapezoidal region below $\theta_{\rm min} = \theta_{\rm max}$ and to the right of $\theta_0 = \theta_{\rm min}$ (denoted by the dashed lines) is physically realisable.

of $\theta_{\max}$ according to the orderings of the lifetimes of initially identical droplets evaporating in the CR, CA, and SJ modes, $t_{\rm CR}$, $t_{\rm CA}$ and $t_{\rm SJ}$, as shown in figure 6.4. Region 1 corresponds to $t_{\rm CR} < t_{\rm CA} < t_{\rm SJ}$, region 2 corresponds to $t_{\rm CR} < t_{\rm SJ} < t_{\rm CA}$, region 3 corresponds to $t_{\rm CA} < t_{\rm CR} < t_{\rm SJ}$, region 4 corresponds to $t_{\rm CA} < t_{\rm SJ} < t_{\rm CR}$, region 5 corresponds to $t_{\rm SJ} < t_{\rm CA} < t_{\rm CR}$, and region 6 corresponds to $t_{\rm SJ} < t_{\rm CR} < t_{\rm CA}$. Since $\theta_{\min} \le \theta_{\max}$ and $\theta_{\min} \le \theta_0$, only the trapezoidal region below $\theta_{\min} = \theta_{\max}$ and to the right of $\theta_0 = \theta_{\min}$ (denoted by the dashed lines in figure 6.4) is physically realisable. As $\theta_{\max}$ increases this physically realisable trapezoidal region $\theta_{\min} \le \theta_{\max}$ and $\theta_{\min} \le \theta_0$ increases, so that in the special case $\theta_{\max} = \pi$ the complete lower triangle of the θ_0–$\theta_{\min}$ parameter plane is physically realisable (see figure 6.4 part (f)).

Figure 6.4 (a)–(d) show that for $0 < \theta_{\max} \le \theta_{\rm crit} \simeq 2.5830$, regions 1–3 occupy substantial portions of the physically realisable region of the θ_0–$\theta_{\min}$ parameter plane. Figure 6.4 (e) and (f) show that for $\theta_{\rm crit} < \theta_{\max} \le \pi$, additional regions, namely regions 4–6, appear, which occupy increasingly larger portions of the physically realisable region of the θ_0–$\theta_{\min}$ parameter plane for increasing $\theta_{\max}$. In particular, figure 6.4 shows that *all* six orderings of $t_{\rm SJ}$, $t_{\rm CR}$ and $t_{\rm CA}$ are possible: $t_{\rm SJ}$ can be larger than both $t_{\rm CR}$ and $t_{\rm CA}$, *i.e.* $t_{\rm SJ} > \max(t_{\rm CR}, t_{\rm CA})$, as it is in regions 1 and 3, $t_{\rm SJ}$ can be smaller than both $t_{\rm CR}$ and $t_{\rm CA}$, *i.e.* $t_{\rm SJ} < \min(t_{\rm CR}, t_{\rm CA})$, as it is in regions 5 and 6, and $t_{\rm SJ}$ can be bounded by $t_{\rm CR}$ and $t_{\rm CA}$, *i.e.* $t_{\rm CR} < t_{\rm SJ} < t_{\rm CA}$ or $t_{\rm CA} < t_{\rm SJ} < t_{\rm CR}$, as it is in regions 2 and 4.

Of particular interest are regions 5 and 6, since in these two regions $t_{\rm SJ} < \min(t_{\rm CR}, t_{\rm CA})$, *i.e.* the lifetime of a droplet in the SJ mode is *shorter* than the lifetimes of initially identical droplets evaporating in the two extreme modes. This is, to the best of our knowledge, the first time that the lifetime of a droplet in a mixed mode, *i.e.* in a mode of evaporation in which the droplet evaporates with a

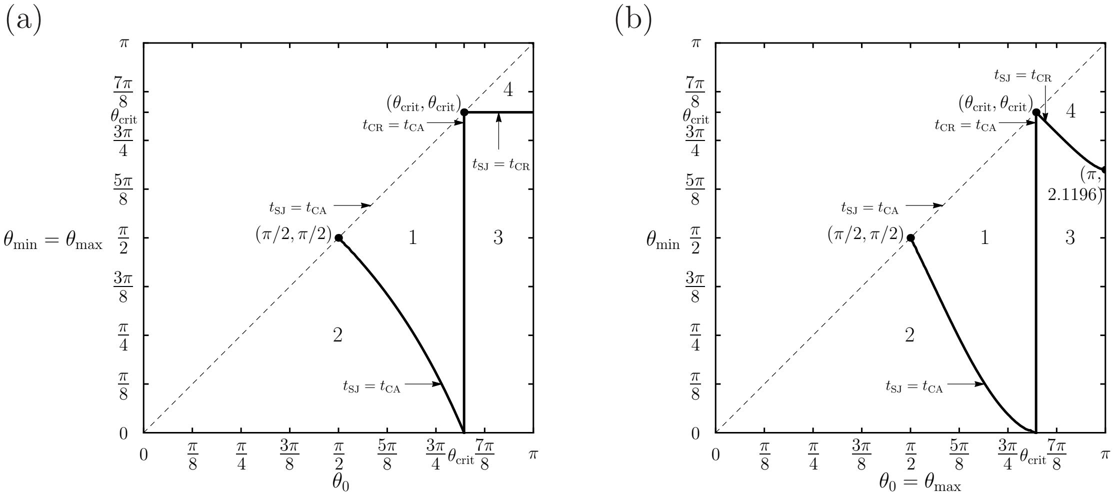

Figure 6.5: Parts (a) and (b) show how the $\theta_{\min}$–θ_0 parameter plane is divided into regions in which only four orderings of the lifetimes of initially identical droplets evaporating the CR, CA, and SJ mode, t_{CR}, t_{CA} and t_{SJ}, occur in the two special cases $\theta_{\min} = \theta_{\max} = \theta^*$ analysed in Chapter 3 and $\theta_0 = \theta_{\max}$ analysed by Dietrich *et al.* [56], respectively. Specifically, region 1 corresponds to $t_{\text{CR}} < t_{\text{CA}} < t_{\text{SJ}}$, region 2 corresponds to $t_{\text{CR}} < t_{\text{SJ}} < t_{\text{CA}}$, region 3 corresponds to $t_{\text{CA}} < t_{\text{CR}} < t_{\text{SJ}}$, and region 4 corresponds to $t_{\text{CA}} < t_{\text{SJ}} < t_{\text{CR}}$. Since $\theta_{\min} < \theta_0$ only the triangular regions below $\theta_{\min} = \theta_0$ (denoted by the dashed lines) are physically realisable.

pinned as well as with a de-pinned contact line, is reported to be shorter than the lifetimes of initially identical droplets evaporating in the two extreme modes. For comparison, figure 6.5 shows master diagrams of the orderings of the lifetimes of droplets in the SJ mode for two special cases considered previously. Specifically, figure 6.5 (a) reproduces the master diagram previously given in figure 3.7 (with the notation of this chapter), which corresponds to the special case $\theta_{\min} = \theta_{\max} = \theta^*$, in which the SJ mode is equivalent to the SS mode, and figure 6.5 (b) shows the master diagram resulting from the model of Dietrich *et al.* [56] (again, with the notation of this chapter), which corresponds to the special case $\theta_{\max} = \theta_0$; both of these are qualitatively different from those shown in figure 6.4. Furthermore, figure 6.5 shows that, unlike in the present model in which six different regions representing six different orderings occur (see figure 6.4), in both of these two special cases only four regions representing four different possible orderings occur.

Note that an alternative presentation of the master diagram to the one shown in figure 6.4 can be given, in which the θ_0–$\theta_{\max}$ parameter plane (rather than the θ_0–$\theta_{\min}$ parameter plane) is divided for different ranges/values of $\theta_{\min}$ (rather than $\theta_{\max}$) according to the orderings of the lifetimes. This alternative presentation is shown in figure 6.6, which shows again that all six orderings of t_{CR}, t_{CA} and t_{SJ} are possible and that t_{SJ} can be smaller than both t_{CR} and t_{CA}.

6.3.2 Asymptotic behaviour of t_{SJ}

We have shown in section 5.4 that the present model for the SJ mode can be considered a universal model of evaporation in the sense that in appropriate special cases it reduces to models for simpler modes of evaporation. In this subsection we shall show how in these cases the lifetimes of droplets in the SJ mode reduce to the lifetimes of droplets in these simpler modes of evaporation.

In the limit $\theta_{\min} \to 0^+$ the t_{SJ} curve approaches the t_{CR} curve from above for all values of $\theta_0 \geq \theta_{\min}$ and $\theta_{\max} \geq \theta_{\min}$ according to

$$t_{\mathrm{SJ}} = t_{\mathrm{CR}}(\theta_0) + B(\theta_0, \theta_{\max}){\theta_{\min}}^{2/3} + O(\theta_{\min}), \tag{6.3}$$

where the function $B = B(\theta_0, \theta_{\max})$ is given by

$$\begin{aligned} B(\theta_0, \theta_{\max}) = & \left(\frac{3(1+\cos\theta_0)^2}{2\sin\theta_0(\cos\theta_0+2)} \right)^{2/3} \\ & \times \frac{\sin^2\theta_{\max}}{[(\cos\theta_{\max}+2)(\cos\theta_{\max}-1)^2]^{2/3}} \int_0^{\theta_{\max}} \frac{2\,\mathrm{d}\theta}{g(\theta)}. \end{aligned} \tag{6.4}$$

In the limit $\theta_{\min} \to {\theta_{\max}}^-$, the t_{SJ} curve approaches the t_{SS} curve from below for all values of $0 \leq \theta_{\max} < \pi/2$ and from above for all values of $\pi/2 \leq \theta_{\max} < \pi$

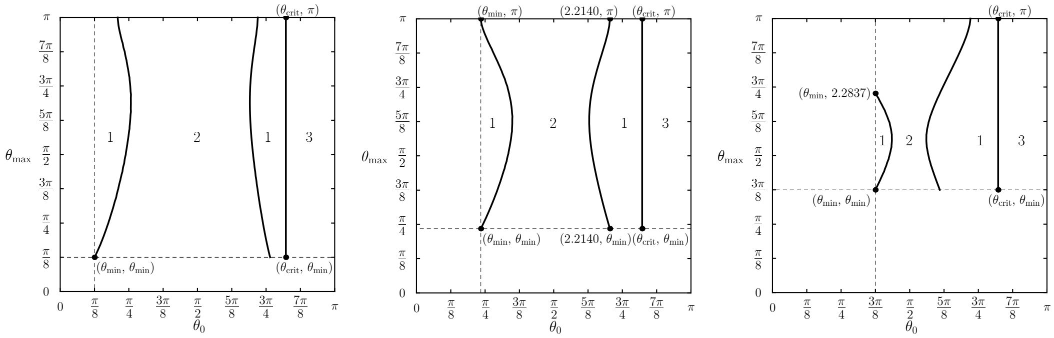

$0 < \theta_{\rm min} = \pi/8 \lesssim 0.7366$

$\theta_{\rm min} \simeq 0.7366$

$0.7366 \lesssim \theta_{\rm min} = 3\pi/8 < \pi/2$

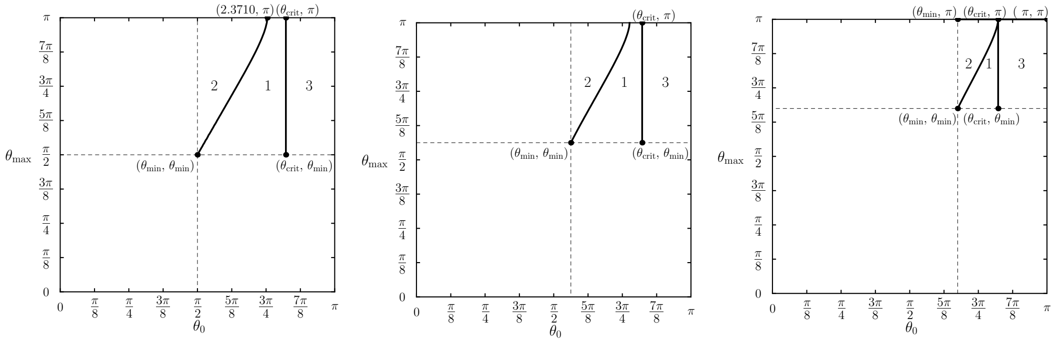

$\theta_{\rm min} = \pi/2$

$\pi/2 < \theta_{\rm min} = 9\pi/16 \lesssim 2.1196$

$\theta_{\rm min} \simeq 2.1196$

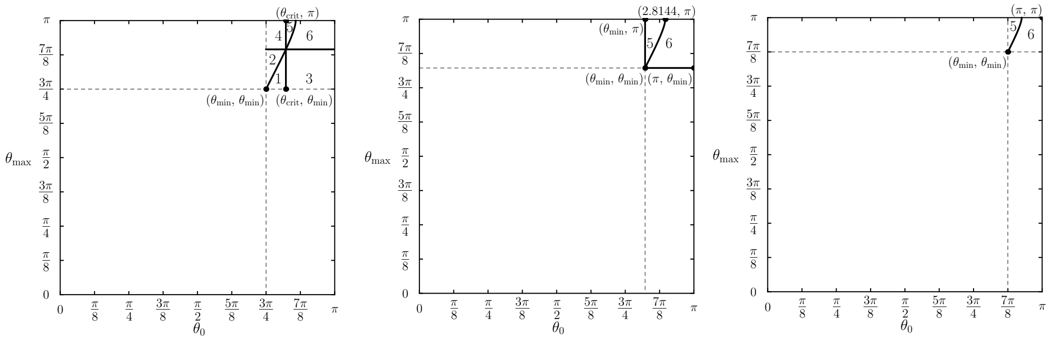

$2.1196 \lesssim \theta_{\rm min} = 3\pi/4 < \theta_{\rm crit}$

$\theta_{\rm min} = \theta_{\rm crit} \simeq 2.5830$

$\theta_{\rm crit} < \theta_{\rm min} = 7\pi/8 < \pi$

Figure 6.6: The θ_0–$\theta_{\rm max}$ parameter plane is divided into regions in which the six orderings of the lifetimes of initially identical droplets evaporating in the CR, CA, and SJ modes, $t_{\rm CR}$, $t_{\rm CA}$ and $t_{\rm SJ}$, occur for nine different ranges/values of $\theta_{\rm min}$. Specifically, region 1 corresponds to $t_{\rm CR} < t_{\rm CA} < t_{\rm SJ}$, region 2 to $t_{\rm CR} < t_{\rm SJ} < t_{\rm CA}$, region 3 to $t_{\rm CA} < t_{\rm CR} < t_{\rm SJ}$, region 4 to $t_{\rm CA} < t_{\rm SJ} < t_{\rm CR}$, region 5 to $t_{\rm SJ} < t_{\rm CA} < t_{\rm CR}$, and region 6 to $t_{\rm SJ} < t_{\rm CR} < t_{\rm CA}$. Since $\theta_{\rm min} \le \theta_{\rm max}$ and $\theta_{\rm min} \le \theta_0$, only the square region above $\theta_{\rm min} = \theta_{\rm max}$ and to the right of $\theta_0 = \theta_{\rm min}$ (denoted by the dashed lines) is physically realisable.

according to

$$t_{\mathrm{SJ}} = t_{\mathrm{SS}}(\theta_0, \theta_{\max}) + C(\theta_0, \theta_{\max})(\theta_{\max} - \theta_{\min}) + O(\theta_{\max} - \theta_{\min})^2, \tag{6.5}$$

where t_{SS} is given by equation (3.4) with $\theta_{\max} = \theta^*$ and the function $C = C(\theta_0, \theta_{\max})$ is given by

$$\begin{aligned} C(\theta_0, \theta_{\max}) &= \left(\frac{2(1+\cos\theta_0)^2}{\sin\theta_0(2+\cos\theta_0)} \right)^{2/3} \\ &\times \left[\frac{\sin\theta_{\max}(\cos\theta_{\max}+2)g'(\theta_{\max})}{2g(\theta_{\max})^2} - \frac{2\cos^2\theta_{\max} + 2\cos\theta_{\max} - 3}{2g(\theta_{\max})} \right]. \end{aligned} \tag{6.6}$$

In the limit $\theta_{\min} \to \theta_{\max}$ *and* $\theta_0 \to \theta_{\min}$ the t_{SJ} curve approaches the t_{CA} curve from below for all values of $0 \leq \theta_{\max} < \pi/2$ and from above for all values of $\pi/2 \leq \theta_{\max} < \pi$ according to

$$t_{\mathrm{SJ}} = t_{\mathrm{CA}}(\theta_{\max}) + C(\theta_{\max}, \theta_{\max})(\theta_0 - \theta_{\min}) + O(\theta_0 - \theta_{\min})^2. \tag{6.7}$$

The universality of the model for the SJ mode can also be observed in the lifetime in the small angle limit, $\theta_0 = O(\theta_{\max}) = O(\theta_{\min}) \to 0^+$, in which

$$t_{\mathrm{SJ}} = \left(\frac{1}{3}\right)^{2/3} \frac{\pi}{2} \frac{1+\lambda+\beta\lambda^2}{1+\lambda} \theta_0^{1/3} + O\left(\theta_0^{4/3}\right), \tag{6.8}$$

where $\lambda = (\theta_{\min}/\theta_{\max})^{1/3} = O(1)$ (see equation (5.18)) and $\beta = \theta_{\max}/\theta_0 = O(1)$. In the case $\theta_{\min} = 0$, $\lambda = 0$ and so t_{SJ} is identical to t_{CR} given by (2.15), and in the case $\theta_{\min} = \theta_{\max} = \theta_0$, $\lambda = \beta = 1$ and so t_{SJ} is identical to t_{CA} given by (2.16).

Reference	Substrate	Concentration	t_{SJ}	t_{CR}	t_{CA}	Error between t_{SJ} & t_{CA} (in %)
Orejon *et al.* [153]	CYTOP	0.1%	0.9983	0.8834	0.9898	0.85
Orejon *et al.* [153]	CYTOP	0.05%	0.9976	0.8900	0.9869	1.07
Orejon *et al.* [153]	CYTOP	0.025%	0.9950	0.8861	0.9887	0.63
Orejon *et al.* [153]	CYTOP	0.01%	0.9987	0.8793	0.9915	0.72
Orejon *et al.* [153]	PTFE	0.1%	0.9975	0.8861	0.9887	0.88
Orejon *et al.* [153]	PTFE	0.05%	0.9981	0.8861	0.9887	0.94
Orejon *et al.* [153]	PTFE	0.025%	0.9955	0.8834	0.9898	0.57
Orejon *et al.* [153]	PTFE	0.01%	0.9944	0.8900	0.9869	0.75
Moffat *et al.* [144]	PTFE	0.1%	0.9042	0.6590	0.9123	−0.90
Askounis *et al.* [5]	PTFE	0.1%	0.8776	0.6451	0.8990	−2.43
Askounis *et al.* [6]	Silicon	0.125%	0.7789	0.6826	0.9330	−19.78
Askounis *et al.* [7]	Silicon	0.125%	0.8250	0.6851	0.9123	−10.58

Table 6.2: The theoretically predicted lifetimes of evaporating droplets, t_{SJ}, as in table 6.1 together with theoretically predicted lifetimes of evaporating droplets in the extreme modes, t_{CR} and t_{CA}, using the experimentally determined values for θ_0, $\theta_{\min}$ and $\theta_{\max}$ given in table 5.3 and the error (in %) between t_{SJ} and t_{CA}, calculated from $(t_{\mathrm{SJ}} - t_{\mathrm{CA}}) \times 100/t_{\mathrm{SJ}}$ for the twelve data sets described in table 5.1.

6.4 Simple Approximations for t_{SJ}

As we have seen in the previous subsection, the lifetimes of droplets in the SJ mode reduce to the lifetimes of droplets in simpler modes of evaporation in appropriate special cases, and, in particular, in the limit $\theta_{\min} \to \theta_{\max}$ *and* $\theta_0 \to \theta_{\min}$ we have $t_{\mathrm{SJ}} = t_{\mathrm{CA}}$ at leading order (see equation (6.7)). In section 6.2 we pointed out that, with the exception of the two data sets by Askounis *et al.* [6, 7], the experimentally determined values of θ_0, $\theta_{\min}$ and $\theta_{\max}$ are fairly similar, so that for these data sets we expect the values for t_{SJ} to be similar to the values for t_{CA}. Table 6.2 shows the values for t_{SJ} together with the values for t_{CR} and t_{CA} using the experimentally determined values for θ_0, $\theta_{\min}$ and $\theta_{\max}$ given in table 5.3 for all twelve data sets. In particular, table 6.2 shows that the values for t_{SJ} are always larger than the values for t_{CR} for all twelve data sets considered here, and indeed that for all of the data sets with the exception of those by Askounis *et al.* [6, 7] the values for t_{SJ} are all close to the values for t_{CA} with an absolute average percentage error of 1%, so that these values for t_{SJ} can be approximated by the values for t_{CA}, *i.e.*

$$t_{\mathrm{SJ}}(\theta_0, \theta_{\mathrm{min}}, \theta_{\mathrm{max}}) \approx t_{\mathrm{CA}}(\theta_0). \tag{6.9}$$

However, for droplets in the SJ mode the contact angle θ is bounded by $\theta_{\mathrm{min}} \leq \theta \leq \theta_{\mathrm{max}}$ for most of their lifetimes. Therefore, we propose the following approximation for t_{SJ}, which we shall show is a better approximation than (6.9) for the twelve data sets considered here:

$$t_{\mathrm{SJ}}(\theta_0, \theta_{\mathrm{min}}, \theta_{\mathrm{max}}) \approx t_{\mathrm{CA}}(\theta_{\mathrm{av}}), \tag{6.10}$$

where $\theta_{\mathrm{av}} := (\theta_{\mathrm{min}} + \theta_{\mathrm{max}})/2$.

Table 6.3 gives a comparison between t_{SJ} and the approximation $t_{\mathrm{CA}}(\theta_{\mathrm{av}})$ using the experimentally determined values for θ_0, θ_{min} and θ_{max}. It also reproduces the values for the experimentally determined lifetimes, t_{exp}, given in section 6.2. Table 6.3 shows that $t_{\mathrm{CA}}(\theta_{\mathrm{av}})$ is a better approximation for t_{SJ} than $t_{\mathrm{CA}}(\theta_0)$, as the average percentage error between the values for t_{SJ} and $t_{\mathrm{CA}}(\theta_{\mathrm{av}})$ is 0.1%, whereas, it is 1% between the values for t_{SJ} and $t_{\mathrm{CA}}(\theta_0)$ for all data sets except of those of Askounis *et al.* [6, 7]. Table 6.3 also shows that for these data sets the agreement between t_{exp} and $t_{\mathrm{CA}}(\theta_{\mathrm{av}})$ is excellent as the error between these two values is smaller than 3%. However, as expected, when the values for θ_0, θ_{min} and θ_{max} are not similar, as in the cases of the two data sets of Askounis *et al.* [6, 7], the approximation (6.10) is not good for either t_{SJ} or t_{exp}, as the considerably larger errors show.

Reference	Substrate	Concentration	t_{SJ}	t_{exp}	$t_{\mathrm{CA}}(\theta_{\mathrm{av}})$	Error between t_{SJ} & t_{CA} (in %)	Error between t_{exp} & t_{CA} (in %)
Orejon *et al.* [153]	CYTOP	0.1%	0.9983	0.9878	0.9998	−0.15	−1.21
Orejon *et al.* [153]	CYTOP	0.05%	0.9976	0.9836	0.9995	−0.19	−1.61
Orejon *et al.* [153]	CYTOP	0.025%	0.9950	0.9860	0.9956	−0.06	−0.97
Orejon *et al.* [153]	CYTOP	0.01%	0.9987	0.9909	0.9996	−0.09	−0.88
Orejon *et al.* [153]	PTFE	0.1%	0.9975	0.9834	0.9989	−0.14	−1.57
Orejon *et al.* [153]	PTFE	0.05%	0.9981	0.9844	0.9995	−0.14	−1.54
Orejon *et al.* [153]	PTFE	0.025%	0.9955	0.9809	0.9946	0.09	−1.40
Orejon *et al.* [153]	PTFE	0.01%	0.9944	0.9810	0.9952	−0.08	−1.45
Moffat *et al.* [144]	PTFE	0.1%	0.9042	0.8912	0.9045	−0.03	−1.49
Askounis *et al.* [5]	PTFE	0.1%	0.8776	0.9035	0.8781	−0.06	2.18
Askounis *et al.* [6]	Silicon	0.125%	0.7789	0.9458	0.7052	9.46	25.44
Askounis *et al.* [7]	Silicon	0.125%	0.8250	0.9437	0.7911	4.10	16.17

Table 6.3: The theoretically predicted lifetimes of evaporating droplets in the SJ mode, t_{SJ}, as in table 6.1 and and the approximation given by equation 6.10, $t_{\mathrm{CA}}(\theta_{\mathrm{av}})$, together with the experimentally determined droplet lifetimes, t_{exp}, as in table 6.1 and the error (in %) between the approximation and t_{SJ} and t_{exp}, calculated from $(t_{\mathrm{SJ}} - t_{\mathrm{CA}}) \times 100/t_{\mathrm{SJ}}$ and $(t_{\mathrm{exp}} - t_{\mathrm{CA}}) \times 100/t_{\mathrm{exp}}$ for the twelve data sets described in table 5.1.

6.5 Summary

In this chapter we gave a complete description of the lifetime of a droplet in the SJ mode and compared it with the lifetimes of droplets determined from twelve data sets in the literature. Furthermore, we showed that the lifetime of a droplet in the SJ mode may be shorter than the lifetimes of droplets in both extreme modes of evaporation, and that the present t_{SJ} curves are qualitatively different from those obtained in Chapters 3 and 4 and by Dietrich *et al.* [56], which are special cases of the present model. Finally, we gave simple approximations for t_{SJ} given by equations (6.9) and (6.10), which are appropriate in situations in which the values of θ_0, θ_{min} and θ_{max} are fairly similar.

Chapter 7

Conclusions

7.1 Summary

This thesis considered the evolution of sessile droplets in different modes of evaporation and, in particular, the lifetimes of such droplets.

In Chapter 2 we considered droplets evaporating in the two extreme modes of evaporation, namely the CR and CA modes. In particular, we described the manner in which the extreme modes of evaporation become indistinguishable on strongly hydrophobic substrates. Furthermore, we obtained simple asymptotic expressions that provide good approximations to the evolutions of R, θ, and V for a wide range of hydrophobic substrates. As a consequence we showed that it is appropriate to extrapolate the scaled volume $(V/V_0)^{2/3}$ linearly with time t to determine the lifetimes of droplets evaporating in the CR mode as well as in the CA mode on superhydrophobic substrates.

Chapters 3 and 4 concerned the lifetimes of droplets in the SS mode. Chapter 3 gave a complete description of the unexpectedly subtle relationship between the lifetime of a droplet evaporating in a SS mode and those of initially identical droplets evaporating in the extreme modes. It particular, we showed that for initial contact angles in the range $0 \leq \theta_0 < \pi/2$ the lifetime of a droplet in the SS mode is constrained by those of initially identical droplets evaporating in the extreme modes, but that for initial contact angles in the range $\pi/2 \leq \theta_0 < \pi$ the lifetime of a droplet in the SS mode is not, in general, constrained by those of initially identical droplets evaporating in the extreme modes. We also showed that there is good agreement between experimentally determined lifetimes from appropriate data sets in the literature and predicted lifetimes of droplets in the SS mode.

Whereas in Chapter 3 the initial contact angle, θ_0, and the receding contact angle, θ^*, were considered to be independent of each other, in Chapter 4 we proposed a simple relationship between θ_0 and θ^* based on the assumption of a constant maximum pinning force f_{p}. We used this relationship to give a complete description of how the lifetime of a droplet in the SS mode depends on θ_0 and f_{p}. In particular, we showed that the dependence of t_{SS} on θ_0 is qualitatively different from that described in Chapter 3 and that it is qualitatively much more similar to (but still not identical to) that tentatively suggested by Shanahan *et al.* [204]. Furthermore, both the proposed relationship as well as the predicted lifetimes using it were found to agree surprisingly well with experimental results obtained from the literature.

Chapters 5 and 6 concerned droplets evaporating in the SJ mode. In Chapter 5 we developed a simple model for the SJ mode that does not resolve the details of the local behaviour near the contact line but instead captures the global behaviour of the droplet. This model was based on the assumptions that during a stick phase the contact radius R is constant, that a jump phase is instantaneous, and that the contact angle at which the contact line de-pins, θ_{min}, and the contact angle at which the contact line re-pins, θ_{max}, remain constant throughout the entire evaporation process. Furthermore, we showed that for experimental data sets in the literature that satisfy these assumptions there is excellent agreement between both the theoretically predicted duration of the stick phase and the change of R during a jump phase and the experimentally determined values. It was also shown that in appropriate special cases the SJ mode reduces to the CR, CA or SS mode.

Whereas Chapter 5 concerned the evolution of a droplet in the SJ mode, Chapter 6 focused on the lifetime of a droplet in this mode. In particular, it was shown that, despite the model predicting an infinite number of stick and jump phases, there was good agreement between the experimentally determined lifetime of droplets in the literature and the (finite) theoretically predicted lifetimes. Furthermore, a complete description of the rather complicated relationship between the lifetime of a droplet in the SJ mode and those of initially identical droplets in the extreme modes was given. In particular, we showed that the lifetime of a droplet in the SJ mode may be shorter than the lifetime of initially identical droplets in the extreme modes. Finally, approximations to the lifetime of a droplet in the SJ mode were proposed and were found to be good approximations to the experimentally determined lifetimes in situations in which the values of θ_0, θ_{min} and θ_{max} are fairly similar.

7.2 Future Work

The results described in the present thesis suggest many possible directions for future research.

In section 1.5.2 we described different investigations of the evaporation of droplets of water on different superhydrophobic substrates that reached different conclusions about the significance of evaporative cooling, and hence different conclusions about the applicability of the simplest version of the diffusion-limited model. Further theoretical and experimental investigations could focus on determining precisely which factors lead to a significant effect of evaporative cooling on droplets on superhydrophobic substrates observed by Dash and Garimella [49, 50], but not by Gelderblom *et al.* [78] and Talbot *et al.* [228].

In Chapter 2 we described the manner in which the extreme modes of evaporation become indistinguishable on strongly hydrophobic substrates in the simplest version of the diffusion-limited model. Since the instantaneous evaporative cooling depends only on the instantaneous geometry of the droplet, and hence its instantaneous effect will be the same on both extreme modes, we hypothesised that even in situations such as those studied by Dash and Garimella [49, 50] in which evaporative cooling is significant, the extreme modes will still become indistinguishable on strongly hydrophobic substrates. However, further theoretical investigations are needed to confirm or disprove this hypothesis.

All of the experimental data sets considered in Chapters 3–6 have initial contact angles in the range $0.61 \simeq 35^\circ \lesssim \theta_0 \lesssim 2.14 \simeq 123^\circ$ (see tables 4.1 and 5.1). Thus testing the present models for droplets on superhydrophobic substrates remains an open challenge.

As pointed out in Chapter 4, the value of the maximum pinning force f_p will depend on the nature of the substrate (such as its surface roughness and chemical heterogeneity), as well as on the fluid and the atmosphere, and so will, in general, be different for different experiments. However, the unexpected insensitivity of the lifetimes to the value of f_p revealed in Chapter 4 reinforces the need for further theoretical and experimental work on the nature of contact line pinning and depinning on non-ideal substrates.

The model for the SJ mode described in Chapter 5 assumes that during a stick phase the contact radius R is constant, that a jump phase is instantaneous, and that the contact angle at which the contact line de-pins, θ_{min}, and the contact angle at which the contact line re-pins, θ_{max}, remain constant throughout the entire evaporation process. Future work could focus on relaxing some or all of these assumptions. For example, for an evaporating droplet containing suspended nanoparticles, variation in R during the stick phase and in θ_{min} and θ_{max} throughout the entire evaporation process could be included in the model, by, for example, making R, θ_{min} and θ_{max} functions of the concentration of nanoparticles in such a way that for high concentrations there is little variation in R, θ_{min} and θ_{max}, but for low concentrations there is significant variation in them. This extended model could also be used to describe how the SJ mode reduces to the CR or CA mode in appropriate special limits. In particular, for very high concentrations the contact line is pinned for most of its lifetime and the droplet evaporates in the CR mode, for very low concentrations the contact line is de-pinned and the droplet evaporates in the CA mode, and for intermediate concentrations of nanoparticles the contact line is pinned, de-pins and re-pins multiple times and the droplet evaporates in the SJ mode.

Orejon *et al.* [153] showed that for droplets with a 0.1% concentration of nanoparticles evaporating on a CYTOP or PTFE substrate the contact line eventually ceases de-pinning, so that thereafter it evaporates in a stick phase for the remainder of its lifetime (see figures 1.9 and 5.1). The model described in Chapter 5 could be extended to capture this effect by replacing the infinite stick and jump phases with a final stick phase. This could be done by considering a maximum pinning force like that in Chapter 4, as well as a minimum pinning force. Once the pinning force remains below its maximum value, the contact line no longer de-pins and thereafter the droplet evaporates in a stick phase for the remainder of its lifetime.

The present model assumes the jump phases are instantaneous; another possible extension could include a more detailed modelling of the rapid variation in the droplet profile during the jump phases.

Models for other SJ modes could be developed in the future. For example, in the model described in Chapter 5 it is assumed that θ_{min} and θ_{max}, and therefore $\delta\theta := \theta_{\text{max}} - \theta_{\text{min}}$, are constant throughout the entire evaporation process. Replacing these assumptions with the assumption that the change in R during each jump phase is constant, *i.e.* $\delta R := R_{n+1} - R_n$ is a constant, describes a different SJ mode, which has been observed by, for example, McHale *et al.* [142] and Xu *et al.* [245] for droplets evaporating on pillared substrates, in which case δR represents, for example, the width of a pillar plus the gap between two adjacent pillars.

Alternatively, the models for the SS and the SJ mode, described in Chapter 3 and Chapter 5, respectively, could be combined to describe a stick-jump-slide (SJS) mode, as investigated by, for example, Kusumaatmaja and Yeomans [117].

We believe that the results described in the present thesis make a significant contribution to the study of evaporating sessile droplets; nonetheless the previously mentioned open challenges and possible extensions show that much research still remains to be done before we can completely understand this fascinating and important problem.

Bibliography

[1] E Adachi, A S Dimitrov, K Nagayama, Stripe patterns formed on a glass surface during droplet evaporation, *Langmuir* **11** 1057–1060 (1995)

[2] N K Adam, G Jessop, Angles of contact and polarity of solid surfaces, *J. Chem. Soc.* **127** 1863–1868 (1925)

[3] N Anantharaju, M Panchagnula, S Neti, Evaporating drops on patterned surfaces: transition from pinned to moving triple line, *J. Coll. Int. Sci.* **337** 176–182 (2009)

[4] S R Annapragada, S Dash, S V Garimella, J Y Murthy, Dynamics of droplet motion under electrowetting actuation, *Langmuir* **27** 8198–8204 (2011)

[5] A Askounis, D Orejon, V Koutsos, K Sefiane, M E R Shanahan, Nanoparticle deposits near the contact line of pinned volatile droplets: size and shape revealed by atomic force microscopy, *Soft Matter* **7** 4152–4155 (2011)

[6] A Askounis, K Sefiane, V Koutsos, M E R Shanahan, Structural transitions in a ring stain created at the contact line of evaporating nanosuspension sessile drops, *Phys. Rev. E* **87** 012301 (2013)

[7] A Askounis, K Sefiane, V Koutsos, M E R Shanahan, The effect of evaporation kinetics on nanoparticle structuring within contact line deposits of volatile drops, *Colloids and Surfaces A: Physicochemical and Engineering Aspects* **441** 855–866 (2014)

[8] A Askounis, Surface nano-patterning using the coffee-stain effect, *Ph.D. Thesis*, University of Edinburgh, UK, (2014)

[9] D Attinger, C Moore, A Donaldson, A Jafari, H A Stone, Fluid dynamics topics in bloodstain pattern analysis: comparative review and research opportunities, *Forensic Science International* **231** 375–396 (2013)

[10] K A Baldwin, M Granjard, D Willmer, K Sefiane, D J Fairhurst, Drying and deposition of poly(ethylene oxide) droplets determined by Péclet number, *Soft Matter* **7** 7819–7826 (2011)

[11] K A Baldwin, S Roest, D J Fairhurst, K Sefiane, M E R Shanahan, Monolith formation and ring-stain suppression in low-pressure evaporation of poly(ethylene oxide) droplets, *J. Fluid Mech.* **695** 321–329 (2012)

[12] K A Baldwin, D J Fairhurst, The effects of molecular weight, evaporation rate and polymer concentration on pillar formation in drying poly(ethylene) oxide droplets, *Colloids and Surfaces A: Physicochemical and Engineering Aspects* **441** 867–871 (2014)

[13] L Y Barash, Dependence of fluid flows in an evaporating sessile droplet on the characteristics of the substrate *Int. J. Heat Mass Tran.* **84** 419–426 (2015).

[14] S Bauer, Two Fuji apples, `http://commons.wikimedia.org/wiki/File:Fuji_apple.jpg?uselang=en-gb`, accessed on 11th March 2015

[15] A M Benselama, S Harmand, K Sefiane, A perturbation method for solving the micro-region heat transfer problem, *Phys. Fluids* **23** 102103 (2011)

[16] A M Benselama, S Harmand, K Sefiane, Thermocapillary effects on steadily evaporating contact line: a perturbative local analysis, *Phys. Fluids* **24** 072105 (2012)

[17] G Berteloot, C-T Pham, A Daerr, F Lequeux, L Limat, Evaporation-induced flow near a contact line: consequences on coating and contact angle, *Euro. Phys. Lett.* **83** 14003 (2008)

[18] G Berteloot, A Hoang, A Daerr, P Kavehpour, F Lequeux, L Limat, Evaporation of a sessile droplet: inside the coffee stain, *J. Coll. Int. Sci.* **370** 155–161 (2012)

[19] R Bhardwaj, X Fang, D Attinger, Pattern formation during the evaporation of a colloidal nanoliter drop: a numerical and experimental study, *New Journal of Physics* **11** 075020 (2009)

[20] K S Birdi, D T Vu, A Winter, A study of the evaporation rates of small water drops placed on a solid surface, *J. Phys. Chem.* **93** 3702–3703 (1989)

[21] K S Birdi, D T Vu, Wettability and the evaporation rates of fluids from solid surfaces, *J. Adhesion Sci. Technol.* **7** 485–493 (1993)

[22] E Bormashenko, A Musin, M Zinigrad, Evaporation of droplets on strongly and weakly pinning surfaces and dynamics of the triple line, *Colloids and Surfaces A: Physicochemical and Engineering Aspects* **385** 235–240 (2011)

[23] E Bormashenko, Wetting of Real Surfaces, *De Gruyter* (2013)

[24] W Bou Zeid, D Brutin, Influence of relative humidity on spreading, pattern formation and adhesion of a drying drop of whole blood, *Colloids and Surfaces A: Physicochemical and Engineering Aspects* **430** 1–7 (2013)

[25] W B[ou] Zeid, J Vicente, D Brutin, Influence of evaporation rate on cracks formation of a drying drop of whole blood, *Colloids and Surfaces A: Physicochemical and Engineering Aspects* **432** 139–146 (2013)

[26] C Bourgès-Monnier, M E R Shanahan, Influence of evaporation on contact angle, *Langmuir* **11** 2820–2829 (1995)

[27] D Brutin, B Sobac, F Rigollet, C Le Niliot, Infrared visualization of thermal motion inside a sessile drop deposited onto a heated surface, *Experimental Thermal and Fluid Science* **35** 521–530 (2011)

[28] D Brutin, Influence of relative humidity and nano-particle concentration on pattern formation and evaporation rate of pinned drying drops of nanofluids, *Colloids and Surfaces A: Physicochemical and Engineering Aspects* **429** 112–120 (2013)

[29] J Buongiorno, Convective transport in nanofluids, *J. Heat Transf.* **128** 240–250 (2006)

[30] J P Burelbach, S G Bankoff, S H Davis, Nonlinear stability of evaporating/condensing liquid films *J. Fluid Mech.* **195** 463–494 (1988)

[31] M Cachile, O Bénichou, A-M Cazabat, Evaporating droplets of completely wetting fluids, *Langmuir* **18** 7985–7990 (2002)

[32] M Cachile, O Bénichou, C Poulard, A-M Cazabat, Evaporating droplets, *Langmuir* **18** 8070–8078 (2002)

[33] F Carle, B Sobac, D Brutin, Experimental evidence of the atmospheric convective transport contribution to sessile droplet evaporation, *Appl. Phys. Lett.* **102** 061603 (2013)

[34] F Carle, D Brutin, How surface functional groups influence fracturation in nanofluid droplet dry-out, *Langmuir* **29** 9962–9966 (2013)

[35] J Cavan, Watercolor Stain 1, URL: `https://www.flickr.com/photos/mj12982/3953116352/in/set-72157622451494860`, accessed on 11th March 2015

[36] A-M Cazabat, M A Cohen Stuart, Dynamics of wetting: effects of surface roughness, *J. Phys. Chem.* **90** 5845–5849 (1986)

[37] A-M Cazabat, G Guéna, Evaporation of macroscopic sessile droplets, *Soft Matter* **6** 2591–2612 (2010)

[38] M Cezza, Study of the feasibility of controlling the length scale of the phase separation of organic molecular mixtures on Si(111) substrates, *Ph.D. Thesis*, University of Maryland, USA, (2014)

[39] C H Chon, S Paik, J B Tipton, K D Kihm, Effect of nanoparticle sizes and number densities on the evaporation and dryout characteristics for strongly pinned nanofluid droplet, *Langmuir* **23** 2953–2960 (2007)

[40] M D Choudhury, T Dutta, S Tarafdar, Pattern formation in droplets of starch gels containing NaCl dried on different surfaces, *Colloids and Surfaces A: Physicochemical and Engineering Aspects* **432** 110–118 (2013)

[41] J R E Christy, Y Hamamoto, K Sefiane, Flow transition within an evaporating binary mixture sessile drop, *Phys. Rev. Lett.* **106** 205701 (2011)

[42] R W Coutant, E C Penski, Experimental evaluation of mass transfer from sessile drops, *Ind. Eng. Chem. Fund.* **21** 250–254 (1982)

[43] R V Craster, O K Matar, K Sefiane, Pinning, retraction, and terracing of evaporating droplets containing nanoparticles, *Langmuir* **25** 3601–3609 (2009)

[44] A Crivoi, F Duan, Evaporation-induced branched structures from sessile nanofluid droplets, *J. Phys. Chem. B* **117** 7835–7843 (2013)

[45] A Crivoi, F Duan, Amplifying and attenuating the coffee-ring effect in drying sessile nanofluid droplets, *Phys. Rev. E* **87** 042303 (2013)

[46] A Crivoi, F Duan, Fingering structures inside the coffee-ring pattern, *Colloids and Surfaces A: Physicochemical and Engineering Aspects* **432** 119–126 (2013)

[47] A Crivoi, F Duan, Three-dimensional Monte Carlo model of the coffee-ring effect in evaporating colloidal droplets, *Sci. Rep.* **4** 4310 (2014)

[48] S Dash, N Kumari, S V Garimella, Characterization of ultrahydrophobic hierarchical surfaces fabricated using a single-step fabrication methodology, *J. Micromech. Microeng.* **21** 105012 (2011)

[49] S Dash, S V Garimella, Droplet evaporation dynamics on a superhydrophobic surface with negligible hysteresis, *Langmuir* **29** 10785–10795 (2013)

[50] S Dash, S V Garimella, Droplet evaporation on heated hydrophobic and superhydrophobic surfaces, *Phys. Rev. E* **89** 042402 (2014)

[51] R D Deegan, O Bakajin, T F Dupont, G Huber, S R Nagel, T A Witten, Capillary flow as the cause of ring stains from dried liquid drops, *Nature* **389** 827–829 (1997)

[52] R D Deegan, Pattern formation in drying drops, *Phys. Rev. E* **61** 475–785 (2000)

[53] R D Deegan, O Bakajin, T F Dupont, G Huber, S R Nagel, T A Witten, Contact line deposits in an evaporating drop, *Phys. Rev. E* **62** 756–765 (2000)

[54] H K Dhavaleswarapu, C P Migliaccio, S V Garimella, J Y Murthy, Experimental investigation of evaporation from low-contact-angle sessile droplets, *Langmuir* **26** 880–888 (2010)

[55] D Diehl, Soil water repellency: dynamics of heterogeneous surfaces, *Colloids and Surfaces A: Physicochemical and Engineering Aspects* **432** 8–18 (2013)

[56] E Dietrich, E S Kooij, X Zhang, H J W Zandvliet, D Lohse, Stick-jump mode in surface droplet dissolution, *Langmuir* **31** 4696–4703 (2015)

[57] M D Doganci, B U Sesli, H Y Erbil, Diffusion-controlled evaporation of sodium dodecyl sulfate solution drops placed on a hydrophobic substrate, *J. Coll. Int. Sci.* **362** 524–531 (2011)

[58] M D Doganci, H Y Erbil, Shape and diameter control of C60 fullerene microstains by evaporation of aqueous SDS–fullerene dispersion drops, *Colloids and Surfaces A: Physicochemical and Engineering Aspects* **432** 104–109 (2013)

[59] G J Dunn, S K Wilson, B R Duffy, S David, K Sefiane, A mathematical model of the evaporation of a thin sessile liquid droplet: comparison between experiment and theory, *Colloids and Surfaces A: Physicochemical and Engineering Aspects* **323** 50–55 (2008)

[60] G J Dunn, S K Wilson, B R Duffy, S David, K Sefiane, The strong influence of substrate conductivity on droplet evaporation, *J. Fluid Mech.* **623** 329–351 (2009)

[61] G J Dunn, S K Wilson, B R Duffy, K Sefiane, Evaporation of a thin droplet on a thin substrate with a high thermal resistance, *Phys. Fluids* **21** 052101 (2009)

[62] G J Dunn, B R Duffy, S K Wilson, D Holland, Quasi-steady spreading of a thin ridge of fluid with temperature-dependent surface tension on a heated or cooled substrate, *Q. J. Mech. Appl. Math.* **62** 365–402 (2009)

[63] J Dupas, E Verneuil, L Talini, F Lequeux, M Ramaioli, L Forny, Diffusion and evaporation control the spreading of volatile droplets onto soluble films, *Interfacial Phenomena and Heat Transfer* **1** 231–243 (2013)

[64] T Dutta, A Giri, M D Choudhury, S Tarafdar, Experiment and simulation of multifractal growth of crystalline NaCl aggregates in aqueous gelatin medium, *Colloids and Surfaces A: Physicochemical and Engineering Aspects* **432** 127–131 (2013)

[65] J Eggers, L M Pismen, Nonlocal description of evaporating drops, *Phys. Fluids* **22** 112101 (2010)

[66] H B Eral, D Mampallil Augustine, M H G Duits, F Mugele, Suppressing the coffee stain effect: how to control colloidal self-assembly in evaporating drops using electrowetting, *Soft Matter* **7** 4954–4958 (2011)

[67] H B Eral, D van den Ende, F Mugele, Say goodbye to coffee stains, *Physics World* **April 2012** 33–37 (2012)

[68] H B Eral, D J C M ’t Mannetje, J M Oh, Contact angle hysteresis: a review of fundamentals and applications, *Coll. Polym. Sci.* **291** 247–260 (2013)

[69] H Y Erbil, G McHale, S M Rowan, M I Newton, Determination of the receding contact angle of sessile drops on polymer surfaces by evaporation, *Langmuir* **15** 7378–7385 (1999)

[70] H Y Erbil, G McHale, M I Newton, Drop evaporation on solid surfaces: constant contact angle mode, *Langmuir* **18** 2636–2641 (2002)

[71] H Y Erbil, Evaporation of pure liquid sessile and spherical suspended drops: a review, *Adv. Colloid Interface Sci.* **170** 67–86 (2012)

[72] L Espín, S Kumar, Sagging of evaporating droplets of colloidal suspensions on inclined substrates, *Langmuir* **30** 11966–11974 (2014)

[73] X Fang, B Li, E Petersen, Y Ji, J C Sokolov, M H Rafailovich, Factors controlling the drop evaporation constant, *J. Phys. Chem. B* **109** 20554–20557 (2005)

[74] B J Fischer, Particle convection in an evaporating colloidal droplet, *Langmuir* **18** 60–67 (2002)

[75] L Frastia, A J Archer, U Thiele, Dynamical model for the formation of patterned deposits at receding contact lines, *Phys. Rev. Lett.* **106** 077801 (2011)

[76] J Fukai, H Ishizuka, Y Sakai, M Kaneda, M Morita, A Takahara, Effects of droplet size and solute concentration on drying process of polymer solution droplets deposited on homogeneous surfaces, *Int. J. Heat Mass Tran.* **49** 3561–3567 (2006)

[77] E Y Gatapova, A A Semenov, D V Zaitsev, O A Kabov, Evaporation of a sessile water drop on a heated surface with controlled wettability, *Colloids and Surfaces A: Physicochemical and Engineering Aspects* **441** 776–785 (2014)

[78] H Gelderblom, Á G Marín, H Nair, A van Houselt, L Lefferts, J H Snoeijer, D Lohse, How water droplets evaporate on a superhydrophobic substrate, *Phys. Rev. E* **83** 026306 (2011)

[79] H Gelderblom, O Bloemen, J H Snoeijer, Stokes flow near the contact line of an evaporating drop, *J. Fluid Mech.* **709** 69–84 (2012)

[80] H Gelderblom, H A Stone, J H Snoeijer, Stokes flow in a drop evaporating from a liquid subphase, *Phys. Fluids* **25** 102102 (2013)

[81] P-G de Gennes, F Brochard-Wyart, D Quéré, Capillarity and wetting phenomena: drops, bubbles, pearls, waves, *Springer* (2004)

[82] F Girard, M Antoni, S Faure, A Steinchen, Evaporation and Marangoni driven convection in small heated water droplets, *Langmuir* **22** 11085–11091 (2006)

[83] F Girard, M Antoni, K Sefiane, On the effect of Marangoni flow on evaporation rates of heated water drops, *Langmuir* **24** 9207–9210 (2008)

[84] K Gleason, S A Putnam, Microdroplet evaporation with a forced pinned contact line, *Langmuir* **30** 10548–10555 (2014)

[85] R J Good, A thermodynamic derivation of Wenzel's modification of Young's equation for contact angles; together with a theory of hysteresis, *J. Am. Chem. Soc.* **74** 5041–5042 (1952)

[86] L Grandas, C Reynard, R Santini, L Tadrist, Experimental study of the evaporation of a sessile drop on a heat[ed] wall. Wetting influence, *Int. J. Thermal Sci.* **44** 137–146 (2005)

[87] G Guéna, C Poulard, M Voue, J De Coninck, A-M Cazabat, Evaporation of sessile liquid droplets, *Colloids and Surfaces A: Physicochemical and Engineering Aspects* **291** 191–196 (2006)

[88] G Guéna, P Allancon, A-M Cazabat, Receding contact angle in the situation of complete wetting: experimental check of a model used for evaporating droplets, *Colloids and Surfaces A: Physicochemical and Engineering Aspects* **300** 307–314 (2007)

[89] G Guéna, C Poulard, A-M Cazabat, The leading edge of evaporating droplets, *J. Coll. Int. Sci.* **312** 164–171 (2007)

[90] M Hadj-Achour, D Brutin, Fractal pattern formation in nanosuspension sessile droplets via evaporation-spreading on a glass substrate, *Colloids and Interface Science Communications* **1** 43–46 (2014)

[91] Y Hamamoto, J R E Christy, K Sefiane, Order-of-magnitude increase in flow velocity driven by mass conservation during the evaporation of sessile drops, *Phys. Rev. E* **83** 051602 (2011)

[92] M A Hampton, T A H Nguyen, A V Nguyen, Z P Xu, L Huang, V Rudolph, Influence of surface orientation on the organization of nanoparticles in drying nanofluid droplets, *J. Coll. Int. Sci.* **377** 456–462 (2012)

[93] W Han, Z Lin, Learning from "coffee rings": ordered structures enabled by controlled evaporative self-assembly, *Angew. Chem. Int. Ed.* **51** 1534–1546 (2012)

[94] B He, F Duan, Full-field convection flow visulization in pendant droplets by tilt-angle imaging, *Appl. Phys. Lett.* **103** 053508 (2013)

[95] S Herbert, T Gambaryan-Roisman, P Stephan, Influence of the governing dimensionless parameters on heat transfer during single drop impingement onto a hot wall, *Colloids and Surfaces A: Physicochemical and Engineering Aspects* **432** 57–63 (2013)

[96] H Hu, R G Larson, Evaporation of a sessile droplet on a substrate, *J. Phys. Chem. B* **106** 1334–1344 (2002)

[97] H Hu, R G Larson, Analysis of the microfluid flow in an evaporating sessile droplet, *Langmuir* **21** 3963–3971 (2005)

[98] H Hu, R G Larson, Analysis of the effects of Marangoni stresses on the microflow in an evaporating sessile droplet, *Langmuir* **21** 3972–3980 (2005)

[99] H Hu, R G Larson, Marangoni effect reverses coffee-ring depositions, *J. Phys. Chem. B* **110** 7090–7094 (2006)

[100] D Huang, L Ma, X Xu, The capillary outward flow inside pinned drying droplets, *Int. J. Heat Mass Tran.* **83** 307–310 (2015)

[101] H P Jansen, H J W Zandvliet, E S Kooij, Evaporation of elongated droplets on chemically stripe-patterned surfaces, *Int. J. Heat Mass Tran.* **82** 537–544 (2015)

[102] J F Joanny, P G de Gennes, A model for contact angle hysteresis, *J. Chem. Phys.* **81** 552–562 (1984)

[103] R E Johnson, R H Dettre, Contact angle hysteresis. I. Study of an idealized rough surface, *Advances in Chemistry* **43** 112–135 (1964)

[104] R E Johnson, R H Dettre, Contact angle hysteresis. III. Study of an idealized heterogeneous surface, *J. Phys. Chem.* **68** 1744–1750 (1964)

[105] N Jung, C S Yoo, P H Leo, Instability deposit patterns in an evaporating droplet, *J. Phys. Chem. B* **118** 2535–2543 (2014)

[106] T Kajiya, C Monteux, T Narita, F Lequeux, M Doi, Contact-line recession leaving a macroscopic polymer film in the drying droplets of water-poly(N,N-dimethylacrylamide) (PDMA) solution, *Langmuir* **25** 6934–6939 (2009)

[107] T Kajiya, A Daerr, T Narita, L Royon, F Lequeux, L Limat, Dynamics of the contact line in wetting and diffusing processes of water droplets on hydrogel (PAMPS-PAAM) substrates, *Soft Matter* **7** 11425–11432 (2011)

[108] T Kajiya, A Daerr, T Narita, L Royon, F Lequeux, L Limat, Advancing liquid contact line on visco-elastic gel substrates: stick-slip vs. continuous motions, *Soft Matter* **9** 454–461 (2013)

[109] G Karapetsas, O K Matar, P Valluri, K Sefiane, Convective rolls and hydrothermal waves in evaporating sessile drops, *Langmuir* **28** 11433–11439 (2012)

[110] R Karlsson, Coffee stain on an white paper, `www.free-photo-gallery.org/photos/coffee-stain/`, accessed on 11th March 2015

[111] P L Kelly-Zion, C J Pursell, S Vaidya, J Batra, Evaporation of sessile drops under combined diffusion and natural convection, *Colloids and Surfaces A: Physicochemical and Engineering Aspects* **381** 31–36 (2011)

[112] P L Kelly-Zion, J Batra, C J Pursell, Correlation for the convective and diffusive evaporation of a sessile drop, *Int. J. Heat Mass Tran.* **64** 278–285 (2013)

[113] P L Kelly-Zion, C J Pursell, N Hasbamrer, B Cardozo, K Gaughan, K Nickels, Vapor distribution above an evaporating sessile drop, *Int. J. Heat Mass Tran.* **65** 165–172 (2013)

[114] A E Korenchenko, V P Beskachko, Oscillations of a sessile droplet in open air, *Phys. Fluids* **25** 112106 (2013)

[115] N M Kovalchuck, A Trybala, V M Starov, Evaporation of sessile droplets, *Curr. Opin. Colloid Interface Sci.* **19** 336–342 (2014)

[116] S A Kulinich, M Farzaneh, Effect of contact angle hysteresis on water droplet evaporation from super-hydrophobic surfaces, *Appl. Surf. Sci.* **255** 4056–4060 (2009)

[117] H Kusumaatmaja, J M Yeomans, Modeling contact angle hysteresis on chemically patterned and superhydrophobic surfaces, *Langmuir* **23** 6019–6032 (2007)

[118] R G Larson, Transport and deposition patterns in drying sessile droplets, *AIChE J* **60** 1538–1571 (2014)

[119] N N Lebedev, Special Functions and their Applications, *Prentice Hall Inc.* (1965)

[120] P Lebedev-Stepanov, K Vlasov, Simulation of self-assembly in an evaporating droplet of colloidal solution by dissipative particle dynamics, *Colloids and Surfaces A: Physicochemical and Engineering Aspects* **432** 132–138 (2013)

[121] R Ledesma-Aguilar, D Vella, J M Yeomans, Lattice-Boltzmann simulations of droplet evaporation, *Soft Matter* **10** 8267–8275 (2014)

[122] C Y Lee, B J Zhang, J Park, K J Kim, Water droplet evaporation on Cu-based hydrophobic surfaces with nano- and micro-structures, *Int. J. Heat Mass Tran.* **55** 2151–2159 (2012)

[123] F-I Li, S M Thaler, P H Leo, J A Barnard, Dendrimer pattern formation in evaporating drops, *J. Phys. Chem. B* **110** 25838–25843 (2006)

[124] F-I Li, P H Leo, J A Barnard, Dendrimer pattern formation in evaporating drops: solvent, size, and concentration effects, *J. Phys. Chem. B* **112** 14266–14273 (2008)

[125] F-I Li, P H Leo, J A Barnard, Temperature-dependent formation of dendrimer islands from ring structures, *J. Phys. Chem. B* **112** 16497–16504 (2008)

[126] G Li, S M Flores, C Vavilala, M Schmittel, K Graf, Evaporation dynamics of microdroplets on self-assembled monolayers and dialkyl disulfides, *Langmuir* **25** 13438–13447 (2009)

[127] H Li, N Fowler, S Struck, S Sivasankar, Flow triggered by instabilities at the contact line of a drop containing nanoparticles, *Soft Matter* **7** 5116–5119 (2011)

[128] T Lim, J Yang, S Lee, J Chung, D Hong, Deposit pattern of inkjet printed pico-liter droplet, *International Journal of Precision Engineering and Manufacturing* **13** 827–833 (2012)

[129] L Limat, Straight contact lines on a soft, incompressible solid, *Eur. Phys. J. E* **35** 134 (2012)

[130] D Lohse, X Zhang, Pinning and gas oversaturation imply stable single surface nanobubbles, *Phys. Ref. E* **91** 031003(R) (2015)

[131] M C Lopes, E Bonaccurso, T Gambaryan-Roisman, P Stephan, Influence of the substrate thermal properties on sessile droplet evaporation: effect of transient heat transport, *Colloids and Surfaces A: Physicochemical and Engineering Aspects* **432** 64–70 (2013)

[132] S Maheshwari, L Zhang, Y Zhu, H-C Chang, Coupling between precipitation and contact-line dynamics: multiring stains and stick-slip motion, *Phys. Rev. Lett.* **100** 044503 (2008)

[133] K L Maki, S Kumar, Fast evaporation of spreading droplets of colloidal suspensions, *Langmuir* **27** 11347–11363 (2011)

[134] S Manukyan, H M Sauer, I V Roisman, K A Baldwin, D J Fairhurst, H Liang, J Venzmer, C Tropea, Imaging internal flows in a drying sessile polymer dispersion drop using Spectral Radar Optical Coherence Tomography (SR-OCT), *J. Coll. Int. Sci.* **395** 287–293 (2013)

[135] A G Marín, H Gelderblom, D Lohse, J H Snoeijer, Order-to-disorder transition in ring-shaped colloidal stains, *Phys. Rev. Lett.* **107** 085502 (2011)

[136] A G Marín, H Gelderblom, A Susarrey-Arce, A van Houselt, L Lefferts, J G E Gardeniers, D Lohse, J H Snoeijer, Building microscopic soccer balls with evaporating colloidal fakir drops, *Proceedings of the National Academy of Sciences (PNAS)* **109** 16455–16458 (2012)

[137] H Masoud, J D Felske, Analytical solution for inviscid flow inside an evaporating sessile drop, *Phys. Rev. E* **79** 016301 (2009)

[138] H Masoud, J D Felske, Analytical solution for Stokes ow inside an evaporating sessile drop: spherical and cylindrical cap shapes, *Phys. Fluids* **21** 042102 (2009)

[139] O K Matar, R V Craster, K Sefiane, Dynamic spreading of droplets containing nanoparticles, *Phys. Rev. E* **76** 056315 (2007)

[140] G McHale, S M Rowan, M I Newton, M K Banerjee, Evaporation and the wetting of a low-energy solid surface, *J. Phys. Chem. B* **102** 1964–1967 (1998)

[141] G McHale, N J Shirtcliffe, M I Newton, Contact-angle hysteresis on superhydrophobic surfaces, *Langmuir* **20** 10146–10149 (2004)

[142] G McHale, S Aqil, N J Shirtcliffe, M I Newton, H Y Erbil, Analysis of droplet evaporation on a superhydrophobic surface, *Langmuir* **21** 11053–11060 (2005)

[143] S Y Misyura, High temperature nonisothermal desorption in a water-salt droplet, *Int. J. Therm. Sci.* **92** 34–43 (2015)

[144] J R Moffat, K Sefiane, M E R Shanahan, Effect of TiO_2 nanoparticles on contact line stick-slip behavior of volatile drops, *J. Phys. Chem. B* **113** 8860–8866 (2009)

[145] R Mollaret, K Sefiane, J R E Christy, D Veyret, Experimental and numerical investigation of the evaporation into air of a drop on a heated surface, *Chem. Eng. Res. Design* **82** 471–480 (2004)

[146] Y Msambwa, D J Fairhurst, F Ouali, How robust is the ring stain for evaporating suspension droplets?, *Interfacial Phenomena and Heat Transfer* **1** 207–214 (2013)

[147] T A H Nguyen, A V Nguyen, M A Hampton, Z P Xu, L Huang, V Rudolph, Theoretical and experimental analysis of droplet evaporation on solid surfaces, *Chemical Engineering Science* **69** 522–529 (2012)

[148] T A H Nguyen, A V Nguyen, On the lifetime of evaporating sessile droplets, *Langmuir* **28** 1924–1930 (2012)

[149] T A H Nguyen, A V Nguyen, Increased evaporation kinetics of sessile droplets by using nanoparticles, *Langmuir* **28** 16725–16728 (2012)

[150] T A H Nguyen, A V Nguyen, Reply to Comment on "Increased evaporation kinetics of sessile droplets by using nanoparticles" *Langmuir* **29** (39) 12330 (2013)

[151] T A H Nguyen, M A Hampton, A V Nguyen, Evaporation of nanoparticle droplets on smooth hydrophobic surfaces: the inner coffee ring deposits, *J. Phys. Chem. C* **117** 4707–4716 (2013)

[152] T A H Nguyen, A V Nguyen, Transient volume of evaporating sessile droplets: 2/3, 1/1, or another power law? *Langmuir* **30** 6544–6547 (2014)

[153] D Orejon, K Sefiane, M E R Shanahan, Stick-slip of evaporating droplets: substrate hydrophobicity and nanoparticle concentration, *Langmuir* **27** 12834–12843 (2011)

[154] D Orejon, K Sefiane, M E R Shanahan, Young-Lippmann equation revisited for nano-suspensions, *Appl. Phys. Lett.* **102** 201601 (2013)

[155] Z Pan, S Dash, J A Weibel, S V Garimella, Assessment of water droplet evaporation mechanisms on hydrophobic and superhydrophobic substrates, *Langmuir* **29** 15831–15841 (2013)

[156] Z Pan, J A Weibel, S V Garimella, Influence of surface wettability on transport mechanisms governing water droplet evaporation, *Langmuir* **30** 9726–9730 (2014)

[157] F Parisse, C Allain, Drying of colloidal suspension droplets: experimental study and profile renormalization, *Langmuir* **13** 3598–3602 (1997)

[158] M Parsa, S Harmand, K Sefiane, M Bigerelle, R Deltombe, Effect of substrate temperature on pattern formation of nanoparticles from volatile drops, *Langmuir* **31** 3354–3367 (2015)

[159] A J Petsi, V N Burganos, Stokes ow inside an evaporating liquid line for any contact angle, *Phys. Rev. E* **78** 036324 (2008)

[160] R G Picknett, R Bexon, The evaporation of sessile or pendant drops in still air, *J. Coll. Int. Sci.* **61** 336–350 (1977)

[161] P G Pittoni, C-C Yu, T-S Chang, S-Y Lin, Evaporation of water drops on polymer surfaces: pinning, depinning and dynamics of the triple line, *Colloids and Surfaces A: Physicochemical and Engineering Aspects* **432** 89–98 (2013)

[162] P G Pittoni, C-H Lin, T-S Yu, S-Y Lin, On the uniqueness of the receding contact angle: effects of substrate roughness and humidity on evaporation of water drops, *Langmuir* **30** 9346–9354 (2014)

[163] B E Poling, G H Thomson, D G Friend, R L Rowley, W V Wilding, Physical and chemical data In Perry's chemical engineers' handbook, Editors: R H Perry, D W Green, *McGraw-Hill Publishing* 8th edition [online] (2008)

[164] Y O Popov, T A Witten, Characteristic angles in the wetting of an angular region: surface shape, *Euro. Phys. J. E* **6** 211–220 (2001)

[165] Y O Popov, T A Witten, Characteristic angles in the wetting of an angular region: deposit growth, *Phys. Rev. E* **68** 036306 (2003)

[166] Y O Popov, Evaporative deposition patterns: spatial dimensions of the deposit, *Phys. Rev. E* **71** 036313 (2005)

[167] C Poulard, O Bénichou, A-M Cazabat, Freely receding evaporating droplets, *Langmuir* **19** 8828–8834 (2003)

[168] C Poulard, G Guéna, A-M Cazabat, Diffusion-driven evaporation of sessile drops, *J. Phys.: Condens. Matter* **17** S4213–S4227 (2005)

[169] C Poulard, A-M Cazabat, Spontaneous spreading of nematic liquid crystals, *Langmuir* **21** 6270–6276 (2005)

[170] S A Putnam, A M Briones, L W Byrd, J S Ervin, M S Hanchak, A White, J G Jones, Microdroplet evaporation on superheated surfaces, *Int. J. Heat Mass Tran.* **55** 5793–5807 (2012)

[171] M Ramiasa, J Ralston, R Fetzer, R Sedev, The influence of topography on dynamic wetting, *Adv. Colloid Interface Sci.* **206** 275–293 (2014).

[172] S Ramos, A Tanguy, Pinning-de-pinning of the contact line on nanorough surfaces, *Eur. Phys. J. E* **19** 433–440 (2006)

[173] R C Reid, J M Prausnitz, B E Poling, The properties of gases and liquids, *McGraw-Hill* 4th edition (1987)

[174] E Rio, A Daerr, F Lequeux, L Limat, Moving contact lines of a colloidal suspension in the presence of drying, *Langmuir* **22** 3186–3191 (2006)

[175] W D Ristenpart, P G Kim, C Domingues, J Wan, H A Stone, Influence of substrate conductivity on circulation reversal in evaporating drops, *Phys. Rev. Lett.* **99** 234502 (2007)

[176] O E Ruiz, W Z Black, Evaporation of water droplets placed on a heated horizontal surface, *J. Heat Transfer* **124** 854–863 (2002)

[177] M A Saada, S Chikh, L Tadrist, Numerical investigation of heat and mass transfer of an evaporating sessile drop on a horizontal surface, *Phys. Fluids* **22** 112115 (2010)

[178] M A Saada, S Chikh, L Tadrist, Evaporation of a sessile drop with pinned or receding contact line on a substrate with different thermophysical properties, *Int. J. Heat Mass Tran.* **58** 197–208 (2013)

[179] F Schoenfeld, K-H Graf, S Hardt, H-J Butt, Evaporation dynamics of sessile liquid drops in still air with constant contact radius, *Int. J. Heat Mass Tran.* **51** 3696–3699 (2008)

[180] K Sefiane, L Tadrist, M Douglas, Experimental study of evaporating water-ethanol mixture sessile drop: influence of concentration, *Int. J. Heat Mass Tran.* **46** 4527–4534 (2003)

[181] K Sefiane, Effect of nonionic surfactant on wetting behavior of an evaporating drop under a reduced pressure environment, *J. Coll. Int. Science* **272** 411–419 (2004)

[182] K Sefiane, On the dynamic capillary effects in the wetting and evaporation process of binary droplets, *Fluid Dynamics and Materials Processing* **1** 267–276 (2005)

[183] K Sefiane, L Tadrist, Experimental investigation of the de-pinning phenomenon on rough surfaces of volatile drops, *Int. Comm. Heat Mass Transfer* **33** 482–490 (2006)

[184] K Sefiane, On the role of structural disjoining pressure and contact line pinning in critical heat flux enhancement during boiling of nanofluids, *Appl. Phys. Lett.* **89** 044106 (2006)

[185] K Sefiane, J Cameron, Modelling of heat and fluid flow during the evaporation of volatile drops on hot surfaces, *Prog. Comp. Fluid Dynam.* **6** 363– 370 (2006)

[186] K Sefiane, R Bennacer, Nanofluids droplets evaporation kinetics and wetting dynamics on rough heated substrates, *Adv. Coll. Int. Sci.* **147–148** 263–271 (2009)

[187] K Sefiane, S K Wilson, S David, G J Dunn, B R Duffy, On the effect of the atmosphere on the evaporation of sessile droplets of water, *Phys. Fluids* **21** 062101 (2009)

[188] K Sefiane, On the formation of regular patterns from drying droplets and their potential use for bio-medical applications, *J. Bionic Eng.* **7** S82–S93 (2010)

[189] K Sefiane, R Bennacer, An expression for droplet evaporation incorporating thermal effects, *J. Fluid Mech.* **667** 260–271 (2011)

[190] S Semenov, V M Starov, R G Rubio, M G Velarde, Instantaneous distribution of fluxes in the course of evaporation of sessile liquid droplets: computer simulations, *Colloids and Surfaces A: Physicochemical and Engineering Aspects* **372** 127–134 (2010)

[191] S Semenov, V M Starov, R G Rubio, H Agogo, M G Velarde, Evaporation of sessile water droplets: universal behaviour in presence of contact angle hysteresis, *Colloids and Surfaces A: Physicochemical and Engineering Aspects* **391** 135–144 (2011)

[192] S Semenov, V M Starov, M G Velarde, R G Rubio, Droplets evaporation: problems and solutions, *Eur. Phys. J. Special Topics* **197** 265–278 (2011)

[193] S Semenov, V M Starov, R G Rubio, H Agogo, M G Velarde, Evaporation of sessile water droplets in presence of contact angle hysteresis, *Math. Model Nat. Phenom.* **7** 82–98 (2012)

[194] S Semenov, A Trybala, H Agogo, N Kovalchuk, F Ortega, R G Rubio, V M Starov, M G Velarde, Evaporation of droplets of surfactant solutions, *Langmuir* **29** 10028–10036 (2013)

[195] S Semenov, A Trybala, R G Rubio, N Kovalchuk, V [M] Starov, M G Velarde, Simultaneous spreading and evaporation: recent developments, *Adv. Coll. Int. Sci.* **206** 382–398 (2014)

[196] W Sempels, R De Dier, H Mizuno, J Hofkens, J Vermant, Auto-production of biosurfactants reverses the coffee ring effect in a bacterial system, *Nature Communications* **4** 1757 (2013)

[197] N Shahidzadeh-Bonn, S Rafaï, A Azouni, D Bonn, Evaporating droplets, *J. Fluid Mech.* **549** 307–313 (2006)

[198] M E R Shanahan, Meniscus shape and contact angle of a slightly deformed axisymmetric drop, *J. Phys. D: Appl. Phys.* **22** 1128–1135 (1989)

[199] M E R Shanahan, Capillary movement of nearly axisymmetric sessile drops, *J. Phys. D: Appl. Phys.* **23** 321–327 (1990)

[200] M E R Shanahan, A simple analysis of local wetting hysteresis on a Wilhelmy plate, *Surface and Interface Analysis* **17** 489–495 (1991)

[201] M E R Shanahan, Simple theory of "stick-slip" wetting hysteresis, *Langmuir* **11** 1041–1043 (1995)

[202] M E R Shanahan, Is a sessile drop in an atmosphere saturated with its vapour really in equilibrium?, *Langmuir* **18** 7763–7765 (2002)

[203] M E R Shanahan, K Sefiane, Kinetics of triple line motion during evaporation In Contact Angle, Wettability and Adhesion, Editor: K L Mittal, *Koninklijke Brill N V* 19–31 (2009)

[204] M E R Shanahan, K Sefiane, J R Moffat, Dependence of volatile droplet lifetime on the hydrophobicity of the substrate, *Langmuir* **27** 4572–4577 (2011)

[205] D H Shin, S H Lee, J-Y Jung, J Y Yoo, Evaporating characteristics of sessile droplet on hydrophobic and hydrophilic surfaces, *Microelectronic Engineering* **86** 1350–1353 (2009)

[206] D H Shin, S H Lee, C K Choi, S Retterer, The evaporation and wetting dynamics of sessile water droplets on submicron-scale patterned silicon hydrophobic surfaces, *J. Micromech. Microeng.* **20** 055021 (2010)

[207] D H Shin, C K Choi, Y T Kang, S H Lee, Local aggregation characteristics of nanofluid droplet evaporation during evaporation, *Int. J. Heat Mass Tran.* **72** 336–344 (2014)

[208] D H Shin, J S Allen, C K Choi, S H Lee, Visualization of an evaporating thin layer during the evaporation of a nanofluid droplet, *Langmuir* **31** 12371241 (2015)

[209] N J Shirtcliffe, G McHale, M I Newton, Learning from superhydrophobic plants: the use of hydrophilic areas on superhydrophobic surfaces for droplet control, *Langmuir* **25** 14121–14122 (2009)

[210] L Shmuylovich, A Q Shen, H A Stone, Surface morphology of drying latex films: multiple ring formation, *Langmuir* **18** 3441–3445 (2002)

[211] S K Singh, S Khandekar, D Pratap, S A Ramakrishna, Wetting dynamics and evaporation of sessile droplets on nano-porous alumina surfaces, *Colloids and Surfaces A: Physicochemical and Engineering Aspects* **432** 71–81 (2013)

[212] G S Smith, R Barakat, Electrostatics of two conducting spheres in contact, *Appl. Sci. Res.* **30** 418–432 (1975)

[213] C Snow, Potential problems and capacitance for a conductor bounded by 2 intersecting spheres, *J. Res. Nat. Bur. Stand.* **43** 377–407 (1949)

[214] B Sobac, D Brutin, Triple-line behavior and wettability controlled by nanocoated substrates: influence on sessile drop evaporation, *Langmuir* **27** 14999–15007 (2011)

[215] B Sobac, D Brutin, Thermocapillary instabilities in an evaporating drop deposited onto a heated substrate, *Phys. Fluids* **24** 032103 (2012)

[216] B Sobac, D Brutin, Thermal effects of the substrate on water droplet evaporation, *Phys. Rev. E* **86** 021602 (2012)

[217] B Sobac, D Brutin, Desiccation of a sessile drop of blood: cracks, folds formation and delamination, *Colloids and Surfaces A: Physicochemical and Engineering Aspects* **448** 34–44 (2014)

[218] H Song, Y Lee, S Jin, H-Y Kim, J Y Yoo, Prediction of sessile drop evaporation considering surface wettability, *Microelectronic Engineering* **88** 3249–3255 (2011)

[219] D M Soolaman, H-Z Yu, Water microdroplets on molecularly tailored surfaces: correlation between wetting hysteresis and evaporation mode switching, *J. Phys. Chem. B* **109** 17967–17973 (2005)

[220] J M Stauber, S K Wilson, B R Duffy, K Sefiane, Comment on “Increased evaporation kinetics of sessile droplets by using nanoparticles”, *Langmuir* **29** 12328–12329 (2013)

[221] J M Stauber, S K Wilson, B R Duffy, K Sefiane, On the lifetime of a fluid droplet on a solid substrate in a mixed mode of evaporation”, published electronically in the Proceedings of the 13th UK National Heat Transfer Conference, 2nd–3rd September 2013, London

[222] J M Stauber, S K Wilson, B R Duffy, K Sefiane, On the lifetime of evaporating droplets, extended abstract in the Proceedings of the European Coating Symposium (ECS 13), 11th–13th September 2013, (ed. J. De Coninck), Mons, Belgium, pp. 118–120. ISBN 978-2-87325-077-5.

[223] J M Stauber, S K Wilson, B R Duffy, K Sefiane, On the lifetimes of evaporating droplets, *J. Fluid Mech.* **744** R2 (2014)

[224] J M Stauber, S K Wilson, B R Duffy, K Sefiane, On the evaporation of droplets on strongly hydrophobic substrates, *Langmuir* **31** 3653–3660 (2015)

[225] J M Stauber, S K Wilson, B R Duffy, K Sefiane, On the lifetimes of evaporating droplets with related initial and receding contact angles, submitted to *Phys. Fluids* (2015)

[226] W Sun, F Yang, Dynamics of the evaporative dewetting of a volatile liquid film confined within a circular ring, *Langmuir* **31** 4024–4031 (2015)

[227] R Tadmor, Line energy and the relation between advancing, receding and Young contact angles, *Langmuir* **20** 7659–7664 (2004)

[228] E L Talbot, A Berson, P S Brown, C D Bain, Evaporation of picoliter droplets on surfaces with a range of wettabilities and thermal conductivities, *Phys. Rev. E* **85** 061604 (2012)

[229] E L Talbot, L Yang, A Berson, C D Bain, Control of the particle distribution in inkjet printing through an evaporation-driven solgel transition, *ACS Appl. Mater. Interfaces* **6** 9572–583 (2014)

[230] Y Y Tarasevich, Simple analytical model of capillary flow in an evaporating sessile drop, *Phys. Rev. E* **71** 027301 (2005)

[231] Y Y Tarasevich, I V Vodolazskaya, O P Bondarenko, Modeling of spatial-temporal distribution of the components in the drying of sessile droplet of biological fluid, *Colloids and Surfaces A: Physicochemical and Engineering Aspects* **432** 99–103 (2013)

[232] A K Thokchom, R Swaminathan, A Singh, Fluid flow and particle dynamics inside an evaporating droplet containing live bacteria displaying chemotaxis, *Langmuir* **30** 12144–12153 (2014)

[233] A Trybala, A Okoye, S Semenov, H Agogo, R G Rubio, F Ortega, V M Starov, Evaporation kinetics of sessile droplets of aqueous suspensions of inorganic nanoparticles, *J. Coll. Int. Sci.* **403** 49–57 (2013)

[234] Y Tsoumpas, S Dehaeck, M Galvagno, A Rednikov, H Ottevaere, U Thiele, P Colinet, Nonequilibrium Gibbs' criterion for completely wetting volatile liquids, *Langmuir* **30** 11847–11852 (2014)

[235] K Uno, K Hayashi, T Hayashi, K Ito, H Kitano, Particle adsorption in evaporating droplets of polymer latex dispersions on hydrophilic and hydrophobic surfaces, *Colloid Polym. Sci.* **276** 810–815 (1998)

[236] B Valentine, How to photograph refracting dew droplets, URL: `http://www.wonderfulphotos.com/articles/macro/dewdrops/`, accessed on 11th March 2015

[237] V Vancauwenberghe, P D Marco, D Brutin, Wetting and evaporation of a sessile drop under an external electrical field: a review, *Colloids and Surfaces A: Physicochemical and Engineering Aspects* **432** 50–56 (2013)

[238] F Vincentz, Raindrops on a window, URL: `http://commons.wikimedia.org/wiki/File:Rain_drops_on_window_01_ies.jpg`, accessed on 11th March 2015

[239] W A Wakeham, M J Assael, A Marmur, J De Coninck, T D Blake, S A Theron, E Zussman, Material properties: measurement and data In Springer handbook of experimental fluid mechanics, Editors: C Tropea, A L Yarin, J F Foss, *Springer* 106–119 (2007)

[240] J Wang, J R G Evans, Drying behaviour of droplets of mixed powder suspensions, *J. Euro. Ceram. Soc.* **26** 3123–3131 (2006)

[241] J Wang, J R G Evans, Segregation in multicomponent ceramic colloids during drying of droplets, *Phys. Rev. E* **73** 021501 (2006)

[242] B M Weon, J H Je, C Poulard, Convection-enhanced water evaporation, *AIP Advances* **1** 012102 (2011)

[243] D Willmer, K A Baldwin, C Kwartnik, D J Fairhurst, Growth of solid conical structures during multistage drying of sessile poly(ethylene oxide) droplets, *Phys. Chem. Chem. Phys.* **12** 3998–4004 (2010)

[244] A W Wray, D T Papageorgiou, R V Craster, K Sefiane, O K Matar, Electrostatic suppression of the "coffee stain effect", *Langmuir* **30** 5849–5858 (2014)

[245] L Xu, Z Li, S Yao, Directional motion of evaporating droplets on gradient surfaces, *Appl. Phys. Lett.* **101** 064101 (2012)

[246] X Xu, L Ma, Analysis of the effects of evaporative cooling on the evaporation of liquid droplets using a combined field approach, *Sci. Rep.* **5** 8614 (2015)

[247] H Yoo, C Kim, Experimental studies on formation, spreading, drying of inkjet drop of colloidal suspensions, *Colloids and Surfaces A: Physicochemical and Engineering Aspects* **468** 234-245 (2015)

[248] T Young, An essay of the cohesion of fluids, *Philos. Trans. R. Soc. Lond.* **95** 65–87 (1805)

[249] Y-S Yu, Z[-Q] Wang, Y-P Zhao, Experimental and theoretical investigations of evaporation of sessile water droplet[s] on hydrophobic surfaces, *J. Coll. Int. Sci.* **365** 254–259 (2012)

[250] Y-S Yu, Z-Q Wang, Y-P Zhao, Experimental stufy of evaporation of sessile water droplet[s] on PDMS surfaces, *Acta. Mech. Sinica* **29** 799–805 (2013)

[251] P J Yunker, D J Durian, A G Yodh, Coffee rings and coffee disks: physics of the edge, *Physics Today* **August 2013** 60–61 (2013)

[252] Y Zhang, L Chen, S Yang, J R G Evans, Control of particle segregation during drying of ceramic suspension droplets, *J. Euro. Ceram. Soc.* **27** 2229–2235 (2007)

[253] Y Zhang, S Yang, L Chen, J R G Evans, Shape changes during the drying of droplets of suspensions, *Langmuir* **24** 3752–3758 (2008)

[254] Y Zhang, J R G Evans, Morphologies developed by the drying of droplets containing dispersed and aggregated layered double hydroxide platelets, *J. Coll. Int. Sci.* **395** 11–17 (2013)

[255] K Zhang, L Ma, X Xu, J Luo, D Guo, Temperature distribution along the surface of evaporating droplets, *Phys. Rev. E* **89** 032404 (2014)

[256] X Zhang, J Wang, L Bao, E Dietrich, R C A van der Veen, S Peng, J Friend, H J W Zandvliet, L Yeo, D Lohse, Mixed mode of dissolving immersed nanodroplets at a solid-water interface, *Soft Matter* **11** 1889–1900 (2015)